CO_2 Laser Annealing for Metal Halide Perovskite Solar Cells

THE UNIVERSITY OF SYDNEY

Jianpeng Yi

Supervisor: Anita Ho-Baillie

Associate supervisor: David McKenzie

Associate supervisor: Md Arafat Mahmud

School of Physics

Faculty of Science

The University of Sydney

A thesis submitted to fulfil requirements for the degree of Doctor of Philosophy

December 2025

Declaration

I certify that the intellectual content of this thesis is the product of my own work and that all the assistance received in preparing this thesis and sources have been acknowledged.

Signature and date

7 Dec. 2025

Statement of Contributions by Student

I wrote the entire thesis and revised it according to input from my supervisors and contributors to the experimental work of this thesis.

Chapter 2 contains materials from the following publication:

Jianpeng Yi, Tik-Lun Leung, Justin Digweed, Jueming Bing, Christopher Bailey, Chwenhaw Liao, Runmin Tao, Guoliang Wang, Zhuofeng Li, Hieu T. Nguyen, Dane R. McCamey, Jianghui Zheng, Md Arafat Mahmud, Anita W. Y. Ho-Baillie. "CO_2 Laser Crystallization in Ambient for Highly Efficient $FAPbI_3$ Perovskite Solar Cells". Small, 2024, 20, 2402215.

Regarding contributions, Ho-Baillie and I conceived the main idea and designed the experiments. Digweed and Leung facilitated access to the CO_2 laser system. I conducted the literature review, fabricated the devices, and performed various measurements, including *J-V* testing, external quantum efficiency (EQE) testing, light-dependent V_{OC} analysis, and device stability assessments. Additionally, I carried out optical absorption measurements, photoluminescence (PL) analysis, atomic force microscopy (AFM), and sheet resistance evaluations. Bing assisted in collecting x-ray diffraction (XRD) data, while Wang conducted scanning electron microscopy (SEM) measurements. Bailey and McCamey contributed to temperature-dependent V_{OC} measurements and data processing. Li and Nguyen performed transient photoluminescence (TrPL) measurements. X-ray photoelectron spectroscopy (XPS) data were collected by Liao and Tao. I drafted and revised the manuscript, created the figures and tables. Mahmud, Zheng, and Anita -Baillie provided critical reviews and revisions.

Chapters 3-4 contain materials from the following publication:

Jianpeng Yi, Christopher Bailey, Tik-Lun Leung, Runmin Tao, Guoliang Wang, Jueming Bing, Md Arafat Mahmud, David R. Mckenzie, Anita W. Y. Ho-Baillie, "Efficient Ambient-All-Laser-Annealed Wide Bandgap Perovskite Solar Cells", Adv. Funct. Mater., 2025, 2503971.

Regarding contributions,

Ho-Baillie, Muhmud, Mckenzie and I conceived the main ideas and designed the experiments. I conducted literature review, fabricated and optimized devices, carried out *J-V*, EQE, light-dependent V_{OC}, PL, TrPL, XRD measurements. I measured device temperatures before, during and after laser annealing. Wang assisted with SEM measurements for data processing and

visualizations by me. Tao contributed to XPS measurements, data processing and analysis. Bailey and I worked on the COMSOL simulation: construction and optimization. Bing provided laboratory supports. I drafted and revised the manuscript which was also revised by Leung, Mahmud and Anita Ho-Baillie.

Jianpeng Yi, Jueming Bing, Cheng-Yu Yeh, Christopher Bailey, Guoliang Wang, Runmin Tao, Tik-Lun Leung, Li Liu, Yu Wang, Priyank Vijaya Kumar, Kourosh Kalantar-Zadeh, Rajendra Kumar Gunasekaran, Dane R. McCamey, David R. Mckenzie, Chu-Chen Chueh, Md Arafat Mahmud, Anita W. Y. Ho-Baillie, "Efficient All Ambient-Laser-Annealed Perovskite-Organic-Photovoltaic Tandem Solar Cells", Adv. Funct. Mater., 2025, Accepted.

Regarding contributions, Ho-Baillie, Muhmud, Mckenzie and I conceived the main ideas and designed the experiments. I conducted literature review, fabricated and optimized devices, carried out *J*-*V*, EQE, light-dependent V_{OC}, PL, TrPL, XRD measurements. Chang and Chueh contributed to the OPV device research. Wang assisted with SEM measurements for data processing and visualizations by me. Bailey and I worked on the COMSOL simulation: construction and optimization. Bailey and McCamey contributed to temperature-dependent V_{OC} measurements. Liu, Wang, Kumar, and Kalantar-Zadeh contributed to GIXRD measurements. Bing, Gunasekaran and Tao provided laboratory and experimental supports. Ho-Baillie and I drafted and revised the manuscript which was also revised by Leung, Bing, Mahmud, and Ho-Baillie.

Permissions to include the published material has been granted by the corresponding author.

Signature and date

7 Dec 2025

As the supervisor for the candidature upon which this thesis is based, I can confirm that the authorship attribution statements above are correct.

Signature and date

7 Dec 2025

Acknowledgement

I would like to express my genuine gratitude to everyone who has guided and supported me throughout my PhD journey. First and foremost, I am deeply thankful to my supervisor, Professor Anita Ho-Baillie, for giving me the incredible opportunity to work on laser-perovskite solar cell research. I am also profoundly grateful to my associate supervisors, Professor David McKenzie and Dr. Md Arafat Muhmud, for their kind guidance, invaluable academic support, and continuous encouragement, all of which have been instrumental in making this research possible.

Secondly, I would like to extend my appreciation to the colleagues and peers at the University of Sydney: Dr. Jianghui Zheng, Dr. Jueming Bing, Dr. Shi Tang, Dr. Christopher G. Bailey, Dr. Hongjun Chen, Dr. Guoliang Wang, Dr. Chwenhaw Liao, Mr. Tik Lun Peter Leung, Mr. Runmin Tao, Ms. Christine Kueh, and Mr. Mark Silver. Their valuable insights, research technical, and administrative support, and collaboration have played a crucial role in advancing my research in perovskite electronic devices. Beyond academic contributions, I am also deeply grateful for the encouragement, camaraderie, and stimulating discussions that have made my PhD journey both intellectually enriching and personally fulfilling. Their constant support and the positive, collaborative environment they have cultivated have been instrumental in making my time at the university truly memorable.

Many thanks to Dr. Justin Digweed from the Research & Prototype Foundry, Core Research Facilities at the University of Sydney, for his assistance associated with the CO_2 laser and for his invaluable guidance and support throughout my entire journey. I really appreciate his time and kind efforts: training, explaining, and exploring laser sources across campus.

I would also like to convey my sincere appreciation for the strong support from the professionals at the Design and Prototyping Workshop, Technical Support Services (TSS) at the University of Sydney, including Workshop Manager Dr. James Tawadros, Senior Technical Officer Mr. Nagaraja Panduranga, Project & Design Engineer Mr. Caleb Gudu, Technical Officer Mr. Poulose Arakkudiyil, Technical Officer Mr. Philip Gray, Technical Officer Mr. Peter Bracken, and Technical Officer Mr. Mike Zhong. I am very grateful for your swift and professional responses and your patience to my request. It has been a great pleasure working with you all in this joyful and relaxed environment.

I would like to thank my previous supervisor Prof. Guohua Xie from Xiamen University for his guidance for my Masters thesis. I would like to express my gratitude to my late father, Mr. Yongshan Yi, and my mother, Mrs. Qiuyue Lin, for their persistent love and continuous support throughout my life. Their encouragement has been invaluable in every step of the way. I am also profoundly grateful to my sister-in-law, Mrs. Charlie Lipeng Yi, an expert in PV industry, for her constant and loving support, which has been a source of strength and motivation. And, to my beloved wife, Mrs. Yanhong Chen, my heartfelt appreciation for your unconditional love, patience, and spiritual support throughout my PhD journey. Your unwavering belief in me has been my greatest driving force.

Lastly, my sincerest thanks to Yingxin Yi, Lingcai Yi, and Weijiang Xu for their incredible friendship and steadfast support during this entire period. Your presence has made this journey all the more meaningful.

List of Publications

As first-author:

1. **Jianpeng Yi**, Tik-Lun Leung, Justin Digweed, Jueming Bing, Christopher Bailey, Chwenhaw Liao, Runmin Tao, Guoliang Wang, Zhuofeng Li, Hieu T. Nguyen, Dane R. McCamey, Jianghui Zheng, Md Arafat Mahmud, Anita W. Y. Ho-Baillie. "CO_2 Laser Crystallization in Ambient for Highly Efficient $FAPbI_3$ Perovskite Solar Cells". Small, 2024, 20, 2402215.
2. **Jianpeng Yi**, Christopher Bailey, Tik-Lun Leung, Runmin Tao, Guoliang Wang, Jueming Bing, Md Arafat Mahmud, David R. Mckenzie, Anita W. Y. Ho-Baillie. "Efficient Ambient-All-Laser-Annealed Wide Bandgap Perovskite Solar Cells". Adv. Funct. Mater., 2025, 2503971.
3. **Jianpeng Yi**, Jueming Bing, Cheng-Yu Yeh, Christopher Bailey, Guoliang Wang, Runmin Tao, Tik-Lun Leung, Rajendra Kumar Gunasekaran, Dane R. McCamey, David R. Mckenzie, Chu-Chen Chueh, Md Arafat Mahmud, Anita W. Y. Ho-Baillie. "Efficient All Ambient-Laser-Annealed Perovskite-Organic-Photovoltaic Solar Cells". Adv. Funct. Mater., 2025, Accepted.

As co-author:

1. Md Arafat Mahmud, Jianghui Zheng, Jia-Fu Chang, Guoliang Wang, Chwenhaw Liao, Md Habibur Rahman, Walia Binte Tarique, Shi Tang, Jueming Bing, Christopher G. Bailey, Zhuofeng Li, Limei Yang, Nina Novikova, Tik Lun Leung, Hongjun Chen, **Jianpeng Yi**, Runmin Tao, Marko Jankovec, Stephen P. Bremner, Julie Cairney, Ashraf Uddin, Hieu T. Nguyen, Trevor Smith, Chu-Chen Chueh, Anita W. Y. Ho-Baillie. "Halogenated Polycyslic Aromatic Hydrocarbon for Hole Selective Layer/Perovskite Interface Modification and Passivation for Efficient Perovskite-Organic Tandem Solar Cells FOR Record Fill Factor", Adv. Energy Matter., 2024, 14, 2400691.
2. Guoliang Wang, Weiyuan Duan, Qing Lian, Md Arafat Mahmud, Tik Lun Leung, Chwenhaw Liao, Jueming Bing, Christopher Bailey, **Jianpeng Yi**, Runmin Tao, Jiong Yang, Xin Cui, Shuai Nie, Yan Zhu, Andreas Lambertz, Marko Jankovec, Marko Topič, Dane R. McCamey, Stephen Bremner, Ziv Hameiri, Kaining Ding, David Mckenzie, Jianghui Zheng, Anita Ho-Baillie. "Reducing Voltage Loss via Dipole Tuning for Electron-Transport in Efficient and Stable Perovskite-Silicon Tandem

Solar Cells", Adv. Energy Mater. 2024, 14, 2401029.

3. Chwenhaw Liao, Stefano Bernardi, Christopher G. Bailey, I. Hsiang Chao, Su-Ying Chien, Guoliang Wang, Yi-Hsuan Sun, Shi Tang, Jianghui Zheng, **Jianpeng Yi**, Ming-Hsuan Yu, Salvy P. Russo, Hung-Wei Yen, Dane R. McCamey, Brendan James Kennedy, Asaph Widmer-Cooper, Chu-Chen Chueh, Anita W. Y. Ho-Baillie. "Piperidine and (aminomethyl)pyridine series lead-free Dion–Jacobson phase tin perovskite single crystals and their applications for field-effect transistors", ACS Nano, 2024, 18, 22, 14176-14186.
4. Jianghui Zheng, Chaowei Xue, Guoliang Wang, Md Arafat Mahmud, Zhenyu Sun, Chwenhaw Liao, **Jianpeng Yi**, Jiangtao Qu, Limei Yang, Li Wang, Stephen Bremner, Julie M. Cairney, Jie Zhang, Anita W. Y. Ho-Baillie. "Efficient Flexible Monolithic Perovksite-CIGS Tandem Solar Cell on Conductive Steel Substrate". ACS Energy Lett., 9, 4, 1545-1547.
5. Guoliang Wang, Jianghui Zheng, Weiyuan Duan, Jiong Yang, Md Arafat Mahmud, Qing Lian, Shi Tang, Chwenhaw Liao, Jueming Bing, **Jianpeng Yi**, Tik-Lun Leung, Xin Cui, Hongjun Chen, Feng Jiang, Yulan Huang, Andreas Lambertz, Marko Jankovec, Marko Topic, Stephen Bremner, Yuan-Zhu Zhang, Chun Cheng, Kaining Ding, Anita Ho-Baillie. Joule, 7, 11, 2023, 2583-2594.
6. Md Arafat Mahmud, Jianghui Zheng, Shi Tang, Chwenhaw Liao, Guoliang Wang, Jueming Bing, Tik-Lun Leung, Anh Dinh Bui, Hongjun Chen, **Jianpeng Yi**, Stephen P. Bremner, Hieu T. Nguyen, A. W. Y. Ho-Baillie. Water-free, conductive hole transport layer for reproducible perovskite-perovskite tandems with record fill factor. ACS Energy Letters 8, 2022, 1, 21-30.

Abstract

Metal halide perovskite solar cells have attracted enormous research effort over the past two decades. While hot-plate annealing is common for perovskite crystallization, laser annealing is also promising. Most studies on laser annealing for solar cell fabrication focused on short-wavelength lasers, which can damage the perovskite layer.

This thesis focuses on the use of CO_2 laser with lower photon-energy in the mid-infrared (MIR) range for the annealing of i) formamidinium lead triiodide ($FAPbI_3$) perovskite with a bandgap of 1.53 eV; ii) (4-(3,6-Dimethyl-9H-carbazol-9-yl)butyl)phosphonic acid (Me-4PACz) hole transport layer (HTL); iii) 1.80 eV $FA_{0.8}Cs_{0.2}PbI_{1.8}Br_{1.2}$ perovskite; iv) 1.78 eV $FA_{0.8}Cs_{0.2}PbI_{1.8}Br_{1.2}$ perovskite with potassium hexafluorophosphate and cellulose acetate butyrate additives; v) and organic photovoltaic (OPV) absorber based on PM6:Y6 where PM6 is a donor–acceptor (D-A) copolymer composed of the 4,8-bis(5-(2-ethylhexyl)-4-fluorothiophen-2-yl)benzo[1,2-b:4,5-b′]dithiophene (BDT) and 1,3-bis(thiophen-2-yl)-5,7-bis(2-ethylhexyl)benzo-[1,2-c:4,5-c']dithiophene-4,8-dione (BDD) units and Y6 consists of dithienothiophen[3,2-b]-pyrrolobenzothiadiazole with 2-(5,6-Difluoro-3-oxo-2,3-dihydro-1H-inden-1-ylidene)malononitrile units.

All CO_2 laser annealing were performed in the ambient and all cell demonstrations using CO_2 laser annealing in this thesis were reported for the first time. Key findings of this thesis include:

1. Laser power is critical to α-$FAPbI_3$ phase formation, without driving out volatile organics from the perovskite nor increasing PbI_2 defects. Champion power conversion efficiency (PCE) of 21.8% achieved (without additional additives for perovskite bulk and surface passivations) was the highest for a laser annealed single-junction perovskite solar cell at the time.
2. COMSOL Multiphysics simulations of macroscopic and localised temperature profiles during laser annealing unveiled highly effective laser power absorption and cooling by the perovskite film, especially when compared to Me-4PACz, thereby lowering substrate temperature experienced compared to hot-plate annealing.
3. All laser annealed (HTL and perovskite) wide bandgap (1.80 eV) perovskite solar cell achieving a champion V_{OC} of 1.35 V and a PCE of 19.8%, highest for reported perovskite solar cells with the same bandgap at the time.
4. The first use of CO_2 laser for perovskite-OPV tandem solar cells. The laser annealed

PM6:Y6 OPV champion cell produced a PCE of 16.8%, highest for a laser annealed OPV cell at the time. The champion perovskite-OPV tandem produced a PCE of 24.0%, comparable to the state-of-the-art.

This thesis demonstrates the promising prospects of laser annealing offering time savings and localised heating advantage for temperature-sensitive substrates.

Table of Contents

Chapter 1 Introduction and Literature Review

1.1 Introduction

The consumption of fossil fuels such as coal, oil and gas has been the major contributor to CO_2 emission (**Figure 1.1**)[1] since late 19th century[2] . This in turn contributes to the global warming crisis, resulting in rapid climate change affecting habitat and safety. To address this issue, countries around the world have agreed to reduce the dependence on these carbon-emitting energy sources, aiming to reach net-zero carbon dioxide (CO_2) emissions by 2050.[3]

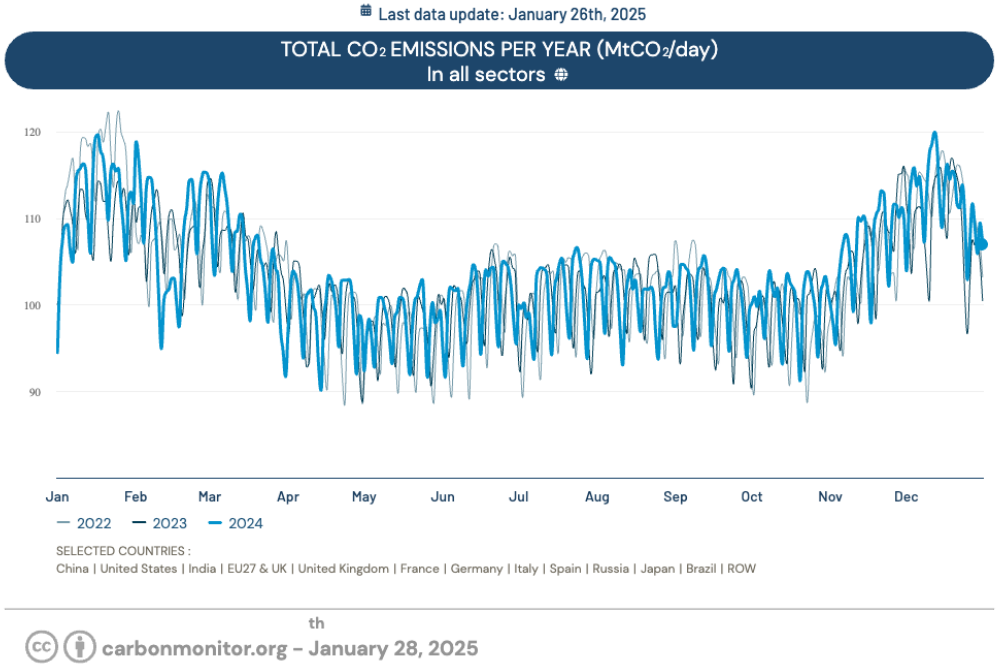

Figure 1.1 Total CO_2 emissions for years of 2022, 2023 and 2024.

Strengthening renewable energy development is one of the most promising ways to respond to the issue. Among various renewable energies, the cost solar photovoltaics (PV) has come down remarkably in the last decade, while performance improvement has been achieved at a slower pace compared to cost-reduction.[4] As of 2024, the global solar PV market was valued at USD 398.21 billion.[5] The annual solar photovoltaic installation rate is projected to be 1.7 TW/yr in 2030 and 3.4 TW/yr in 2037 for the accumulative capacity reaching 75 TW in 2050.[6]

Such growth has been driven by the silicon solar cell technology that will continue[6] to play a

crucial role in replacing fossil fuels. However, as power conversion efficiencies of silicon solar cells are reaching their theoretical limits at ~30%,[7] tandem technologies are being investigated to further increase power output to further bring the cost per watt down for the increasing demand for renewables.

Tandem solar cells involve the stacking of solar cells with different bandgaps (highest on the sun-facing side) allowing each cell to convert different parts of the solar spectrum to electricity more efficiently, minimizing sub-bandgap and thermalization losses.[7] The efficiency limit of 2-junction tandem therefore increases to~45% and for 3-junction tandem, the efficiency limit is ~51%.[7]

Technologies that are potentially useful for tandem are shown in **Figure 1.2**, in particular, the technologies that produce high power conversion efficiencies. Among them, metal halide perovskite solar cells have the required efficiencies and low cost potentials to be a contending technology. The performance improvement of metal halide perovskite solar cells is the most rapid compared to other technologies. (**Figure 1.3)** Since its first demonstration with an efficiency of 3.8%[8], the most efficient laboratory cell in the form of single junction is now 27.0%, which is comparable to silicon.[9]

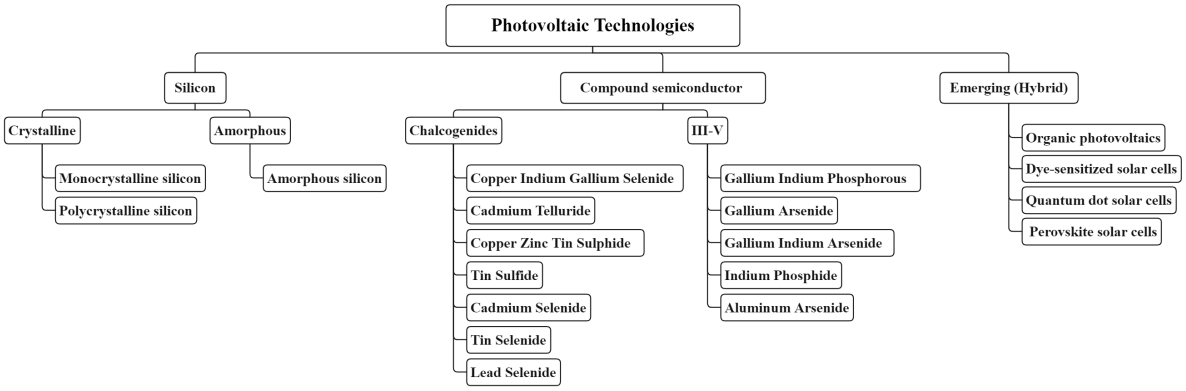

Figure 1.2 A summary of PV technologies.[10, 11]

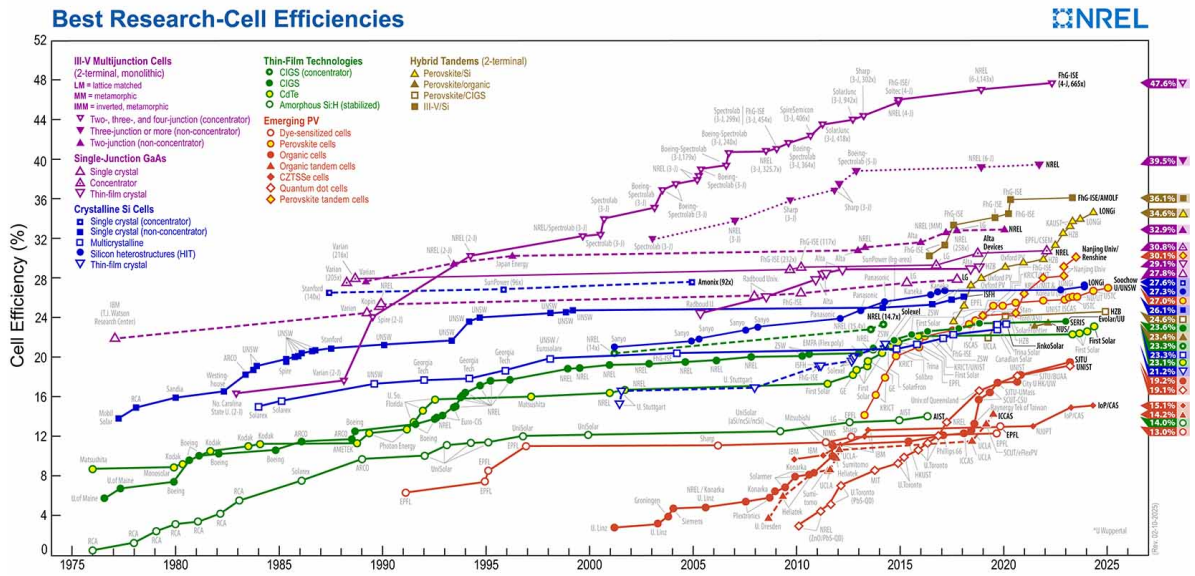

Figure 1.3 Record research cell efficiencies for major PV technologies. Accessed on 10th Mar. 2025. [9]

1.2 Metal halide perovskites

Metal halide perovskites are a class of crystalline materials with the general chemical formula ABX_3 as shown in **Figure 1.4**,[12] where A is an organic (e.g., methylammonium, formamidinium) or inorganic (e.g., caesium) cation; B is a metal cation (e.g, lead and/or tin); X is a halide anion (e.g., iodine, bromine, chlorine or a mixture).

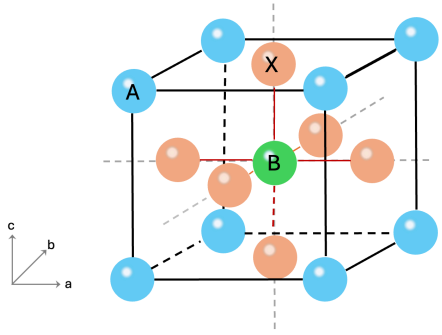

Figure 1.4 The perovskite crystal lattice with a chemical formula of ABX_3 .[12]

Metal halide perovskites, exhibit excellent properties for photovoltaics including high absorption coefficient,[13] long carrier diffusion length,[14] and low exciton binding energy if lower-dimensional or layered perovskites are involved[15]. The perovskite structure is also

versatile in the sense that the composition of the perovskite can be tuned by alternating the cations in the A- and B-sites or altering the anion in the X-site to form narrow bandgap (E_g) <1.5 eV, medium bandgap (1.5 eV ≤ E_g ≤ 1.7 eV), and wide bandgap (E_g >1.7 eV) perovskites making them suitable for tandems.[7] Therefore, a variety of perovskite-tandem devices have been demonstrated recently including perovskite-silicon tandems, perovskite-perovskite tandems, perovskite-organic tandems, perovskite-Copper Indium Gallium Diselenide (CIGS) tandems owing to perovskites' ease of fabrication. Many companies, such as LONGi, is actively investigating the commercial prospects of perovskite-silicon tandem.[16] Therefore, developing commercially viable manufacturing processes is important to ensure perovskite solar cell technology remains commercially competitive. This thesis will focus on the development of laser annealing for perovskite solar cells.

1.3 Laser annealing

Laser annealing is a highly versatile and proven technology with a long history of developments and applications.[17-19] It is a highly popular heating tool for a variety of industries for semiconductor,[20-24] photovoltaics,[19, 25-28] medical therapy,[29-34] and even fabrics production [35-38] amongst many others[28, 39-41]. Compared to traditional thermal annealing such as hot plate, furnace, oven annealing, laser annealing[17] offers rapid heating due to more efficient heat transfer and localized heating which is a distinctive advantage when patterning or heat sensitive materials are involved.[27, 42, 43]

Annealing is a critical factor in perovskite crystallization process, as it provides the activation energy for phase transition.[44] There are multiple heating strategies (**Table 1.1**) being utilized nowadays, including traditional hot-plate thermal annealing (TA),[45-47] microwave annealing (MA),[48-50] infrared lamp annealing (IRLA),[51, 52] intense pulsed light annealing (IPLA),[53, 54] flash infrared lamp annealing (FIRA) [55, 56] and laser annealing (LA).[57, 58] Among them, TA is extensively employed due to ease of access for research purposes producing cells with record efficiencies [59, 60] but has disadvantages such as low heating rate via heat-conduction thereby requiring long annealing time that generally take tens of minutes. Laser annealing on the other hand is non-contacting, highly localized or selective, with much less adverse thermal effects on adjacent functional layers and the substrate. [57] This is beneficial for heat-sensitive substrates. [61, 62] Research groups have reported laser annealing for perovskites [63-75] (**Table 1.2a**) and solar

cells [57, 58, 76-80] (**Table 1.2b**) with promising results.

Table 1.1 Annealing methods useful for metal halide perovskites and their potential advantages and disadvantages.

Annealing Method	**Advantages**	**Disadvantages**
Hot-plate	Ease of access for research purposes	Slow response rate Long heating time Non-uniform vertical heating Heating through substrate
Microwave	Short annealing time	Prone to non-uniform heating due to non-uniform field and heterogeneous material system
Infrared lamp	Short annealing time	Heat loss to non-inert ambient
Intense pulsed light annealing	Short annealing time	Damage by UV or high energy photons Heat loss to non-inert ambient
Flash infrared lamp	Short annealing time	Heat loss to non-inert ambient
Laser (UV-VIS-NIR)	Short annealing time Localised annealing possible	Raster scan style annealing may increase annealing time
Laser (CO_2)	Short annealing time Localised annealing possible Lower photon energy and therefore less harmful to the Pb-I bond in metal halide perovskites	Raster scan style annealing may increase annealing time

The first laser-annealed perovskite solar cells based on methyl ammonium lead iodide ($MAPbI_3$) in 2016 were reported by Jeon and Li et al. Jeon et.al [58] achieved a champion efficiency of 12.1% for inverted p-i-n device by using a near-infrared (NIR) laser with a wavelength of 1064 nm for $MAPbI_3$ crystallization (Table 1.2b). Four years later, Trinh et al. also reported the use of a 1064 nm laser for $MAPbI_3$ perovskite crystallization but this time it was for a n-i-p device. The champion device achieved a PCE of 13.0%.[79]

Using a blue-emitting laser (wavelength, 450 nm), Li et al.[76] reported a higher device efficiency of 17.8% based on n-i-p structure in 2016. In 2020, You et al. compared the use of diode lasers with 3 different wavelengths (405 nm, 450 nm, and 660 nm) for $MAPbI_3$ and $(CsPbI_3)_{0.05}(FAPbI_3)_{0.95}(MAPbBr_3)_{0.05}$ perovskite crystallization.[57] With the merits of laser annealing, such as high heating rate and high temperature gradient, lasered-films showed larger grains with better crystallinity, which contributed to higher device performance with a champion PCE of 21.5% comparing to 18.1% resulted from the thermally annealed counterpart. In other works,[77, 78, 80] researchers also reported the use of krypton fluoride (KrF) excimer laser (248nm) or a NIR laser (800 nm) or UV laser (355 nm) for "polishing" the perovskite layer via surface ablation post hot-plate annealing. Respectable efficiencies were achieved (last entries in **Table 1.2b**) although the laser processing used was not intended for annealing.

For the reports discussed above, UV lasers (248 nm, 355 nm), visible wavelength lasers (405 nm, 450 nm, 532 nm, 660 nm), and near infrared lasers (800 nm, 1064 nm) were frequently

used in perovskite treatments. Despite the encouraging results, these lasers have short wavelengths corresponding to high energies that can be detrimental to chemical bonds in the perovskite photo-absorber.[81] According to the literature reports, Pb-I bond is the most vulnerable within a perovskite with a dissociation energy as low as around 0.2 eV.[82-85] However, even for the widely-used NIR lasers as reported, the photon energy is around 1.17 eV, which is 5.8 times than the Pb-I bond dissociation energy. Therefore, lasers possessing both lower photon energies (namely, longer wavelengths) are preferred for laser-assisted perovskite crystallization. Carbon dioxide (CO_2) lasers with mid-infrared (MIR) emissions at higher power, on the other hand, produce much longer wavelengths (typically, 9.3 - 10.6 μm) and thus lower photon energy, as low as 0.12 eV, which are anticipated to be to compatible with perovskites.[86, 87] Moreover, CO_2 laser beams are highly thermally active due to its IR beam characteristics and as a heat source have been also used for other applications in the field of medicine and material engineering. To the best of our knowledge, CO_2 laser has not been used for perovskite before in the literature prior to this thesis.

Therefore, the utilisation of heat generated from CO_2 laser for perovskite annealing may have an advantage over short-wavelength lasers for the same purpose.

1.3.1 Laser annealing for formamidinium lead triiodide perovskites

Therefore, in this thesis, I will first develop a CO_2 laser process for the first time for perovskite film crystallisation and in particular for formamidinium lead triiodide ($FAPbI_3$) perovskite solar cells its bandgap at around 1.48 eV, which is closest to the theoretical optimum for single junction solar cell compared to other perovskite materials.[88]

1.3.2 Laser annealing modelling

To demonstrate the advantages of laser annealing in terms of time savings and lower substrate temperatures, I will model macroscopic and localised temperature profiles generated by laser annealing via a three-dimension (3D) finite element analysis model using COMSOL Multiphysics for the first time.

Laser annealing offers a highly controllable, non-contact method to precisely tailor film morphology and crystallinity, potentially overcoming existing limitations in WBG perovskites. In perovskite films, laser processing provides a rapid heating approach that can mitigate phase segregation while promoting high-quality crystallization.[89] By optimizing laser parameters, it may be possible to achieve finer control over halide distribution and defect passivation, further improving stability and V_{OC}. These advantages make laser annealing a promising tool for next-generation WBG perovskite solar cells, aiming for higher efficiencies and enhanced long-term operational stability.

1.3.3 Laser annealing for wide bandgap perovskites

Wide bandgap (WBG, energy gap E_g >1.7 eV) metal halide perovskites have attracted enormous research interest for multiple junction tandems[90,91] especially monolithic tandems that have wide bandgap (WBG) perovskite sub-cells directly deposited on top of Si, perovskite, CIGS, and organic photovoltaic sub-cells producing tandem cell power conversion efficiencies (PCEs) that surpass the highest efficiencies of the sub-cells.[92-100] Despite the impressive achievements, WBG perovskites are still facing severe open-circuit voltage losses whereby $W_{OC} = E_g/q\text{-}V_{OC}$, q is elementary charge and V_{OC} is open circuit voltage. Reasons for W_{OC} include non-radiative recombination, energy level misalignment and phase segregation. [101,102]

Non-radiative recombination can be suppressed by improving perovskite quality while a well-designed and appropriately fabricated hole transport layer (HTL) enables energy level alignment and perovskite/HTL interface with reduced surface passivation.[89,102-106] Laser annealing has been demonstrated to enhance perovskite crystallinity.[57, 58, 73, 107, 108] and for the fabrication of HTL such as NiO_X[109] and porous graphene electrode from poly(3,4-ethylenedioxythiophene) polystyrene sulfonate (PEDOT:PSS).[110] While self-assembly mono-layer (SAM) type HTLs have become popular in the state-of-the-art high efficiency perovskite single junction and tandem solar cells,[111-116] there has been no report on laser processing of SAM HTL for perovskite solar cells. While two-dimensional simulation models have been developed to understand heat transport,[79, 117] three-dimensional models are yet to be developed.

Therefore, in this thesis, I will develop a laser annealing processes for fabricating (4-(3,6-Dimethyl-9H-carbazol-9-yl)butyl)phosphonic acid (Me-4PACz) SAM HTL and WBG 1.80eV $FA_{0.8}Cs_{0.2}PbI_{1.8}Br_{1.2}$ perovskite layers.

1.3.4 Laser annealing for OPV and perovskite-OPV tandem

Perovskite-OPV tandem solar cells with a theoretical efficiency limit of 41% have attracted research interest over the years.[97, 118, 119] Since the perovskite and OPV cells are essentially prepared by coating, perovskite-OPV tandems can be manufactured as a continuous flexible arrays. This is challenging for perovskite-silicon tandems due to the rigidity and fragility of the silicon bottom cell.[96] Perovskite-OPV tandems do not suffer from the instability issue faced by perovskite-perovskite tandems, namely oxidation of narrow bandgap tin-base perovskite in the bottom cell.[119] There has been great progress in improving the efficiency for perovskite-OPV tandems, to the most recent certified value at 25.1% in 2024.[96] This was achieved via the incorporation of pseudo-halide thiocyanate in the precursor to suppress phase segregation that is otherwise commonly found in mixed iodide bromide perovskite[92, 121-125] for the fabrication of wide bandgap cells.

Therefore, in this thesis, I will demonstrate the use of ambient laser annealing for the fabrication of PM6:Y6 OPV and perovskite-OPV tandem solar cells for the first time. PM6 is a donor–acceptor (D-A) copolymer composed of the 4,8-bis(5-(2-ethylhexyl)-4-fluorothiophen-2-yl)benzo[1,2-b:4,5-b′]dithiophene (BDT) and 1,3-bis(thiophen-2-yl)-5,7-bis(2-ethylhexyl)benzo-[1,2-c:4,5-c']dithiophene-4,8-dione (BDD) units and Y6 consists of dithienothiophen[3,2-b]-pyrrolobenzothiadiazole with 2-(5,6-Difluoro-3-oxo-2,3-dihydro-1H-inden-1-ylidene)malononitrile units.

Table 1.2a Reported laser processed perovskite materials in the form of films, or nano-structures in different environment such as ambient, N_2 and dry air.

Year	Test structure	Perovskite	Treatment	Environment	laser λ (nm)	Ref
2016	glass/FTO/Perovskite	$FAPbI_3$	post illumination	Air	400	[63]
2017	Si/SiO_2/Perovskite	$MAPbBr_3$, $MAPbI_3$, $MAPbCl_3$	crystallization	Not reported	800	[64]
2018	glass/ITO/PEDOT:PSS or PTAA/Perovskite	$MAPbI_3$	crystallization	Nitrogen	532	[65]
2018	perovskite precursor solution	$MAPbX_3$ nano-crystals NCs	crystallization	Not reported	1,064	[73]
2018	glass/ITO/PEDOT:PSS	$MAPbBr_3$	crystallization	Not reported	808	[75]
2020	glass/PEDOT:PSS/Perovskite	$MAPbI_3$	crystallization	Not reported	1,064	[66]
2020	borosilicate glass matrix containing Cs, Pb, Br, & Cl	$CsPb(Cl/Br)_3$ NCs	crystallization	Not reported	800	[71]
2020	glass/ITO/Perovskite:CQD	$(Cs_{0.06}FA_{0.79}MA_{0.15})Pb(I_{0.85}Br_{0.15})_3$	crystallization	Air	1,064	[67]
2021	glass/Perovskite	$MAPbI_3$	crystallization	Not reported	405	[68]
2022	$CsPb_2Br_5$ single crystals	$CsPbBr_3$ NCs	convert $CsPb_2Br_5$ SCs to $CsPbBr_3$ NCs	Not reported	800	[70]
2022	quartz/perovskite	$CsPbBr_3$ NCs	crystallization	Ambient	355	[72]
2023	perovskite inside PVDF matrix (film)	$CsPbX_3$ NPs	crystallization	Not reported	405	[74]
2023	Perovskite on Au nano-islands	$MAPbBr_3$	crystallization	Not reported	800	[69]

Table 1.2b Reported laser processed perovskite in solar cells in different environment such as ambient, N_2 and dry air.

Year	Solar device	Perovskite	Treatment	Environment	laser λ (nm)	J_{SC} (mA/cm^2)	V_{OC} (V)	FF (%)	PCE (%)	Ref.
2016	glass/ITO/PEDOT:PSS/Perovskite/PCBM/Ca:Al	$MAPbI_3$	crystallization	Not reported	1,064	16.8	0.89	80.1	12.1	[58]
2016	glass/FTO/TiO_2/Perovskite/Spiro-OMeTAD/Au	$MAPbI_3$	crystallization	Not reported	450	22.8	1.15	68.0	17.8	[76]
2019	glass/FTO/TiO_2/Perovskite/Spiro-OMeTAD/Au	$MAPbI_3$	surface treatment post hot-plate crystallization	Not reported	248	23.7	1.13	72.6	19.4	[77]
2020	glass/ITO/PTAA:F4-TCNQ/Perovskite/PCBM/BCP/Ag	$Cs_{0.06}FA_{0.79}MA_{0.15}Pb(I_{0.85}Br_{0.15})_3$	surface polishing	Not reported	800	23.3	1.14	70.2	18.6	[78]
2020	glass/FTO/TiO_2/Perovskite/Spiro-OMeTAD/Au*	$MAPbI_3$	crystallization	Dry air	405	23.2	1.11	76.4	19.7	[57]
					450	23.3	1.12	77.3	20.2	[57]
					660	23.2	1.12	76.7	19.9	[57]
		$(CsPbI_3)_{0.05}(FAPbI_3)_{0.95}(MAPbBr_3)_{0.05}$			405	23.6	1.13	76.6	20.2	[57]
					450	23.6	1.14	77.4	20.8	[57]
					660	23.4	1.14	76.7	20.4	[57]
2020	glass/FTO/TiO_2/Perovskite/Spiro-OMeTAD/Ag*	$MAPbI_3$	crystallization	Not reported	1,064	20.9	0.93	65.0	12.5	[79]
2023	glass/ITO/SnO_2/Perovskite/Spiro-OMeTAD/Au	$MAPbI_3$	laser polishing	Ambient	355	21.0	1.19	77.3	19.3	[80]
		$Cs_{0.05}(MA_{0.17}FA_{0.83})_{0.95}Pb(I_{0.83}Br_{0.17})_3$				20.0	1.06	77.7	16.4	

* average rather than champion cell results are shown.

1.4 Thesis outline

Given the review above that outlines the motivations of the develop CO_2 laser annealing for perovskite solar cells, this thesis will be organised according to the below:

Chapter 2 reports CO_2 laser-assisted ambient crystallisation of $FAPbI_3$ for efficient solar cells.

Chapter 3 reports COMSOL simulation of temperature profiles of laser annealed perovskite and hole transport layers.

Chapter 4 reports all laser-annealed wide bandgap perovskite solar cells.

Chapter 5 reports laser-annealed organic photovoltaic (OPV) and perovskite-OPV tandem solar cells.

Chapter 6 concludes by highlighting originality, novelty and significance of this thesis.

1.5 References

(1) CarbonMonitor. Total CO_2 Emissions Per Year($MtCO_2$/day); Carbon Monitor, 16th Jan 2025. https://carbonmonitor.org/.

(2) NASA. The rate of change since the mid-20th century is unprecedented over millennia; NASA, 10th Mar 2025. https://science.nasa.gov/climate-change/evidence/.

(3) UnitedNations. Renewable energy – powering a safer future; United Nations, 10th Mar 2025. https://www.un.org/en/climatechange/raising-ambition/renewable-energy.

(4) VDMA. *International Technology Roadmap for Photovoltaics (ITRPV) 2023 Results*; May 2025. https://www.vdma.org/international-technology-roadmap-photovoltaic.

(5) CervicornConsulting. Solar Photovoltaic (PV) Market Size and Growth 2025 to 2034; Cervicorn Consulting, 15th Jan. 2025. https://www.cervicornconsulting.com/solar-photovoltaic-market.

(6) Haegel, N. M.; Verlinden, P.; Victoria, M.; Altermatt, P.; Atwater, H.; Barnes, T.; Breyer, C.; Case, C.; De Wolf, S.; Deline, C.; et al. Photovoltaics at multi-terawatt scale: Waiting is not an option. *Science* **2023**, *380* (6640), 39-42. DOI: 10.1126/science.adf6957.

(7) Ho-Baillie, A. W. Y.; Zheng, J.; Mahmud, M. A.; Ma, F.-J.; McKenzie, D. R.; Green, M. A. Recent progress and future prospects of perovskite tandem solar cells. *Applied Physics Reviews* **2021**, *8* (4), 041307. DOI: 10.1063/5.0061483.

(8) Kojima, A.; Teshima, K.; Shirai, Y.; Miyasaka, T. Organometal Halide Perovskites as Visible-Light Sensitizers for Photovoltaic Cells. *Journal of the American Chemical Society* **2009**, *131* (17), 6050-6051. DOI: 10.1021/ja809598r.

(9) NREL. Best Research-Cell Efficiency Chart. 10th Mar 2025, https://www.nrel.gov/pv/cell-efficiency.html.

(10) Pastuszak, J.; Węgierek, P. Photovoltaic Cell Generations and Current Research Directions for Their Development. *Materials* **2022**, *15* (16). DOI: 10.3390/ma15165542.

(11) Rathore, N.; Panwar, N. L.; Yettou, F.; Gama, A. A comprehensive review of different types of solar photovoltaic cells and their applications. *International Journal of Ambient Energy* **2021**, *42* (10), 1200-1217. DOI: 10.1080/01430750.2019.1592774.

(12) Akkerman, Q. A.; Manna, L. What Defines a Halide Perovskite? *ACS Energy Letters* **2020**, *5* (2), 604-610. DOI: 10.1021/acsenergylett.0c00039.

(13) Green, M. A.; Ho-Baillie, A.; Snaith, H. J. The emergence of perovskite solar cells. *Nature Photonics* **2014**, *8* (7), 506-514. DOI: 10.1038/nphoton.2014.134.

(14) Zhao, B.; Gillan, L. V.; Scully, A. D.; Chesman, A. S. R.; Tan, B.; Lin, X.; Liu, J.; Rietwyk, K. J.; Deng, S.; Bailey, C.; et al. Enhanced Carrier Diffusion Enables Efficient Back-Contact Perovskite Photovoltaics. *Angewandte Chemie International Edition* **2023**, *62* (27), e202218174. DOI: https://doi.org/10.1002/anie.202218174.

(15) Liao, C.-H.; Chen, C.-H.; Bing, J.; Bailey, C.; Lin, Y.-T.; Pandit, T. M.; Granados, L.; Zheng, J.; Tang, S.; Lin, B.-H.; et al. Inorganic-Cation Pseudohalide 2D $Cs_2Pb(SCN)_2Br_2$ Perovskite Single Crystal. *Advanced Materials* **2022**, *34* (7), 2104782. DOI: https://doi.org/10.1002/adma.202104782.

(16) LONGi. Record-breaker LONGi Once Again Sets a New World Efficiency for Silicon-perovskite Tandem Solar Cells; 18th Jun. **2024**. https://www.longi.com/en/news/2024-snec-silicon-perovskite-tandem-solar-cells-new-world-efficiency/.

(17) Liu, H.; Lin, W.; Hong, M.; Hybrid laser precision engineering of transparent hard materials: challenges, solutions and applications. *Light: Science & Appllication* **2021**, *10*, 162. DOI: https://doi.org/10.1038/s41377-021-00596-5.

(18) Bell, A. Review and analysis of laser annealing. *Rca Review* **1979**, *40* (3), 295.

(19) Simonds, B. J.; Meadows, H. J.; Misra, S.; Ferekides, C.; Dale, P. J.; Scarpulla, M. A. Laser processing for thin film chalcogenide photovoltaics: a review and prospectus. *Journal of Photonics for Energy* **2015**, *5* (1), 050999-050999. DOI: https://doi.org/10.1117/1.JPE.5.050999.

(20) Hertzberg, J. B.; Zhang, E. J.; Rosenblatt, S.; Magesan, E.; Smolin, J. A.; Yau, J.-B.; Adiga, V. P.; Sandberg, M.; Brink, M.; Chow, J. M.; et al. Laser-annealing Josephson junctions for yielding scaled-up superconducting quantum processors. *npj Quantum Information* **2021**, *7* (1), 129. DOI: 10.1038/s41534-021-00464-5.

(21) Lombardo, S. F.; Boninelli, S.; Cristiano, F.; Fisicaro, G.; Fortunato, G.; Grimaldi, M. G.; Impellizzeri, G.; Italia, M.; Marino, A.; Milazzo, R.; et al. Laser annealing in Si and Ge: Anomalous physical aspects and modeling approaches. *Materials Science in Semiconductor Processing* **2017**, *62*, 80-91. DOI: https://doi.org/10.1016/j.mssp.2016.10.047.

(22) Jin, S.; Hong, S.; Mativenga, M.; Kim, B.; Shin, H. H.; Park, J. K.; Kim, T.-W.; Jang, J. Low temperature polycrystalline silicon with single orientation on glass by blue laser annealing. *Thin Solid Films* **2016**, *616*, 838-841. DOI: https://doi.org/10.1016/j.tsf.2016.10.026.

(23) Huet, K.; Mazzamuto, F.; Tabata, T.; Toqué-Tresonne, I.; Mori, Y. Doping of semiconductor devices by Laser Thermal Annealing. *Materials Science in Semiconductor Processing* **2017**, *62*, 92-102. DOI: https://doi.org/10.1016/j.mssp.2016.11.008.

(24) Gluschenkov, O.; Jagannathan, H. (Invited) Laser Annealing in CMOS Manufacturing. *ECS Transactions* **2018**, *85* (6), 11. DOI: 10.1149/08506.0011ecst.

(25) Nielsen, R.; Hemmingsen, T. H.; Bonczyk, T. G.; Hansen, O.; Chorkendorff, I.; Vesborg, P. C. Laser-annealing and solid-phase epitaxy of selenium thin-film solar cells. *ACS Applied Energy Materials* **2023**, *6* (17), 8849-8856. DOI: https://doi.org/10.1021/acsaem.3c01464.

(26) Sinha, A.; Dasgupta, S.; Rohatgi, A.; Gupta, M. C. Rapid Thermal Annealing Effects on Passivation Quality of p-TOPCon Silicon Solar Cells. *IEEE Journal of Photovoltaics* **2024**. DOI: 10.1109/JPHOTOV.2023.3348239.

(27) Wilkes, G. C.; Upadhyaya, A. D.; Rohatgi, A.; Gupta, M. C. Laser crystallization and dopant activation of a-Si:H carrier-selective layer in TOPCon Si solar cells. *IEEE Journal of Photovoltaics* **2020**, *10* (5), 1283-1289. DOI: 10.1109/JPHOTOV.2020.3006273.

(28) Palina, N.; Mueller, T.; Mohanti, S.; Aberle, A. G. Laser assisted boron doping of silicon wafer solar cells using nanosecond and picosecond laser pulses. In *2011 37th IEEE Photovoltaic Specialists Conference*, **2011**; IEEE: pp 002193-002197. DOI: 10.1109/PVSC.2011.6186392.

(29) Farivar, S.; Malekshahabi, T.; Shiari, R. Biological effects of low level laser therapy. *Journal of lasers in medical sciences* **2014**, *5* (2), 58. DOI: https://journals.sbmu.ac.ir/jlms/article/view/5540.

(30) Hashmi, J. T.; Huang, Y. Y.; Osmani, B. Z.; Sharma, S. K.; Naeser, M. A.; Hamblin, M. R. Role of low-level laser therapy in neurorehabilitation. *Pm&r* **2010**, *2*, S292-S305. DOI: 10.1016/j.pmrj.2010.10.013.

(31) Anders, J. J.; Lanzafame, R. J.; Arany, P. R. Low-level light/laser therapy versus photobiomodulation therapy. *Photomedicine and laser surgery* **2015**, *33* (4), 183. DOI: 10.1089/pho.2015.9848.

(32) Loreti, E. H.; Pascoal, V. L. W.; Nogueira, B. V.; Silva, I. V.; Pedrosa, D. F. Use of laser therapy in the healing process: a literature review. *Photomedicine and laser surgery* **2015**, *33* (2), 104-116. DOI: 10.1089/pho.2014.3772.

(33) Omi, T.; Numano, K. The role of the CO_2 laser and fractional CO_2 laser in dermatology. *Laser therapy* **2014**, *23* (1), 49-60. DOI: 10.5978/islsm.14-RE-01.

(34) Athanasiou, S.; Pitsouni, E.; Antonopoulou, S.; Zacharakis, D.; Salvatore, S.; Falagas, M.; Grigoriadis, T. The effect of microablative fractional CO_2 laser on vaginal flora of postmenopausal women. *Climacteric* **2016**, *19* (5), 512-518. DOI: http://dx.doi.org/10.1080/13697137.2016.1212006.

(35) Chow, Y. F.; Chan, A.; Kan, C.-w. Effect of CO_2 laser irradiation on the properties of cotton fabric. *Textile Research Journal* **2012**, *82* (12), 1220-1234. DOI: https://doi.org/10.1177/0040517511429609.

(36) Kan, C. W.; Yuen, C.; Cheng, C. Technical study of the effect of CO_2 laser surface engraving on the colour properties of denim fabric. *Coloration Technology* **2010**, *126* (6), 365-371. DOI: https://doi.org/10.1111/j.1478-4408.2010.00270.x.

(37) Dalbaşı, E. S.; İlleez, A. A.; A research on the effect of various laser fading parameters on physical and surface properties of denim fabric. *Optics & Laser Technology* **2019**, *118*, 28-36. DOI: https://doi.org/10.1016/j.optlastec.2019.04.030.

(38) Tunakova, V.; Hrubosova, Z.; Tunak, M.; Kasparova, M.; Mullerova, J. Laser surface modification of electrically conductive fabrics: Material performance improvement and design effects. *Optics & Laser Technology* **2018**, *98*, 178-189. DOI: https://doi.org/10.1016/j.optlastec.2017.07.017.

(39) Chakraborty, A.; Gottumukkala, N. R.; Gupta, M. C. Superhydrophobic surface by laser ablation of PDMS. *Langmuir* **2023**, *39* (32), 11259-11267. DOI: https://doi.org/10.1021/acs.langmuir.3c00818.

(40) Aryal, A.; Bulcha, B.; Sinha, A.; Chakraborty, A.; Hewagama, T.; Gupta, M. C. Effects of laser ablation of olivine on chamber optical window transmission loss and its recovery. *Journal of Laser Applications* **2024**, *36* (3), 032033. DOI: https://doi.org/10.2351/7.0001521.

(41) Vrancken, B.; Thijs, L.; Kruth, J.-P.; Van Humbeeck, J. Heat treatment of Ti_6Al_4V produced by Selective Laser Melting: Microstructure and mechanical properties. *Journal of Alloys and Compounds* **2012**, *541*, 177-185. DOI: https://doi.org/10.1016/j.jallcom.2012.07.022.

(42) Kong, H.; Kwon, J.; Paeng, D.; Jung, W. J.; Ghimire, S.; Dho, J.; Yoo, J.-H.; Hong, S.; Jung, J.; Shin, J. Laser-induced crystalline-phase transformation for hematite nanorod photoelectrochemical cells. *ACS applied materials & interfaces* **2020**, *12* (43), 48917-48927. DOI: https://doi.org/10.1021/acsami.0c11999.

(43) Liu, X.; Islam, A.; Yang, N.; Odhner, B.; Tupta, M. A.; Guo, J.; Feng, P. X.-L. Atomic layer $MoTe_2$ field-effect transistors and monolithic logic circuits configured by scanning laser annealing. *ACS nano* **2021**, *15* (12), 19733-19742. DOI: https://doi.org/10.1021/acsnano.1c07169.

(44) Bi, L.; Fu, Q.; Zeng, Z.; Wang, Y.; Lin, F. R.; Cheng, Y.; Yip, H.-L.; Tsang, S. W.; Jen, A. K. Y. Deciphering the Roles of MA-Based Volatile Additives for α-$FAPbI_3$ to Enable Efficient Inverted Perovskite Solar Cells. *Journal of the American Chemical Society* **2023**, *145* (10), 5920-5929. DOI: 10.1021/jacs.2c13566.

(45) Chen, H.; Chen, Y.; Zhang, T.; Liu, X.; Wang, X.; Zhao, Y. Advances to High-Performance Black-Phase $FAPbI_3$ Perovskite for Efficient and Stable Photovoltaics. *Small Structures* **2021**, *2* (5), 2000130. DOI: https://doi.org/10.1002/sstr.202000130.

(46) Kim, M.; Kim, G.-H.; Lee, T. K.; Choi, I. W.; Choi, H. W.; Jo, Y.; Yoon, Y. J.; Kim, J. W.; Lee, J.; Huh, D.; et al. Methylammonium Chloride Induces Intermediate Phase Stabilization for Efficient Perovskite Solar Cells. *Joule* **2019**, *3* (9), 2179-2192. DOI: https://doi.org/10.1016/j.joule.2019.06.014.

(47) Chen, R.; Wang, J.; Liu, Z.; Ren, F.; Liu, S.; Zhou, J.; Wang, H.; Meng, X.; Zhang, Z.; Guan, X.; et al. Reduction of bulk and surface defects in inverted methylammonium- and bromide-free formamidinium perovskite solar cells. *Nature Energy* **2023**, *8* (8), 839-849. DOI: 10.1038/s41560-023-01288-7.

(48) Barua, P.; In, C. M.; Lee, M. J.; Hwang, I. Microwave-facilitated crystal growth of defect-passivated triple-cation metal halide perovskites toward efficient solar cells. *Nanoscale* **2023**, *15* (12), 5954-5963. DOI: 10.1039/D2NR07090A.

(49) Chen, Q.; Ma, T.; Wang, F.; Liu, Y.; Liu, S.; Wang, J.; Cheng, Z.; Chang, Q.; Yang, R.; Huang, W.; et al. Rapid Microwave-Annealing Process of Hybrid Perovskites to Eliminate

Miscellaneous Phase for High Performance Photovoltaics. *Advanced Science* **2020**, *7* (12), 2000480. DOI: https://doi.org/10.1002/advs.202000480.

(50) Wang, K.-L.; Zhang, C.-C.; Jiang, Y.-R.; Liu, H.-R.; Li, X.-M.; Jain, S. M.; Ma, H. High-quality perovskite films via post-annealing microwave treatment. *New Journal of Chemistry* **2019**, *43* (24), 9338-9344. DOI: 10.1039/C8NJ05941A.

(51) Wang, G.; Lian, Q.; Wang, D.; Jiang, F.; Mi, G.; Li, D.; Huang, Y.; Wang, Y.; Yao, X.; Shi, R.; et al. Thermal-Radiation-Driven Ultrafast Crystallization of Perovskite Films Under Heavy Humidity for Efficient Inverted Solar Cells. *Advanced Materials* **2022**, *34* (38), 2205143. DOI: https://doi.org/10.1002/adma.202205143.

(52) Huang, S.-H.; Guan, C.-K.; Lee, P.-H.; Huang, H.-C.; Li, C.-F.; Huang, Y.-C.; Su, W.-F. Toward All Slot-Die Fabricated High Efficiency Large Area Perovskite Solar Cell Using Rapid Near Infrared Heating in Ambient Air. *Advanced Energy Materials* **2020**, *10* (37), 2001567. DOI: https://doi.org/10.1002/aenm.202001567.

(53) Ghahremani, A. H.; Martin, B.; Gupta, A.; Bahadur, J.; Ankireddy, K.; Druffel, T. Rapid fabrication of perovskite solar cells through intense pulse light annealing of SnO_2 and triple cation perovskite thin films. *Materials & Design* **2020**, *185*, 108237. DOI: https://doi.org/10.1016/j.matdes.2019.108237.

(54) Chandrasekhar, P. S.; Chapagain, S.; Blake, M.; Armstrong, P. J.; Grapperhaus, C.; Druffel, T. L. Rapid scalable fabrication of roll-to-roll slot-die coated flexible perovskite solar cells using intense pulse light annealing. *Sustainable Energy & Fuels* **2022**, *6* (23), 5316-5323. DOI: 10.1039/D2SE00911K.

(55) Serafini, P.; Boix, P. P.; Barea, E. M.; Edvinson, T.; Sánchez, S.; Mora-Seró, I. Photonic Processing of MAPbI3 Films by Flash Annealing and Rapid Growth for High-Performance Perovskite Solar Cells. *Solar RRL* **2022**, *6* (12), 2200641. DOI: https://doi.org/10.1002/solr.202200641.

(56) Sanchez, S.; Hua, X.; Phung, N.; Steiner, U.; Abate, A. Flash Infrared Annealing for Antisolvent-Free Highly Efficient Perovskite Solar Cells. *Advanced Energy Materials* **2018**, *8* (12), 1702915. DOI: https://doi.org/10.1002/aenm.201702915.

(57) You, P.; Li, G.; Tang, G.; Cao, J.; Yan, F. Ultrafast laser-annealing of perovskite films for efficient perovskite solar cells. *Energy & Environmental Science* **2020**, *13* (4), 1187-1196. DOI: 10.1039/C9EE02324K.

(58) Jeon, T.; Jin, H. M.; Lee, S. H.; Lee, J. M.; Park, H. I.; Kim, M. K.; Lee, K. J.; Shin, B.; Kim, S. O. Laser Crystallization of Organic–Inorganic Hybrid Perovskite Solar Cells. *ACS Nano* **2016**, *10* (8), 7907-7914. DOI: 10.1021/acsnano.6b03815.

(59) Park, J.; Kim, J.; Yun, H.-S.; Paik, M. J.; Noh, E.; Mun, H. J.; Kim, M. G.; Shin, T. J.; Seok, S. I. Controlled growth of perovskite layers with volatile alkylammonium chlorides. *Nature* **2023**, *616* (7958), 724-730. DOI: 10.1038/s41586-023-05825-y.

(60) Zhang, S.; Ye, F.; Wang, X.; Chen, R.; Zhang, H.; Zhan, L.; Jiang, X.; Li, Y.; Ji, X.; Liu, S.; et al. Minimizing buried interfacial defects for efficient inverted perovskite solar cells. *Science* **2023**, *380* (6643), 404-409. DOI: 10.1126/science.adg3755.

(61) Zhang, M.; Wilkinson, B.; Liao, Y.; Zheng, J.; Lau, C. F. J.; Kim, J.; Bing, J.; Green, M. A.; Huang, S.; Ho-Baillie, A. W.-Y. Electrode Design to Overcome Substrate Transparency Limitations for Highly Efficient 1 cm^2 Mesoscopic Perovskite Solar Cells. *Joule* **2018**, *2* (12), 2694-2705. DOI: https://doi.org/10.1016/j.joule.2018.08.012.

(62) Gong, J.; Liang, J.; Sumathy, K. Review on dye-sensitized solar cells (DSSCs): Fundamental concepts and novel materials. *Renewable and Sustainable Energy Reviews* **2012**, *16* (8), 5848-5860. DOI: https://doi.org/10.1016/j.rser.2012.04.044.

(63) Fang, H.-H.; Wang, F.; Adjokatse, S.; Zhao, N.; Loi, M. A. Photoluminescence Enhancement in Formamidinium Lead Iodide Thin Films. *Advanced Functional Materials* **2016**, *26* (26), 4653-4659. DOI: https://doi.org/10.1002/adfm.201600715.

(64) Arciniegas, M. P.; Castelli, A.; Piazza, S.; Dogan, S.; Ceseracciu, L.; Krahne, R.; Duocastella, M.; Manna, L. Laser-Induced Localized Growth of Methylammonium Lead Halide Perovskite Nano- and Microcrystals on Substrates. *Advanced Functional Materials* **2017**, *27* (34), 1701613. DOI: https://doi.org/10.1002/adfm.201701613.

(65) Konidakis, I.; Maksudov, T.; Serpetzoglou, E.; Kakavelakis, G.; Kymakis, E.; Stratakis, E. Improved Charge Carrier Dynamics of $CH_3NH_3PbI_3$ Perovskite Films Synthesized by

Means of Laser-Assisted Crystallization. *ACS Applied Energy Materials* **2018**, *1* (9), 5101-5111. DOI: 10.1021/acsaem.8b01152.

(66) Song, C.; Tong, L.; Liu, F.; Ye, L.; Cheng, G. J. Addressing the Reliability and Electron Transport Kinetics in Halide Perovskite Film via Pulsed Laser Engineering. *Advanced Functional Materials* **2020**, *30* (5), 1906781. DOI: https://doi.org/10.1002/adfm.201906781.

(67) Song, C.; Yang, H.; Liu, F.; Ye, L.; Cheng, G. J. Quantum Dot Enabled Perovskite Thin Film with Enhanced Crystallization, Stability, and Carrier Diffusion via Pulsed Laser Nanoengineering. *Advanced Materials Interfaces* **2020**, *7* (20), 2001021. DOI: https://doi.org/10.1002/admi.202001021.

(68) Chen, X.; Wang, Z.; Wu, R.-J.; Cheng, H.-L.; Chui, H.-C. Laser-Induced Thermal Annealing of $CH_3NH_3PbI_3$ Perovskite Microwires. *Photonics* **2021**, *8* (2), 30. DOI: https://doi.org/10.3390/photonics8020030.

(69) Chen, J.; Yang, J.; Zhuang, W.; He, X.; Li, S.; Lin, Z.; Lan, S. Laser-induced controllable crystallization of organic-inorganic hybrid perovskites assisted by gold nanoislands. *Opt. Mater. Express* **2023**, *13* (2), 538-552. DOI: 10.1364/OME.479485.

(70) Li, M.; Yang, D.; Huang, X.; Zhang, H.; Zhao, Y.; Yin, B.; Pan, Q.; Kang, J.; Zheng, N.; Liu, X.; et al. Coupling Localized Laser Writing and Nonlocal Recrystallization in Perovskite Crystals for Reversible Multidimensional Optical Encryption. *Advanced Materials* **2022**, *34* (26), 2201413. DOI: https://doi.org/10.1002/adma.202201413.

(71) Huang, X.; Guo, Q.; Kang, S.; Ouyang, T.; Chen, Q.; Liu, X.; Xia, Z.; Yang, Z.; Zhang, Q.; Qiu, J.; et al. Three-Dimensional Laser-Assisted Patterning of Blue-Emissive Metal Halide Perovskite Nanocrystals inside a Glass with Switchable Photoluminescence. *ACS Nano* **2020**, *14* (3), 3150-3158. DOI: 10.1021/acsnano.9b08314.

(72) Shi, Y.; Li, R.; Yin, G.; Zhang, X.; Yu, X.; Meng, B.; Wei, Z.; Chen, R. Laser-Induced Secondary Crystallization of CsPbBr3 Perovskite Film for Robust and Low Threshold Amplified Spontaneous Emission. *Advanced Functional Materials* **2022**, *32* (49), 2207206. DOI: https://doi.org/10.1002/adfm.202207206.

(73) Yuyama, K.-i.; Islam, M. J.; Takahashi, K.; Nakamura, T.; Biju, V. Crystallization of Methylammonium Lead Halide Perovskites by Optical Trapping. *Angewandte Chemie International Edition* **2018**, *57* (41), 13424-13428. DOI: https://doi.org/10.1002/anie.201806079.

(74) Nie, L.; Wang, T.; Yu, X.; Gao, W.; Peng, Q.; Xia, Z.; Qiu, J.; Yu, S. F.; Xu, X. Multicolor Display Fabricated via Stacking CW Laser-Patterned Perovskite Films. *ACS Energy Letters* **2023**, *8* (4), 2025-2032. DOI: 10.1021/acsenergylett.3c00134.

(75) Kim, S. J.; Byun, J.; Jeon, T.; Jin, H. M.; Hong, H. R.; Kim, S. O. Perovskite Light-Emitting Diodes via Laser Crystallization: Systematic Investigation on Grain Size Effects for Device Performance. *ACS Applied Materials & Interfaces* **2018**, *10* (3), 2490-2495. DOI: 10.1021/acsami.7b15470.

(76) Li, F.; Zhu, W.; Bao, C.; Yu, T.; Wang, Y.; Zhou, X.; Zou, Z. Laser-assisted crystallization of $CH_3NH_3PbI_3$ films for efficient perovskite solar cells with a high open-circuit voltage. *Chemical Communications* **2016**, *52* (31), 5394-5397. DOI: 10.1039/C6CC00753H.

(77) Shan, X.; Wang, S.; Dong, W.; Pan, N.; Shao, J.; Wang, X.; Tao, R.; Deng, Z.; Hu, L.; Kong, F.; et al. Flash Surface Treatment of $CH_3NH_3PbI_3$ Films Using 248 nm KrF Excimer Laser Enhances the Performance of Perovskite Solar Cells. *Solar RRL* **2019**, *3* (7), 1900020. DOI: https://doi.org/10.1002/solr.201900020.

(78) Kong, W.; Zhao, C.; Xing, J.; Zou, Y.; Huang, T.; Li, F.; Yang, J.; Yu, W.; Guo, C. Enhancing Perovskite Solar Cell Performance through Femtosecond Laser Polishing. *Solar RRL* **2020**, *4* (7), 2000189. DOI: https://doi.org/10.1002/solr.202000189.

(79) Trinh, X.-L.; Tran, N.-H.; Seo, H.; Kim, H.-C. Enhanced performance of perovskite solar cells via laser-induced heat treatment on perovskite film. *Solar Energy* **2020**, *206*, 301-307. DOI: https://doi.org/10.1016/j.solener.2020.05.063.

(80) Kedia, M.; Rai, M.; Phirke, H.; Aranda, C. A.; Das, C.; Chirvony, V.; Boehringer, S.; Kot, M.; Byranvand, M. M.; Flege, J. I.; et al. Light Makes Right: Laser Polishing for Surface Modification of Perovskite Solar Cells. *ACS Energy Letters* **2023**, *8* (6), 2603-2610. DOI: 10.1021/acsenergylett.3c00469.

(81) Blanksby, S. J.; Ellison, G. B. Bond Dissociation Energies of Organic Molecules. *Accounts of Chemical Research* **2003**, *36* (4), 255-263. DOI: 10.1021/ar020230d.

(82) Liu, J.; Phillips, A. E.; Keen, D. A.; Dove, M. T. Thermal Disorder and Bond Anharmonicity in Cesium Lead Iodide Studied by Neutron Total Scattering and the Reverse Monte Carlo Method. *The Journal of Physical Chemistry C* **2019**, *123* (24), 14934-14940. DOI: 10.1021/acs.jpcc.9b02936.

(83) Kang, J.; Wang, L.-W. High Defect Tolerance in Lead Halide Perovskite $CsPbBr_3$. *The Journal of Physical Chemistry Letters* **2017**, *8* (2), 489-493. DOI: 10.1021/acs.jpclett.6b02800.

(84) Golovynskyi, S.; Datsenko, O. I.; Usman, M.; Pérez-Jiménez, A. I.; Chaigneau, M.; Bosi, M.; Seravalli, L.; Hidouri, T.; Golovynska, I.; Li, B.; et al. Free exciton and bound excitons on Pb and I vacancies and O and I substituting defects in PbI_2: Photoluminescence and DFT calculations. *Applied Surface Science* **2023**, *624*, 157128. DOI: https://doi.org/10.1016/j.apsusc.2023.157128.

(85) Kumar, S.; Mishra, T.; Sahu, R. K. Mechanical-load and temperature-engendered degradation of α-CsPbI3: reactive molecular dynamics simulation. *Journal of Materials Chemistry C* **2022**, *10* (33), 12091-12105. DOI: 10.1039/D2TC02298B.

(86) Yu, Y.; Wan, C.; Lv, Y.; Tan, R.; Zhou, J.; Liu, S.; Zhao, C. A 3kW average power tunable TEA CO_2 laser. *Optics & Laser Technology* **2005**, *37* (7), 560-562. DOI: https://doi.org/10.1016/j.optlastec.2004.08.011.

(87) Haberberger, D.; Tochitsky, S.; Joshi, C. Fifteen terawatt picosecond CO_2 laser system. *Opt. Express* **2010**, *18* (17), 17865-17875. DOI: 10.1364/OE.18.017865.

(88) Song C.; Lou S.; Deng S.; Li M.; Xin J; Liang Q; Liu J. Mitigating Ion Migration in a Mixed-Halide Perovskite via Laser Shock Annealing. *The Journal of Physical Chemistry Letters* **2025**, 16 (40), 10345-54. DOI: https://doi.org/10.1021/acs.jpclett.5c02594

(89) Bremner, S. P.; Yi, C.; Almansouri, I.; Ho-Baillie, A.; Green, M. A. Corrigendum to "Optimum band gap combinations to make best use of new photovoltaic materials", *Solar Energy* **2017**, *150*, 621. DOI: https://doi.org/10.1016/j.solener.2017.05.050.

(90) Jiang, Q.; Tong, J.; Scheidt, R. A.; Wang, X.; Louks, A. E.; Xian, Y.; Tirawat, R.; Palmstrom, A. F.; Hautzinger, M. P.; Harvey, S. P.; et al. Compositional texture engineering for highly stable wide-bandgap perovskite solar cells. *Science* **2022**, *378* (6626), 1295-1300. DOI: 10.1126/science.adf0194.

(91) Wu, S.; Yan, Y.; Yin, J.; Jiang, K.; Li, F.; Zeng, Z.; Tsang, S.-W.; Jen, A. K. Y. Redox mediator-stabilized wide-bandgap perovskites for monolithic perovskite-organic tandem solar cells. *Nature Energy* **2024**, *9* (4), 411-421. DOI: 10.1038/s41560-024-01451-8.

(92) Brinkmann, K. O.; Wang, P.; Lang, F.; Li, W.; Guo, X.; Zimmermann, F.; Olthof, S.; Neher, D.; Hou, Y.; Stolterfoht, M.; et al. Perovskite–organic tandem solar cells. *Nature Reviews Materials* **2024**, *9* (3), 202-217. DOI: 10.1038/s41578-023-00642-1.

(93) Chen, W.; Zhu, Y.; Xiu, J.; Chen, G.; Liang, H.; Liu, S.; Xue, H.; Birgersson, E.; Ho, J. W.; Qin, X.; et al. Monolithic perovskite/organic tandem solar cells with 23.6% efficiency enabled by reduced voltage losses and optimized interconnecting layer. *Nature Energy* **2022**, *7* (3), 229-237. DOI: 10.1038/s41560-021-00966-8.

(94) Brinkmann, K. O.; Becker, T.; Zimmermann, F.; Kreusel, C.; Gahlmann, T.; Theisen, M.; Haeger, T.; Olthof, S.; Tückmantel, C.; Günster, M.; et al. Perovskite–organic tandem solar cells with indium oxide interconnect. *Nature* **2022**, *604* (7905), 280-286. DOI: 10.1038/s41586-022-04455-0.

(95) Jiang, S.; Wang, R.; Li, M.; Yu, R.; Wang, F.; Tan, Z. a. Synergistic electrical and light management enables efficient monolithic inorganic perovskite/organic tandem solar cells with over 24% efficiency. *Energy & Environmental Science* **2024**, *17* (1), 219-226. DOI: 10.1039/D3EE02940A.

(96) Zhang, Z.; Chen, W.; Jiang, X.; Cao, J.; Yang, H.; Chen, H.; Yang, F.; Shen, Y.; Yang, H.; Cheng, Q.; et al. Suppression of phase segregation in wide-bandgap perovskites with thiocyanate ions for perovskite/organic tandems with 25.06% efficiency. *Nature Energy* **2024**, *9* (5), 592-601. DOI: 10.1038/s41560-024-01491-0.

(97) Ho-Baillie, A. W. Y.; Zheng, J.; Mahmud, M. A.; Ma, F.-J.; McKenzie, D. R.; Green, M. A. Recent progress and future prospects of perovskite tandem solar cells. *Applied Physics Reviews* **2021**, *8* (4). DOI: 10.1063/5.0061483 (accessed 2/4/2025).

(98) Jiang, X.; Qin, S.; Meng, L.; He, G.; Zhang, J.; Wang, Y.; Zhu, Y.; Zou, T.; Gong, Y.; Chen, Z.; et al. Isomeric diammonium passivation for perovskite–organic tandem solar cells. *Nature* **2024**, *635* (8040), 860-866. DOI: 10.1038/s41586-024-08160-y.

(99) Almora, O.; Bazan, G. C.; Cabrera, C. I.; Castriotta, L. A.; Erten-Ela, S.; Forberich, K.; Fukuda, K.; Guo, F.; Hauch, J.; Ho-Baillie, A. W. Y.; et al. Device Performance of Emerging Photovoltaic Materials (Version 5). *Advanced Energy Materials* ***2024***, 2404386. DOI: https://doi.org/10.1002/aenm.202404386.

(100) Laboratory, N. R. E. best-research-cell-efficiencies. **2025**.

(101) Fang, Z.; Nie, T.; Liu, S.; Ding, J. Overcoming Phase Segregation in Wide-Bandgap Perovskites: from Progress to Perspective. *Advanced Functional Materials* ***2024***, 34(42) 2404402. DOI: https://doi.org/10.1002/adfm.202404402.

(102) Yi, Z.; Wang, W.; He, R.; Zhu, J.; Jiao, W.; Luo, Y.; Xu, Y.; Wang, Y.; Zeng, Z.; Wei, K.; et al. Achieving a high open-circuit voltage of 1.339 V in 1.77 eV wide-bandgap perovskite solar cells via self-assembled monolayers. *Energy & Environmental Science* **2024**, *17* (1), 202-209. DOI: 10.1039/D3EE02839A.

(103) Lin, J.; Huang, R.; Peng, X.; Zhang, J.; Zhang, G.; Wang, W.; Pan, Z.; Rao, H.; Zhong, X. Eliminating Hole Extraction Barrier in 1D/3D Perovskite Heterojunction for Efficient and Stable Carbon-Based CsPbI3 Solar Cells with a Record Efficiency. *Advanced Materials* **2024**, *36* (33), 2404561. DOI: https://doi.org/10.1002/adma.202404561.

(104) Cui, H.; Huang, L.; Zhou, S.; Wang, C.; Hu, X.; Guan, H.; Wang, S.; Shao, W.; Pu, D.; Dong, K.; et al. Lead halide coordination competition at buried interfaces for low V_{OC}-deficits in wide-bandgap perovskite solar cells. *Energy & Environmental Science* **2023**, *16* (12), 5992-6002. DOI: 10.1039/D3EE02818F.

(105) Li, S.; Zheng, Z.; Ju, J.; Cheng, S.; Chen, F.; Xue, Z.; Ma, L.; Wang, Z. A Generic Strategy to Stabilize Wide Bandgap Perovskites for Efficient Tandem Solar Cells. *Advanced Materials* **2024**, *36* (9), 2307701. DOI: https://doi.org/10.1002/adma.202307701.

(106) Wen, J.; Zhao, Y.; Liu, Z.; Gao, H.; Lin, R.; Wan, S.; Ji, C.; Xiao, K.; Gao, Y.; Tian, Y.; et al. Steric Engineering Enables Efficient and Photostable Wide-Bandgap Perovskites for All-

Perovskite Tandem Solar Cells. *Advanced Materials* **2022**, *34* (26), 2110356. DOI: https://doi.org/10.1002/adma.202110356.

(107) Yang, H.; Peng, M.; Yi, W.; Jiang, H.; Cheng, G. J. Oriented Perovskite Film from Laser Recrystallization in Magnetic Field. *Advanced Materials* **2023**, *35* (45), 2303635. DOI: https://doi.org/10.1002/adma.202303635.

(108) Yi, J.; Leung, T.-L.; Digweed, J.; Bing, J.; Bailey, C.; Liao, C.; Tao, R.; Wang, G.; Li, Z.; Nguyen, H. T.; et al. CO_2 Laser Crystallization in Ambient for Highly Efficient $FAPbI_3$ Perovskite Solar Cells. *Small 2024*, 20 (45) 2402215. DOI: https://doi.org/10.1002/smll.202402215.

(109) Park, J. H.; Seo, J.; Park, S.; Shin, S. S.; Kim, Y. C.; Jeon, N. J.; Shin, H.-W.; Ahn, T. K.; Noh, J. H.; Yoon, S. C.; et al. Efficient $CH_3NH_3PbI_3$ Perovskite Solar Cells Employing Nanostructured p-Type NiO Electrode Formed by a Pulsed Laser Deposition. *Advanced Materials* **2015**, *27* (27), 4013-4019. DOI: https://doi.org/10.1002/adma.201500523.

(110) Chu, Z.; Liu, C.; Lu, Y. Laser-induced porous graphene from PEDOT:PSS films for dye-sensitized solar cells. *Materials Letters* **2022**, *323*, 132537. DOI: https://doi.org/10.1016/j.matlet.2022.132537.

(111) Tang, H.; Shen, Z.; Shen, Y.; Yan, G.; Wang, Y.; Han, Q.; Han, L. Reinforcing self-assembly of hole transport molecules for stable inverted perovskite solar cells. *Science* **2024**, *383* (6688), 1236-1240. DOI: 10.1126/science.adj9602.

(112) Al-Ashouri, A.; Köhnen, E.; Li, B.; Magomedov, A.; Hempel, H.; Caprioglio, P.; Márquez, J. A.; Morales Vilches, A. B.; Kasparavicius, E.; Smith, J. A.; et al. Monolithic perovskite/silicon tandem solar cell with >29% efficiency by enhanced hole extraction. *Science* **2020**, *370* (6522), 1300-1309. DOI: 10.1126/science.abd4016.

(113) Li, L.; Wang, Y.; Wang, X.; Lin, R.; Luo, X.; Liu, Z.; Zhou, K.; Xiong, S.; Bao, Q.; Chen, G.; et al. Flexible all-perovskite tandem solar cells approaching 25% efficiency with molecule-bridged hole-selective contact. *Nature Energy* **2022**, *7* (8), 708-717. DOI: 10.1038/s41560-022-01045-2.

(114) Cassella, E. J.; Spooner, E. L. K.; Thornber, T.; O'Kane, M. E.; Catley, T. E.; Bishop, J. E.; Smith, J. A.; Game, O. S.; Lidzey, D. G. Gas-Assisted Spray Coating of Perovskite Solar Cells Incorporating Sprayed Self-Assembled Monolayers. *Advanced Science* **2022**, *9* (14), 2104848. DOI: https://doi.org/10.1002/advs.202104848.

(115) Liu, M.; Bi, L.; Jiang, W.; Zeng, Z.; Tsang, S.-W.; Lin, F. R.; Jen, A. K.-Y. Compact Hole-Selective Self-Assembled Monolayers Enabled by Disassembling Micelles in Solution for Efficient Perovskite Solar Cells. *Advanced Materials* **2023**, *35* (46), 2304415. DOI: https://doi.org/10.1002/adma.202304415.

(116) Farag, A.; Feeney, T.; Hossain, I. M.; Schackmar, F.; Fassl, P.; Küster, K.; Bäuerle, R.; Ruiz-Preciado, M. A.; Hentschel, M.; Ritzer, D. B.; et al. Evaporated Self-Assembled Monolayer Hole Transport Layers: Lossless Interfaces in p-i-n Perovskite Solar Cells. *Advanced Energy Materials* **2023**, *13* (8), 2203982. DOI: https://doi.org/10.1002/aenm.202203982.

(117) Trinh, X.-L.; Nguyen, V.-M.; Nguyen, H.-C.; Phan, T.-L.; Kim, H.-C. Temperature-assisted crystallization and morphology for $CH_3NH_3PbI_3$ perovskite solar cells using laser-induced heat treatment. *Organic Electronics* **2024**, *132*, 107099. DOI: https://doi.org/10.1016/j.orgel.2024.107099.

(118) Mahmud, M. A.; Zheng, J.; Chang, J.-F.; Wang, G.; Liao, C.; Rahman, M. H.; Tarique, W. B.; Tang, S.; Bing, J.; Bailey, C. G.; et al. Halogenated Polycyclic Aromatic Hydrocarbon for Hole Selective Layer/Perovskite Interface Modification and Passivation for Efficient Perovskite-Organic Tandem Solar Cells with Record Fill Factor. *Advanced Energy Materials* **2024**, *14* (45), 2400691. DOI: https://doi.org/10.1002/aenm.202400691.

(119) Chen, M.; Li, Y.; Zeng, Z.; Liu, M.; Du, T.; Huang, X.; Bi, L.; Wang, J.; Jiang, W.; An, Y. Regulating the crystallization of mixed-halide perovskites by cation alloying for perovskite–organic tandem solar cells. *Energy & Environmental Science* **2024**, *17* (24), 9580-9589. DOI: https://doi.org/10.1039/D4EE03045A.

(120) Lin, R.; Xiao, K.; Qin, Z.; Han, Q.; Zhang, C.; Wei, M.; Saidaminov, M. I.; Gao, Y.; Xu, J.; Xiao, M.; et al. Monolithic all-perovskite tandem solar cells with 24.8% efficiency

exploiting comproportionation to suppress Sn(ii) oxidation in precursor ink. *Nature Energy* **2019**, *4* (10), 864-873. DOI: 10.1038/s41560-019-0466-3.

(121) Xu, F.; Zhang, M.; Li, Z.; Yang, X.; Zhu, R. Challenges and perspectives toward future wide-bandgap mixed-halide perovskite photovoltaics. *Advanced Energy Materials* **2023**, *13* (13), 2203911. DOI: https://doi.org/10.1002/aenm.202203911.

(122) Hu, X.; Shen, N.; Zhang, D.; Wu, Y.; Shang, R.; Wang, L.; Qin, C. Multi-Functional Spirobifluorene Phosphonate Based Exciplex Interface Enables V_{OC} Reaching 95% of Theoretical Limit for Perovskite Solar Cells. *Advanced Materials* **2024**, 2313099. DOI: https://doi.org/10.1002/adma.202313099.

(123) Muscarella, L. A.; Ehrler, B. The influence of strain on phase stability in mixed-halide perovskites. *Joule* **2022**, *6* (9), 2016-2031. DOI: 10.1016/j.joule.2022.07.005.

(124) Fang, Z.; Nie, T.; Liu, S.; Ding, J. Overcoming Phase Segregation in Wide-Bandgap Perovskites: from Progress to Perspective. *Advanced Functional Materials* **2024**, 34 (42), 2404402. DOI: https://doi.org/10.1002/adfm.202404402.

(125) An, Y.; Zhang, N.; Zeng, Z.; Cai, Y.; Jiang, W.; Qi, F.; Ke, L.; Lin, F. R.; Tsang, S.-W.; Shi, T.; et al. Optimizing Crystallization in Wide-Bandgap Mixed Halide Perovskites for High-Efficiency Solar Cells. *Advanced Materials* **2024**, *36* (17), 2306568. DOI: https://doi.org/10.1002/adma.202306568.

Chapter 2 CO_2 Laser-assisted Ambient Crystallization of $FAPbI_3$ Perovskite for Efficient Solar Cells

2.1 Introduction

Based on the advantages and progress made in laser annealing as discussed in 1.3, this chapter develops the CO_2 laser process for the first time for perovskite film crystallisation in ambient. This is because CO_2 laser is a very effective localised heat source and its longer wavelength (9.3 - 10.6 μm) meaning low photon energy (~0.12 eV) is anticipated to be compatible with perovskites but has not been used for annealing perovskite prior to this thesis to the best of our knowledge. The device structure used is of glass/ITO/(2-(3,6-Dimethoxy-9H-carbazol-9-yl)ethyl)phosphonic acid (MeO-2PACz)/$FAPbI_3$/C_{60}/Bathocuproine (BCP)/Cu.

2.2 Experimental methods

Materials

Unless stated otherwise, all materials and solvents used in this chapter were purchased from Sigma Aldrich. Formamidinium iodide (FAI) was from GreatCell Solar Materials. [2-(3,6-Dimethoxy-9H-carbazol-9-yl)ethyl]phosphonic Acid (MeO-2PACz) and lead iodide (PbI_2) were purchased from TCI. Pre-patterned ITO glasses with a sheet resistance of 8 Ω/sq were bought from Wuhan Jinge Solar Energy Technology Co. Ltd.

Device fabrication

Pre-patterned ITO glass substrates were rinsed sequentially in ultrasonic bath with deionized (DI) water-diluted HellmanexTM III solution, DI water, acetone and 2-propanol for 20, 5, 20, and 15 minutes, respectively. The rinsed substrates were dry by a nitrogen gun, which were then treated by ultra-violet-ozone (UVO) for 15 minutes.

Hole transport layer solution was prepared by dissolving MeO-2PACz into methanol, with a concentration of 0.5 mg/mL. The MeO-2PACz solution was deposited onto the ITO substrates by spin coating, at a spin rate of 4000 rpm for 16s. Thermal annealing was applied to the as-

deposited films upon 85 °C for 5 minutes.

$FAPbI_3$ solution was prepared by mixing FAI (258 mg), PbI_2 (692 mg) with DMF (900 μL):NMP (100 μL) binary solvent. The corresponding concentration was 1.5 M. $FAPbI_3$ precursor solution was stirred at room temperature for 30 min before use. 80 μL of $FAPbI_3$ precursor solution was spin-coated onto the MeO-2PACz layer with an acceleration of rate of 400 rpm/s to a spin rate of 4000 rpm for 50s. 15s into the spin coating, N_2 gas quenching (at a pressure of ~100 psi) was applied. The deposited $FAPbI_3$ precursor films were then transferred out of glovebox for ambient annealing.

For thermal annealing, the precursor films were heated on a hot plate at 150 ºC, for 20 minutes in ambient.

For laser annealing, the precursor films were illuminated by a 50 W CO_2 laser (Universal Laser VLS 3.60) in ambient (room temperature of 20 °C and uncontrolled humidity) (**Figure 2.1**). The collimated laser beam with an emission wavelength of 10.6 μm is reflected by a mirror and then focused by a Zinc Selenide (ZnSe) lens, creating a focused beam of ~127 μm in diameter. To obtain a larger spot size ~1 mm in diameter on the substrate for processing, the beam was positively defocussed with a defocussing length of 12.5 mm (Chapter 2) or 15.00mm (Chapters 4 and 5). The defocused laser beam scans across $FAPbI_3$ film surface by synchronizing the laser head motion in x- and y-direction at a speed of 254 mm/s, and a pulse per inch (PPI) of 500. This corresponds to a spacing of 50 μm between each pulse in the X-direction and a displacement of 100 μm in the Y-direction to avoid any edge effects (**Figure 2.2**). The laser power ratio varied between 22% and 36% for process optimization. For the very initial laser power selection, the lower possible power, i.e., 5% of the maximum power setting was used to scan the perovskite film of 2 cm^2 to qualitatively gauge the onset of crystallization (characterized by visual darkening of the perovskite film). Power was increased in increments of 2% until film darkening could be observed and crystallisation was confirmed via X-ray diffraction (XRD) measurement. This sets the lower bound for laser power optimization. The upper bound of laser power optimization was when film damage was observed. This process of searching for laser power optimisation is repeated when new perovskite material systems were used.

The laser power densities in kW/cm^2 quoted in this thesis are estimated from laser power ratios of the nominal "50 W" used and the beam size. The pulse repetition rate that will be used for COMPSOL simulation is determined from laser scan speed and the pulse per inch. Laser pulse energy density is determined from the laser power density and the pulse repetition rate.

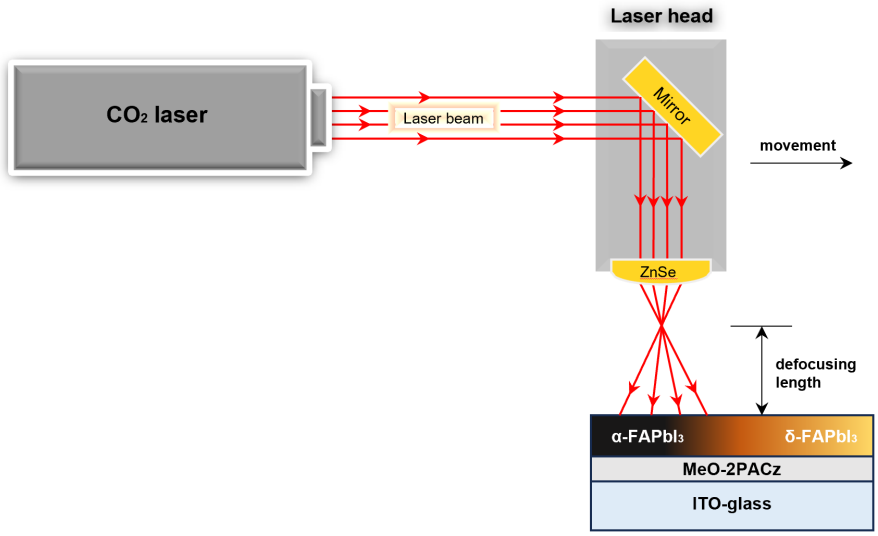

Figure 2.1 Schematic for CO_2 laser annealing of $FAPbI_3$ film.

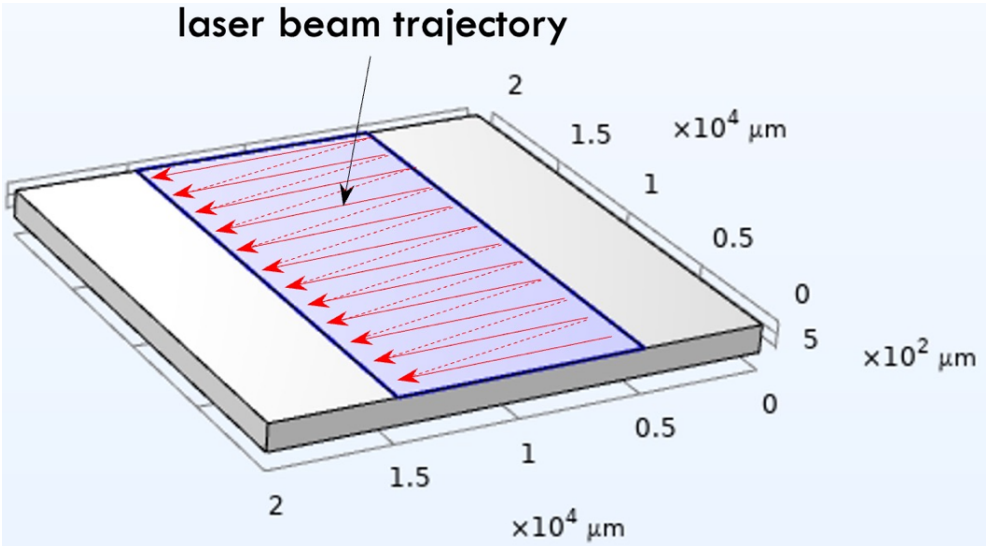

Figure 2.2. Schematic illustration of laser scanning, represented by solid lines when the laser is on and dashed lines when the laser is off.

After ambient annealing, C_{60} (20 nm), BCP (6 nm) and Cu (100 nm) were then deposited sequentially onto $FAPbI_3$ perovskite surface using a thermal evaporator.

Device and film characterizations

Current density-voltage (*J-V*) measurements were carried out using a solar simulator (Class AAA solar simulator, Newport Technologies, Inc.) under 1 sun-condition (AM 1.5G, 1000 W/m^2, 25 °C). A certified Si reference cell was used for 1 sun light-intensity calibration. The

scanned voltage range was -0.1 – 1.3 V for all solar cells, with a reverse scan rate of 400 mV/s. The aperture area of the cell was 0.0706 cm^2.

External quantum efficiency (EQE) measurements were conducted using the QuantX-300 Spectral Response (Newport Inc.) system with monochromatic light from a xenon arc lamp. The system was calibrated using a certified silicon reference cell for 300-1200 nm wavelength regions.

Light intensity-dependent V_{OC} measurements were performed using the same *J-V* measurement setup, with neutral density (ND) filters for light intensity modulation. The ideality factor, n_{id}, was derived from Equation 2.1:

$$V_{OC} = \frac{n_{id} k_B T}{e} \ln\left(\frac{J_{SC}}{J_0}\right) \quad (2.1)$$

Where k_B is the Boltzmann constant, T is the temperature, q is the elementary charge, and J_0 is the saturation current density under reverse bias, V_{OC} is the open-circuit voltage under various light intensities, and J_{SC} the light illumination intensity.

Temperature dependent V_{OC} was measured with Keysight 2636B source meter under 530 nm LED illumination (equivalent to 1-sun) in a customized probe station with true kelvin probe for each manipulator (KeyFactor Inc) and liquid-N_2 cooler. The temperature of the probe station was adjusted using a Lakeshore 336 temperature controller. For determining the activation energy of recombination E_a, J_0 the following Equation was used

$$J_0 = J_{00} \exp\left(-\frac{E_a}{n_{id} k_B T}\right) \quad (2.2)$$

where J_{00} is the pre-exponential factor and E_a is the activation energy of recombination current in the diode. From Equations 2.1 and 2.2, Equation 2.3 is derived.

$$eV_{OC} = E_a - n_{ID} k_B T ln \frac{I_0}{I} \quad (2.3)$$

Scanning electron microscopy (SEM) was conducted using a field emission SEM (NanoSEM 230). Grain sizes were measured with ImageJ.

Atomic force microscopy (AFM) was conducted using a Bruker dimension icon (USA). Samples were scanned at rate of 0.9 Hz and a resolution of 512 samples per line. The AFM results were processed with NanoScope Analysis software.

X-ray diffraction (XRD) measurements were conducted using a PANalytical X'Pert X-ray diffractometer operated at 30 kV, 10 mA at 2θ (Cu Kα) 10-50° with an interval of 0.01°.

Steady-state and time-resolved photoluminescence spectra were obtained using the

Spectrofluorometer FS5 provided by Edinburgh instruments. The effective lifetimes, τ_{eff}, is calculated by the Equation 2.4:

$$\tau_{eff} = \frac{a_1\tau_1{}^2+a_2\tau_2{}^2}{a_1\tau_1+a_2\tau_2} \quad (2.4)$$

Where a_i is the fluorescence intensity contribution of each lifetime component τ_i.

X-ray photoelectron spectra (XPS) were measured using a Thermo Fisher Scientific K-Alpha X-ray Photoelectron Spectrometer System with 72 W monochromatic Al K-Alpha (1486.68 eV) X-ray source. The spectra were normalized individually and calibrated by C-C/C=C binding energy of 284.8 eV.

Fully fabricated solar devices were used for current *J-V*, EQE, light-intensity-dependent V_{OC}, and temperature-dependent-V_{OC} measurements.
Test structures of $FAPbI_3$/MeO-2PACz/ITO/glass were used for SEM, AFM, XRD.

Steady-state power output measurements were conducted on un-encapsulated devices in ambient without temperature and humidity control by holding the device at a fixed voltage (which was near maximum power point ~V_{MPP} obtained from an initial measurement) followed by the switching on of the one-sun illumination which was continued for a period. The steady-state power conversion efficiency was calculated as the product of steady-state current density (*J*) and voltage.

Ambient stability testing was conducted on un-encapsulated devices which were measured at regular intervals ex-situ while not in storage. Storage was in the dark at 25±5°C and relatively humidity of 25%. Measurement was conducted in ambient without temperature and humidity control.

2.3 Results and discussions

Figure 2.3 compares the quality of the $FAPbI_3$ films on MeO-2PACz/ITO glass substrate after ambient thermal anneal (ATA) by hot-plate, as a control, and ambient laser anneal (ALA) (**Figure 2.1**) at different laser power density. Details for film fabrication and annealing conditions can be found in the above Experimental Details. It is important to note that processing time for ALA film is significantly shorter (60 seconds) despite the need for scanning while the processing time for ATA film is 10 to 20 minutes. In addition, the substrate

temperature during ALA process is much lower than that during the ATA process (**Table 2.1**) minimising thermal effect to layers other than the perovskite absorber in the solar cells.

Figure 2.3a-f show the morphologies of the perovskite films by top-view scanning electron microscopy (SEM) after ATA and ALA processes. While films are reasonably compact, ATA film and the ALA film with the higher laser power densities have larger spread of grain size distribution compared to the ALA films with lower laser power densities (**Figure 2.4g**).

Table 2.1 Measured substrate temperatures during ALA. They do not reflect the actual temperatures experienced locally by the perovskite films but nevertheless show a trend in temperature with increasing power densities.

ALA Power Density (kW/cm^2)	Substrate Temperature (°C)		Change in temperature (°C)
	Before ALA	After ALA	
1.4	23	24	1
1.5	20	26	6
1.7	22	28	6
1.9	21	35	14
2.3	20	38	18

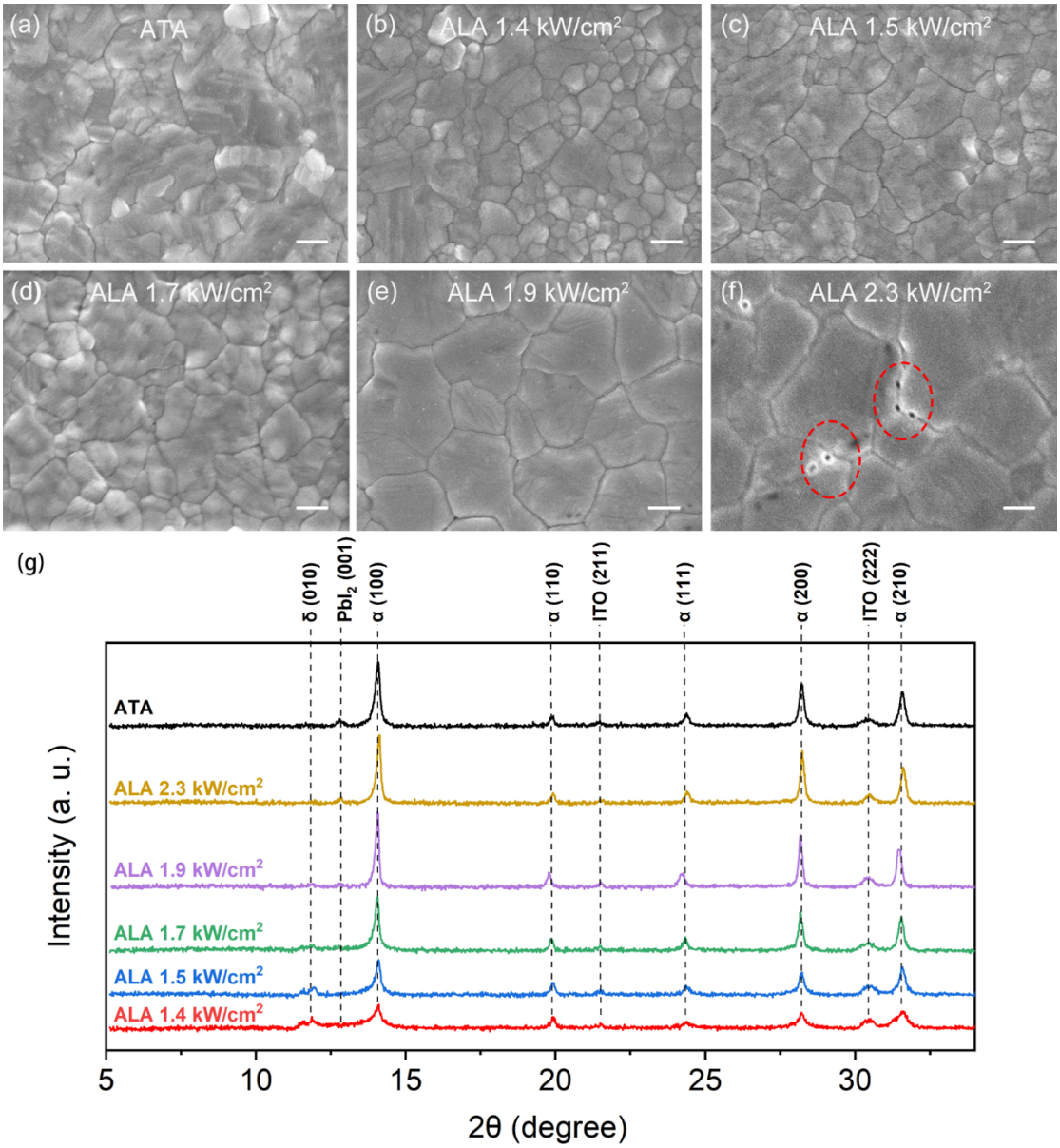

Figure 2.3 Top-view SEM images of (a) an ATA film and (b-f) ALA films processed at various laser power densities. Scale bar = 300 nm. (g) XRD patterns for ATA and ALA films.

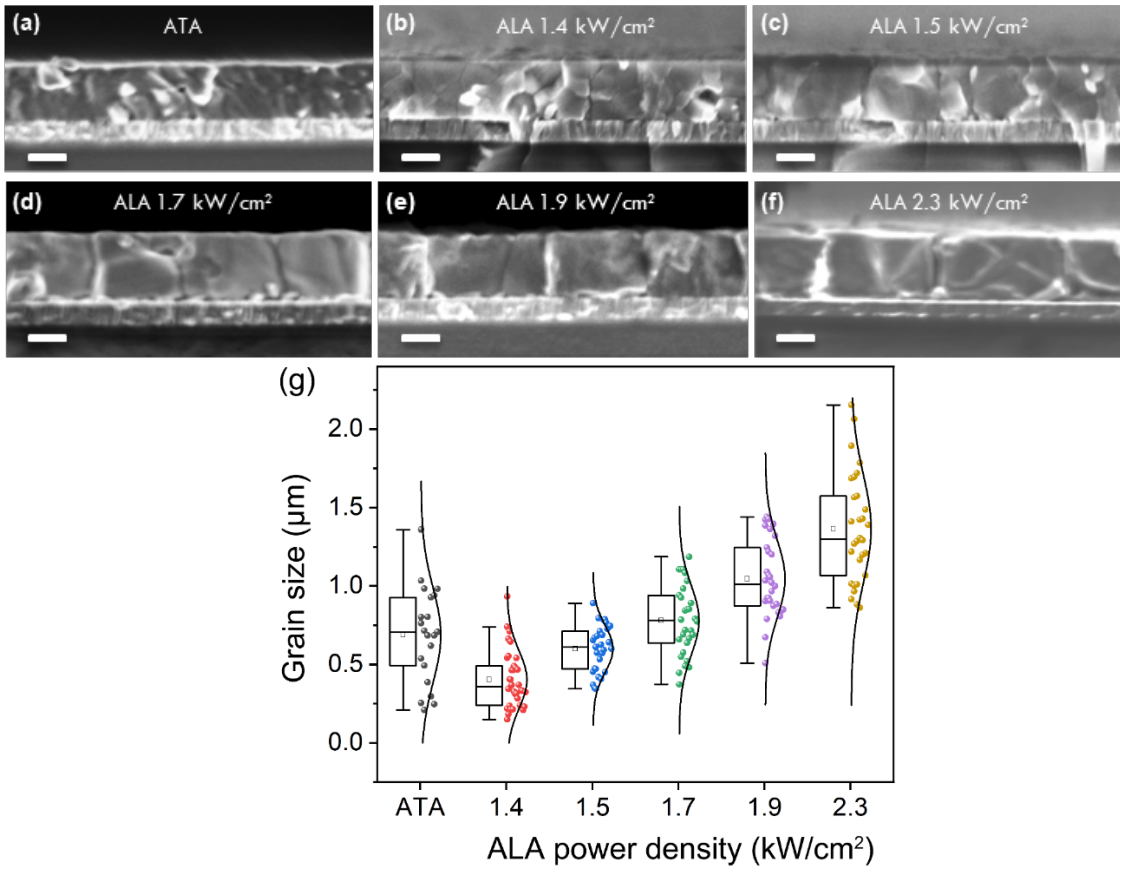

Annealing method	Average grain size (μm)
ATA	0.69±0.30
ALA 1.4 kW/cm²	0.40±0.18
ALA 1.5 kW/cm²	0.62±0.20
ALA 1.7 kW/cm²	0.78±0.22
ALA 1.9 kW/cm²	1.05±0.25
ALA 2.3 kW/cm²	1.36±0.35

Figure 2.4 Scanning electron microscopy (SEM) cross-section images of the (a) ATA and ALA films annealed by laser at power intensity of (b) 1.4, (c) 1.5, (d) 1.7, (e) 1.9 and (f) 2.3 kW/cm^2. Scale bar = 300 nm. (g) The corresponding grain sizes distributions and the average grain sizes are listed in inset table.

ALA film grains also grow larger with laser power density from < 0.5 μm (on average) at 1.4 kW/cm^2 to ≳1 μm at ≳ 1.9 kW/cm^2 **(Figure 2.3)**. However, cracks at the grain boundaries started to emerge at 2.3 kW/cm^2 (**Figure 2.3f**) and worsen at higher laser annealing power (e.g., 2.5 kW/cm^2) **(Figure 2.5)**. The correlation between grain size and laser power density[1] is likely to be due to higher heat generated by the laser (**Table 2.1**) absorbed locally by the film. The higher the power density, the more rapid is the solvent evaporation inducing nucleation and crystallization which is localised but not necessarily restricted as grain growth can extend to regions that are not yet irradiated.[2,3] ATA film on the other hand is heated by the hot plate to

induce nucleation and crystallisation across the full area simultaneously. Grain growth eventually self-limits as neighbouring grains impinge on each other. This explains the smaller grains observed in the ATA film. As laser power density increases, film thickness remains at ~500 nm, demonstrating no evident material ablation from high intensity laser processing. Evident from results of atomic force microscopy (AFM) (**Figure 2.6a**), advantage of ALA film disappears at laser power density of 2.3 kW/cm^2 where surface roughness doubled (**Figure 2.6f**) as cracks emerged from the grain boundaries. This is likely to be due to the excessive heat generated by the laser scanning causing outgassing of volatile components from the perovskite film[16], leading to film decomposition starting at the grain boundaries.

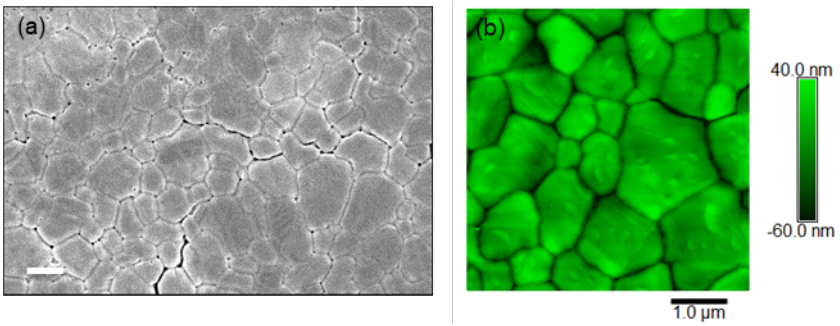

Figure 2.5 (a) SEM and (b) atomic force microscopy (AFM) images of $FAPbI_3$ film after ALA process at 2.5 kW/cm^2 showing the worsening of crack appearance. Scale bar = 1 µm.

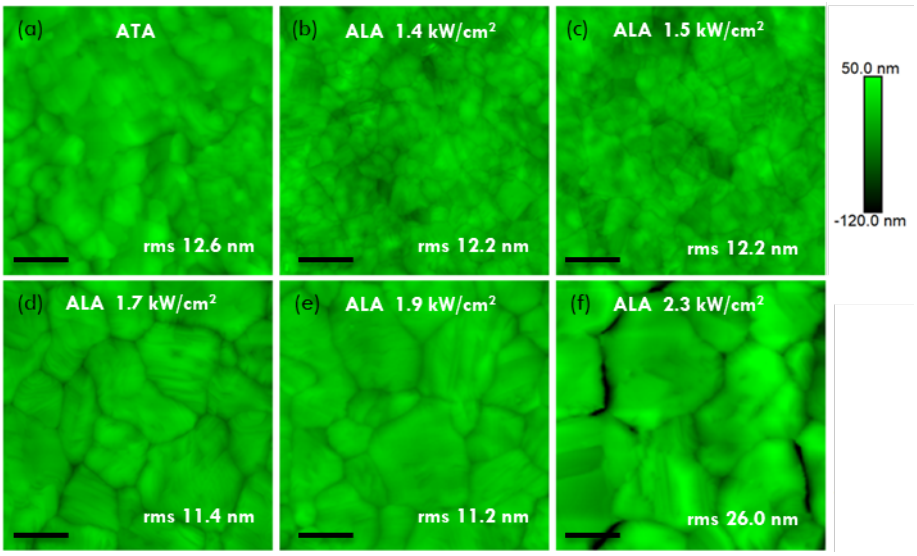

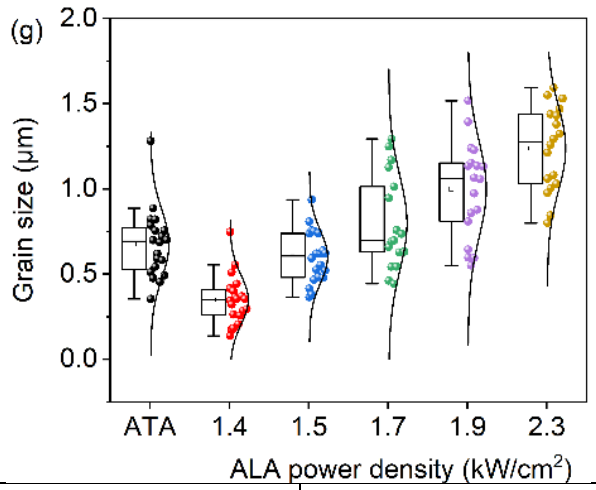

Annealing method	Average grain size (μm)
ATA	0.68±0.20
ALA 1.4 kW/cm²	0.35±0.14
ALA 1.5 kW/cm²	0.60±0.15
ALA 1.7 kW/cm²	0.80±0.28
ALA 1.9 kW/cm²	1.00±0.28
ALA 2.3 kW/cm²	1.24±0.25

Figure 2.6 AFM images of the (a) ATA and ALA $FAPbI_3$ films annealed by laser at power intensity of (b) 1.4, (c) 1.5, (d) 1.7, (e) 1.9 and (f) 2.3 kW/cm^2. Scale bar = 300 nm. The corresponding grain sizes distributions and the average grain sizes are listed in inset table correlating with results in **Figure 2.3**.

In terms of crystallinity, X-ray diffraction (XRD) measurements were performed (**Figure 2.3g**). **Figure 2.7a to e** show the full-width at half-maxima (FWHM) and intensities of the 13.9°, 19.8°, 24.4°, 28.1°, and 31.4° peaks, which are indexed to the (100), (110), (111), (200), and (210) diffractions, respectively, of the desirable photo-active black α-$FAPbI_3$ phase as a function of annealing conditions. The FWHM and intensities of the undesirable less-photo-

active yellow δ-$FAPbI_3$ phase (11.9°) are also plotted as a function of annealing conditions in **Figure 2.8**.

While the ATA film produced narrow and strong α-$FAPbI_3$ (100), (111), (200), and (210) peaks (**Figure 2.7**), a small peak at around 12.6° can be observed in the ATA film (black curve in **Figure 2.3g**) suggesting the presence of unreacted PbI_2. δ-$FAPbI_3$ phase is prevalent in the lower-laser-power-processed ALA film (**Figure 2.3**) but gradually disappears as laser power intensity increases while α-$FAPbI_3$ phase gradually dominates (**Figure 2.7)**, showing strong preference to (100), (200), and (210), compared to (110) and (111).

However, when laser power density is at 2.3 kW/cm^2, precipitation of PbI_2 (emergence of its corresponding peak in the yellow curve in **Figure 2.3g**) can be seen due to the outgassing of volatile organic components leading to decomposition of the film under high laser power as discussed above.

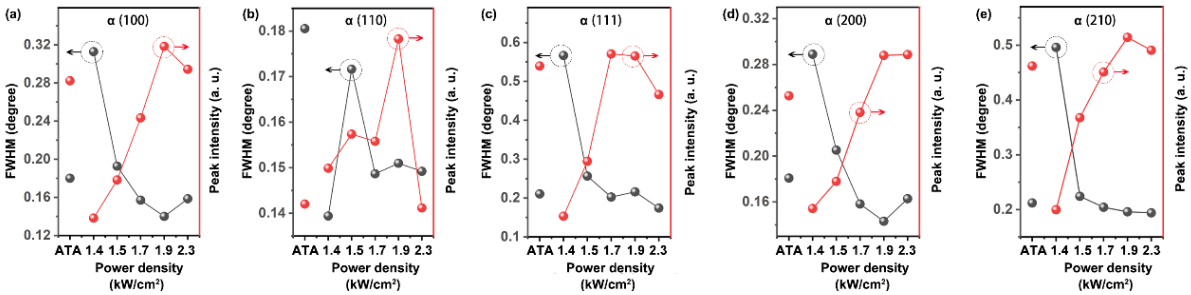

Figure 2.7 Full-width at half-maxima (FWHM) (black) and intensities (red) of the (a) 13.9°, (b) 19.8°, (c) 24.4°, (d) 28.1°, and (e) 31.4° peaks, which are indexed to the (100), (110), (111), (200), and (210) diffractions, respectively, of the desirable photo-active black α-$FAPbI_3$ phase as a function of annealing conditions.

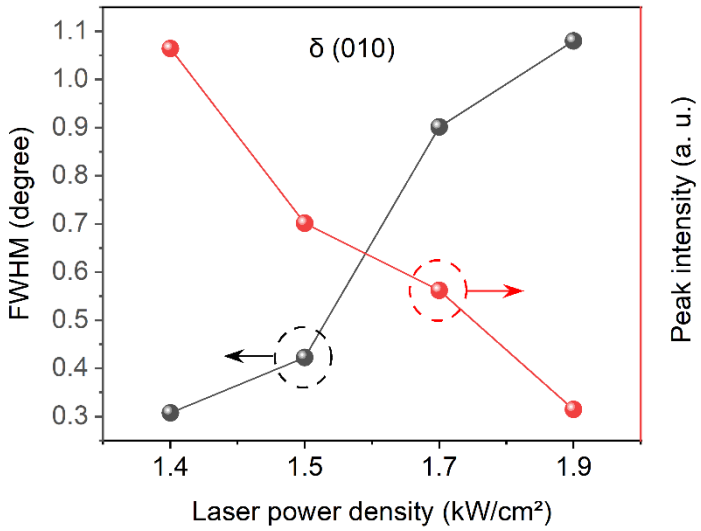

Figure 2.8 Full-width at half-maxima (FWHM) (black) and intensities (red) of the 11.9° peak, which is indexed to the (010) diffraction, of the photo-inactive yellow δ-$FAPbI_3$ phase as a function of laser annealing conditions. Noted that no evident δ-phase peaks observed from ATA film and high-power-(2.3 kW/cm^2)-processed film.

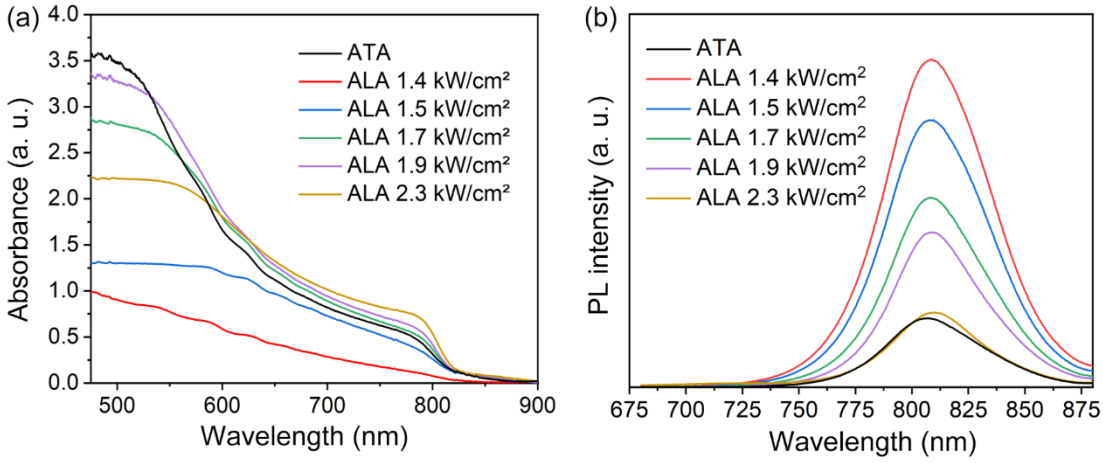

Figure 2.9 (a) Absorbance spectra and (b) steady-state photoluminescence spectra of representative ATA and ALA films at different laser power densities.

Figure 2.9 shows the absorption and steady-state photoluminescence (PL) of representative $FAPbI_3$ films treated by ATA and ALA at various power densities. Steady-state photoluminescence of multiple $FAPbI_3$ films were also measured and the trends in PL peak position and intensity are plotted in **Figure 2.10**.

Photo-absorption is high in ATA film corresponding to strong prevalence of α-$FAPbI_3$ phase as observed in XRD results (**Figure 2.7**).

Photo-absorption is low in ALA film annealed by low laser power but increases with laser

power densities as α-$FAPbI_3$ phase dominates. It was confirmed that variations in the absorption observed were not due to any changes in the optical properties of the ITO substrates as shown in **Figure 2.11**.

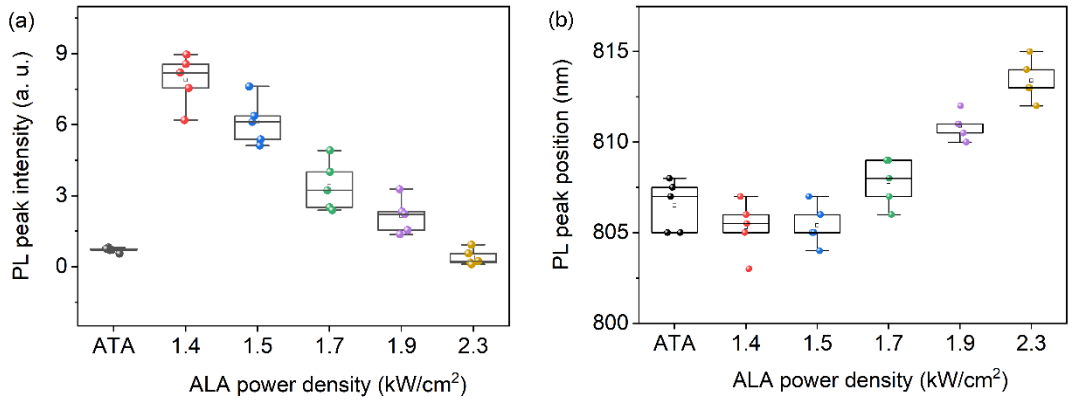

Figure 2.10 Distributions of steady-state PL (a) intensity and (b) peak position measured from multiple ATA and ALA $FAPbI_3$ films annealed by laser at various power intensities.

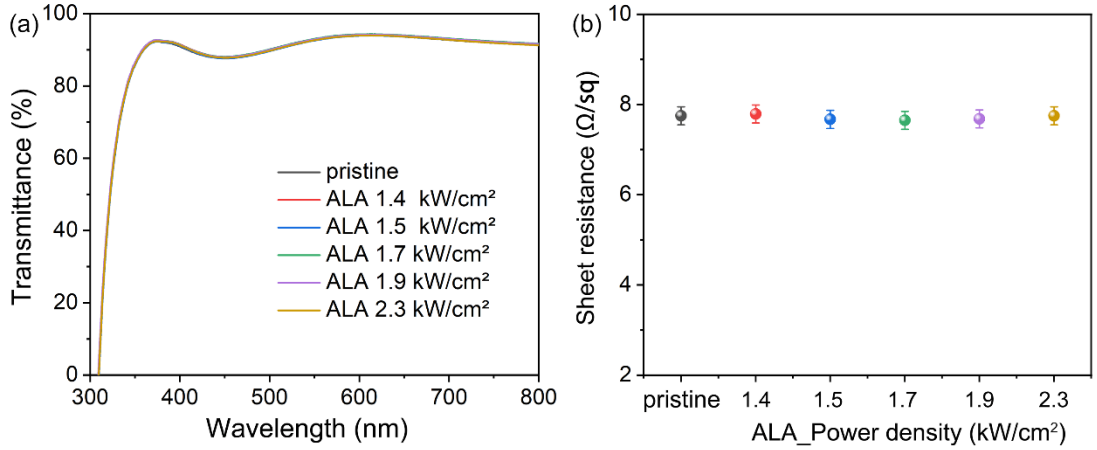

Figure 2.11 (a) Transmittance spectra and (b) sheet resistance of ITO substrates only undergoing the same CO_2 laser treatment as perovskite test structures. No damage or adverse effects can be observed.

Photoluminescence (PL) intensities (**Figure 2.10a**) of the ALA films, on the hand, reduces with increasing laser power density. This is likely to be due to the driving out of the volatile organic components from the film with increasing laser power as discussed above increasing the PbI_2 to FAI ratio (**Figure 2.12**). The eventual precipitation of PbI_2 in the 2.3 kW/cm^2 ALA film, much like the un-reacted PbI_2 in the ATA film, act as defects that have an adverse effect on their photoluminescence responses (black and yellow data points in **Figure 2.10a**).

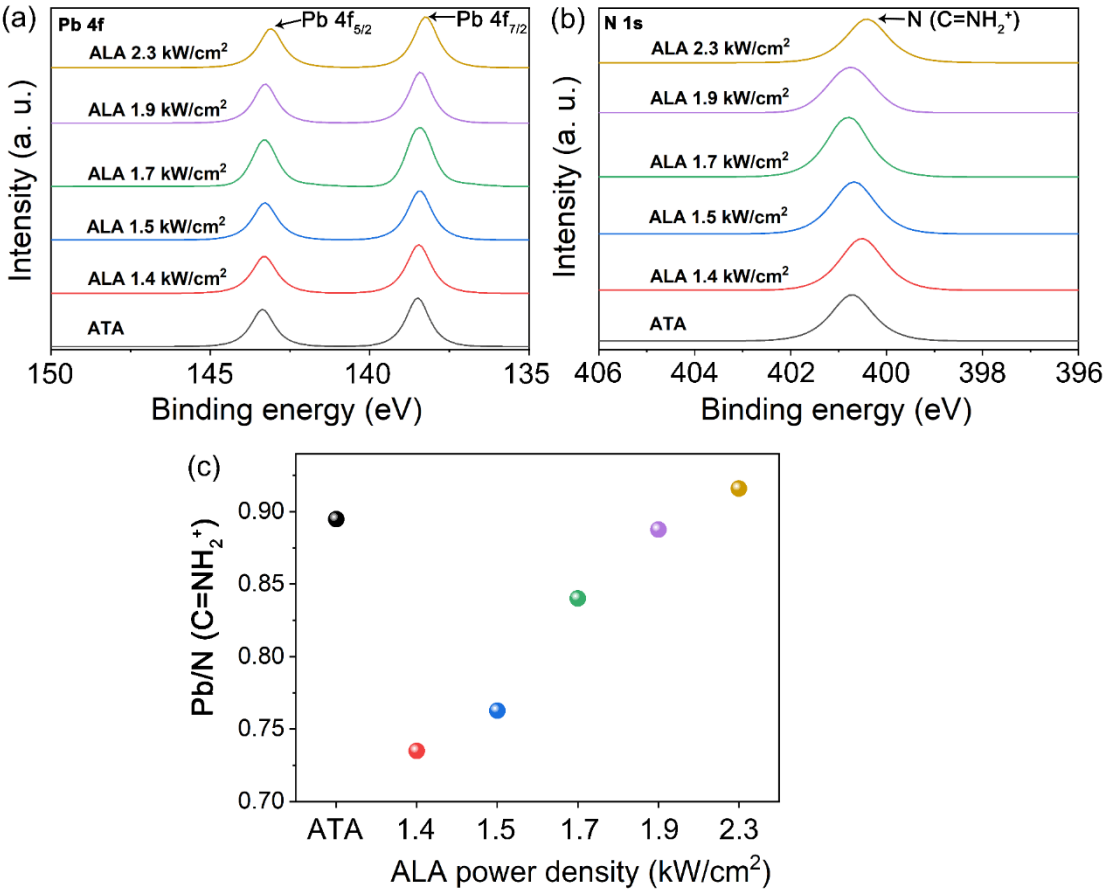

Conditions	Pb 4f/%	N(C=NH_2^+)/%
ATA	2.38	2.66
ALA 1.4 kW/cm^2	2.19	2.98
ALA 1.5 kW/cm^2	2.25	2.95
ALA 1.7 kW/cm^2	2.26	2.69
ALA 1.9 kW/cm^2	2.45	2.76
ALA 2.3 kW/cm^2	2.29	2.50

Figure 2.12 The deconvoluted high-resolution X-ray photoelectron spectroscopy (XPS) spectra of (a) Pb 4f, (b) N 1s for ATA and ALA films processed at 1.4; 1.5; 1.7; 1.9 and 2.3 kW/cm^2. (c) Calculated averaged relative atomic ratio of Pb/N(C=NH_2^+) from XPS at each condition, approximating PbI_2/FAI. Accompanying table shows atomic percentages of Pb and N(C=NH_2^+).

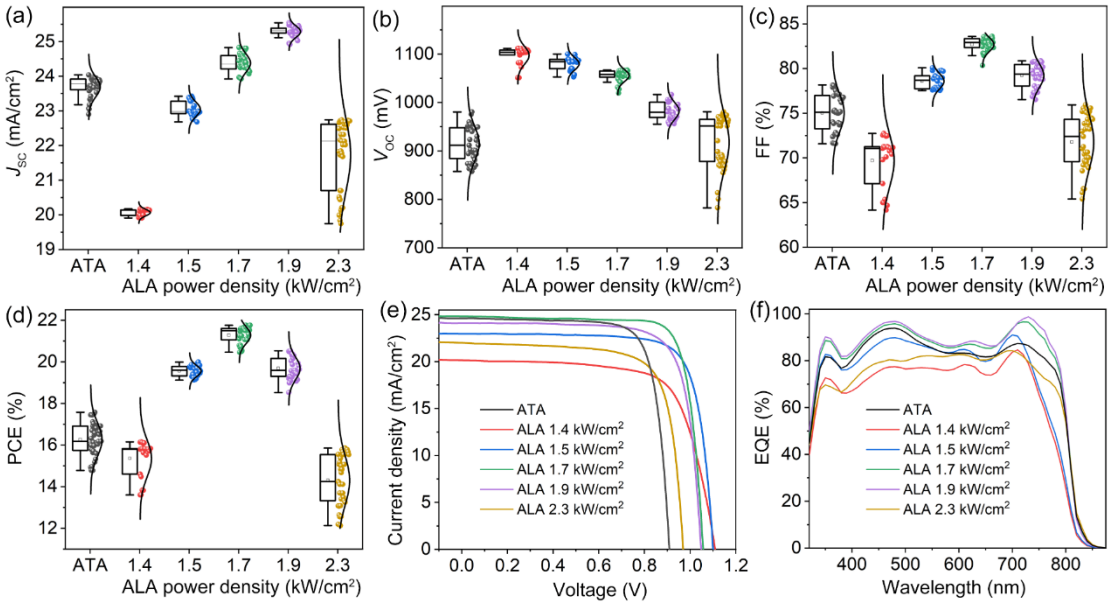

Figure 2.13 Distributions of (a) short circuit current density (J_{SC}), (b) open circuit voltage V_{OC}, (c) fill factor (FF), (d) power conversion efficiency (PCE) of glass/ITO/MeO-2PACz/$FAPbI_3$/C_{60}/BCP/Cu cells by ambient thermal annealing (ALA) and ambient (relativity humidity of 30 to 40%) laser annealing (ALA) at various power densities. More than 20 devices were measured in each batch for (a) to (d). (e) Current density-voltage (*J-V*) and (f) external quantum efficiency (EQE) curves of champion devices in each category.

Table 2.2 Photovoltaic performance of champion devices by ambient (relativity humidity of 30 to 40%) thermal annealing (ATA) and ambient laser annealing (ALA).

Annealing method	Laser power density (kW/cm^{-2})	PCE (%)	FF (%)	V_{OC} (mV)	J_{SC} (mA cm^{-2})	J_{EQE} (mA cm^{-2})
ATA	N/A	17.6	75	980	23.9	23.5
ALA	1.4	15.8	71	1104	20.1	20.0
	1.5	20.0	80	1089	22.9	22.1
	1.7	21.8	83	1058	24.8	24.7
	1.9	20.5	81	1007	25.3	25.0
	2.3	15.8	74	952	22.3	22.0

Given the trends observed in perovskite material properties after laser annealing, full solar devices were fabricated based on an inverted structure of glass/ITO/MeO-2PACz/$FAPbI_3$/C_{60}/BCP/Cu, using the same ATA and ALA conditions. The distributions of the device parameters are given in **Figure 2.13** together with the *J-V* and EQE curves of the champion devices whose parameters are also listed in **Table 2.2**.

In terms of the effect on V_{OC}, increasing laser power processing is harmful (**Figure 2.13b**) due to the outgassing of organic component leading to eventual precipitation of PbI_2 as $FAPbI_3$ started to decompose as discussed above. The trend of V_{OC} correlates with that of photoluminescence response of the perovskite film (**Figure 2.9b**), also measured under open

circuit condition.

The presence of PbI_2 related defects in the ATA film and ALA films processed by high laser power is confirmed by their light intensity-dependent V_{OC} measurements (**Figure 2.14a**). The films produced higher values of ideality factor due to trap-assisted Shockley–Read–Hall recombination.[5]

Temperature-dependent V_{OC} measurements were also conducted for the solar cells (**Figure 2.14b**) to determine activation-energy (E_a) of recombination current (**Figure 2.14c**). E_a decreases with laser power density indicating the recombination mechanism become more surface dominated due to the increasing the presence of PbI_2 related defects.[6]

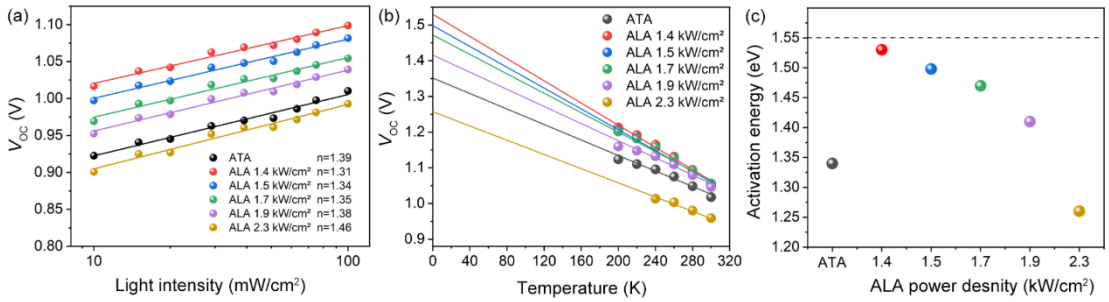

Figure 2.14 (a) The V_{OC} of ATA and ALA devices as a function of light intensity. (b) The temperature dependence of V_{OC}. (c) The trap activation energies upon ATA and ALA with varied power densities.

The opposing effects of increasing laser processing power therefore explains the trend in J_{SC} and fill factor (FF) observed.

The increasing dominance of photo-active α-$FAPbI_3$ phase improves photo-absorption (**Figure 2.9a**) thereby increasing J_{SC} (**Figure 2.13a**) until laser processing power is at 2.3 kW/cm^2. In perovskite films processed by high laser power (>1.7 kW/cm^2), there is an increasing presence of PbI_2 related defects (reducing carrier lifetime (**Figure 2.15)**). The opposing effects results in the trend observed in fill factor (**Figure 2.13c**) and J_{SC} observed. For the latter, even though photons were well absorbed in the 2.3 kW/cm^2 film (**Figure 2.9a**), a significant portion of photon-generated carriers were not collected resulting in low quantum efficiency (photon-electron-conversion) (**Figure 2.13f**) and therefore low J_{SC} (**Figure 2.13a**), low V_{OC} (**Figure 2.13b**) and ultimately low PCE (**Figure 2.13d**).

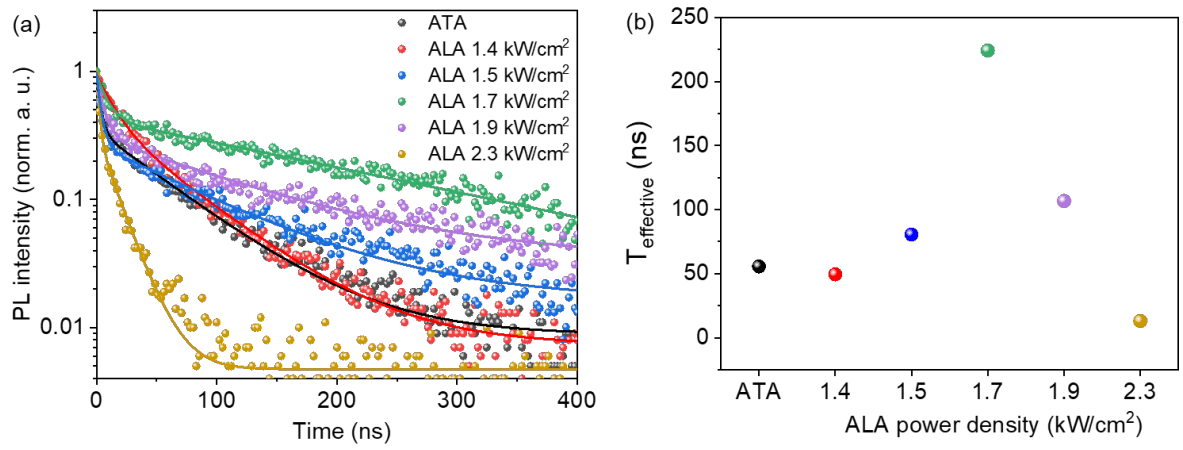

Figure 2.15 (a) Time-resolved PL and (b) corresponding carrier lifetimes of ATA and ALA $FAPbI_3$ films annealed by laser at various power intensities.

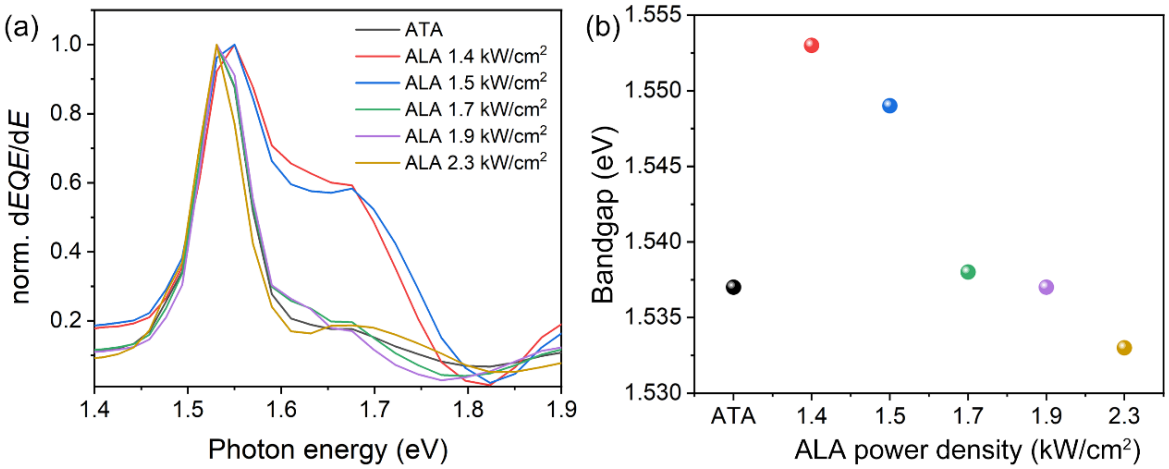

Figure 2.16 (a) Normalized d*EQE*/d*E* as a function of photon energy for determining (b) bandgap values as a function of annealing conditions.

The higher prevalence of yellow δ-$FAPbI_3$ phase in lower-laser-power-processed ALA film explains the larger bandgap observed in these films (**Figure 2.16**) possibly due to the presence of α-$FAPbI_3$/δ-$FAPbI_3$ junction that has a larger bandgap as reported by Ma *et al*. The excess PbI_2 in the ATA film and in the 2.3 kW/cm^2 laser processed films is the likely cause for the reduced bandgap observed in these films.

A balance is struck when the laser power density is at 1.7 kW/cm^2 producing best performance cells whereby the champion cell achieved an efficiency of 21.8%, with a J_{SC} of 24.8 mA/cm^2, a V_{OC} of 1057.9 mV and a high FF of 82.9% that are of higher values than the cells processed by thermal annealing. These are impressive values considering i) the annealing was conducted in ambient; ii) the perovskite precursor did not have additional additives for bulk passivation; iii) or additional layers for surface passivation. At the time of reporting, this was the highest

efficiency achieved by laser annealed perovskite solar cells (**Table 1.2b** in Chapter 1). Preliminary stability test results show that cell stability correlates with cell performance as a function of laser annealing power. Stability of the ALA cells improve with laser power (**Figure 2.17a**) and peaks at 1.7 kW/cm^2. 1.7 kW/cm^2 ALA cell is also more stable than an ALA cell (**Figure 2.17b**). An un-encapsulated 1.7 kW/cm^2 ALA cell retained 95% of initial efficiency after 1000 hours of storage in the dark in 25±5°C and relatively humidity of 25% while the ATA counterpart retained only 90% of initial efficiency under the same condition.

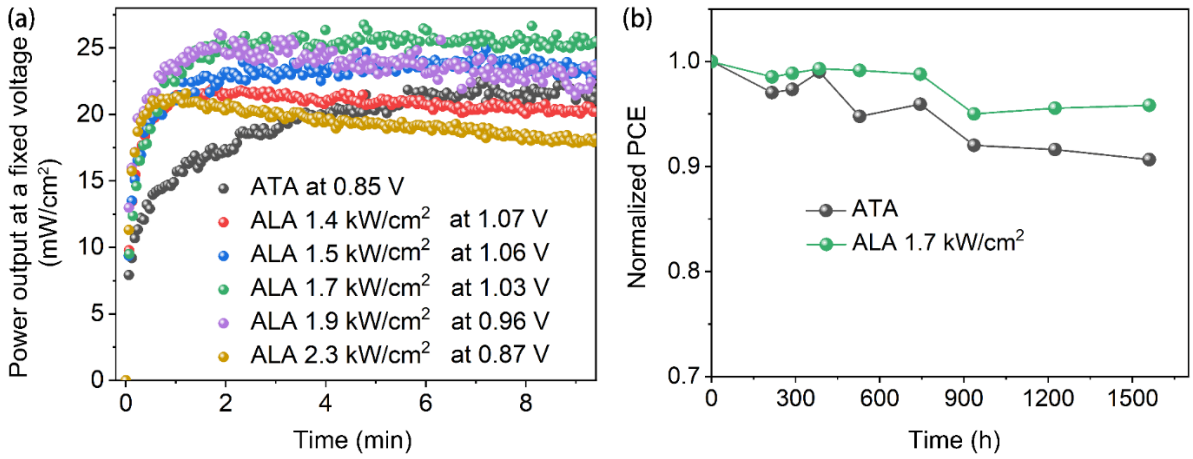

Figure 2.17 (a) Steady state power output at a fixed voltage near maximum power point of un-encapsulated ATA and ALA $FAPbI_3$ cells (annealed by laser at various power intensities). (b) Ambient stability testing (ex-situ measurement of cells when taken out of storage) of un-encapsulated ATA and ALA (1.7 kW/cm^2) $FAPbI_3$ cells.

2.4 Conclusion

In summary, the use of CO_2 laser annealing was successfully demonstrated for highly efficient $FAPbI_3$ p-i-n solar cells. While increasing laser power favours the formation of α-$FAPbI_3$ phase, the higher power also drives the volatile organic component in the perovskite film increasing the presence of PbI_2 related defects. Therefore, when the appropriate laser processing power (e.g., 1.7 kW/cm^2) was used, high power conversion efficiency (PCE) of 21.8% was achieved which was higher than that of the champion cell processed by thermal annealing. Given that the annealing was performed in ambient, the perovskite precursor did not have additional additives for bulk passivation and the perovskite film did not have additional layers for surface passivation, the performance achieved was impressive. At the time of reporting, the PCE achieved in this work was the highest for any laser annealed perovskite solar cells. It is

anticipated this work will inspire further future development of laser processing for perovskite solar cells.

2.5 References

(1) Jeon, T.; Jin, H. M.; Lee, S. H.; Lee, J. M.; Park, H. I.; Kim, M. K.; Lee, K. J.; Shin, B.; Kim, S. O. Laser Crystallization of Organic–Inorganic Hybrid Perovskite Solar Cells. *ACS Nano* **2016**, *10* (8), 7907-7914. DOI: 10.1021/acsnano.6b03815.

(2) You, P.; Li, G.; Tang, G.; Cao, J.; Yan, F. Ultrafast laser-annealing of perovskite films for efficient perovskite solar cells. *Energy & Environmental Science* **2020**, *13* (4), 1187-1196. DOI: 10.1039/C9EE02324K.

(3) Song, C.; Tong, L.; Liu, F.; Ye, L.; Cheng, G. J. Addressing the Reliability and Electron Transport Kinetics in Halide Perovskite Film via Pulsed Laser Engineering. *Advanced Functional Materials* **2020**, *30* (5), 1906781. DOI: https://doi.org/10.1002/adfm.201906781.

(4) Shi, L.; Bucknall, M. P.; Young, T. L.; Zhang, M.; Hu, L.; Bing, J.; Lee, D. S.; Kim, J.; Wu, T.; Takamure, N.; et al. Gas chromatography–mass spectrometry analyses of encapsulated stable perovskite solar cells. *Science* **2020**, *368* (6497), eaba2412. DOI: 10.1126/science.aba2412.

(5) Chen, H.; Chen, Y.; Zhang, T.; Liu, X.; Wang, X.; Zhao, Y. Advances to High-Performance Black-Phase $FAPbI_3$ Perovskite for Efficient and Stable Photovoltaics. *Small Structures* **2021**, *2* (5), 2000130. DOI: https://doi.org/10.1002/sstr.202000130.

(6) Tress, W.; Yavari, M.; Domanski, K.; Yadav, P.; Niesen, B.; Correa Baena, J. P.; Hagfeldt, A.; Graetzel, M. Interpretation and evolution of open-circuit voltage, recombination, ideality factor and subgap defect states during reversible light-soaking and irreversible degradation of perovskite solar cells. *Energy & Environmental Science* **2018**, *11* (1), 151-165. DOI: 10.1039/C7EE02415K.

Chapter 3 COMSOL Simulation of Temperature Profiles of Laser Annealed Perovskite and Hole Transport Layers

3.1 Introduction

As discussed in Chapter 1, a CO_2 laser was chosen in this thesis due to its low photon energy minimising damage to the perovskite film. While more details of the laser annealing conditions can be found in the next section, one important point to note is that the laser scan rate was set at 254 mm/s according to industry standard.[1-3] Therefore, the annealing duration was dramatically shorted to 1 minute per layer compared to 10 minutes by thermal over the same area. In fact, the dwell time for each laser spot beam is only 9.4 ms (**Table 3.1**) which is sufficient to facilitate high quality perovskite crystallisation which is a great advantage for industrialisation of this process facilitating high throughput, energy-efficiency while maintaining lower substrate and cell temperatures during processing.

To better ascertain temperature experienced by the substrate during annealing, rudimentary measurement was carried out and results were compared with those from a finite element simulation was performed using COMSOL Multiphysics software[4,5] for a three-dimensional (3D) time-dependent heat distribution model.[6,7] Such simulation provides a clear picture on global and local heat flow at different time scales which is very challenging to obtain in-situ during laser processing. At the time of reporting, this was the very first 3D model regarding laser annealing in perovskite solar cells.

3.2 Simulation methods

Table 3.1 summarises the laser processing parameters used for perovskite and and Me-4PACz layers experimentally and for temperature profiling simulation.

Table 3.1. Laser processing parameters used for perovskite and Me-4PACz layers experimentally and for temperature profiling simulation

	Perovskite	Me-4PACz
Laser power	16 W	17.5 W
Laser pulse energy density	0.28 J/cm^2	0.31 J/cm^2
Pulse repetition rate	5000 Hz	
Scanning speed	254 mm/s	
Dwell time	9.4 ms	
Pulse-to-pulse distance_x direction	50.8 μm	
Pulse-to-pulse distance_y direction	100 μm	
Time gap between two pulses	0.2 ms	

Temperature profiling simulation

The simulation of laser annealing process was conducted using COMSOL Multiphysics. The governing equation for temporal and spatial temperature distribution field can be expressed as:

$$\rho C_P \frac{\partial T}{\partial t} - \nabla(k\nabla T) = Q \tag{3.1}$$

Where ρ is the mass density, C_p is the specific heat, and k is the thermal conductivity. Q denotes the volumetric heat source generated by the absorption of laser energy by functional layers within the device.[6-10] The volumetric heat source is delivered as below according to the Beer-Lambert law:

$$Q = I \cdot (1 - R) \cdot \alpha \cdot \exp(-\alpha|z|) \tag{3.2}$$

where I is the 2D energy distribution of the Gaussian laser beam, α is the absorption coefficient, |z| indicates the depth position in z axis orientation.

Further, I can be calculated with the following equation:

$$I = I_0 \cdot \exp\left(\frac{-((x-x_r)^2+(y-y_r)^2)}{2r^2}\right) \tag{3.3}$$

where x_r and y_r are transient spatial coordinates of a laser pulse centre and r represents beam radius , while x and y account for the relative coordinates with respect to the beam centre. I_0 is the source laser beam intensity as expressed below:

$$I_0 = \frac{2P_0}{\pi r_0^2} \tag{3.4}$$

P_0 denotes laser power density, while r_0 is radius of the laser beam spot.

Laser processing parameters in **Table 3.1** are used for the simulation.

3.3 Simulation results

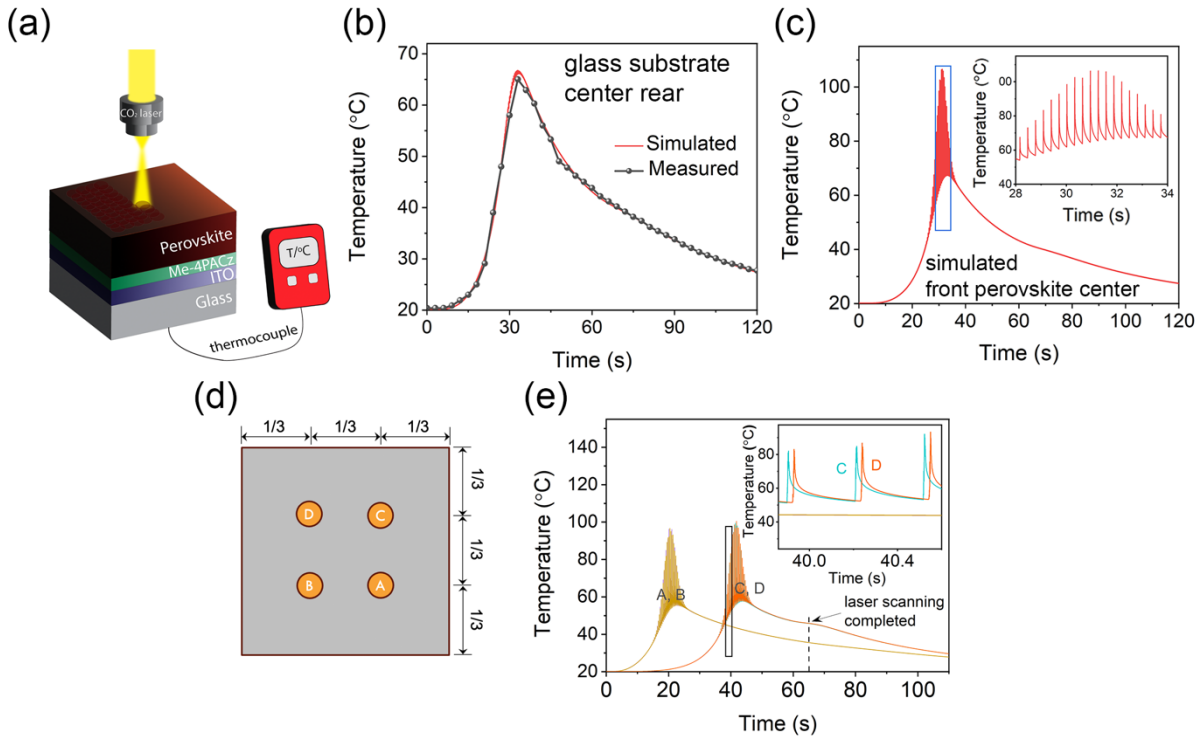

Figure 3.1 (a) Schematic of experimental temperature measurement setup using thermocouple attached to the centre of the glass substrate rear. (b) Comparison of simulated and measured glass temperature over time at the centre rear. (c) Simulated temperature over time of the front perovskite film. Inset: magnified view of the peak temperature region. (d) Schematic and (e) simulated temperature of the perovskite film over time at regions A, B, C, and D which are the typical locations of solar cells.

Figure 3.1a shows the schematic of the structure used for temperature profiling experiment which consists of glass substrate, ITO, Me-4PACz and perovskite layers.

Figure 3.1b shows the glass temperature overtime at the centre rear from the start of the laser processing (t = 0) to the end of the laser processing (t = 61.8s) and after laser processing (t = 61.8 to 120s). Simulated result (peak temperature = 66 °C) agreed with that measured (peak at 65 °C), thereby validating the model.

The temperature at the centre of the front perovskite surface was then modelled. The result in **Figure 3.1c** shows that the peak temperature reached 105 °C while the inset shows periodic heating and cooling at a finer time scale that correspond to the laser being turned on and off during scanning (**Figure 2.2**).

It is important to note that there is a difference of approximately 40 °C between the peak temperatures at the bottom of the glass substrate and at the surface of the perovskite film, demonstrating reduced temperature experience by the substrate.

For the purpose of visualising the temperature profiles from a single laser beam at different times of its scanning, simulations were carried out for the edge of the test structure with (**Figure 3.2**) and without (**Figure 3.3**) the perovskite layer.

Results showed that heat is generated locally by a laser beam (t = 1.0 ms) and is confined to the top ~67 μm of the substrate when the perovskite layer is present or ~0.3 mm of the substrate when the perovskite layer is absent. The perovskite film reached a higher temperature (~70 °C) with a shallower heat profile than the Me-4PACz layer (~32 °C) demonstrating effective laser power absorption by the perovskite film.

As the laser is moved along, cooling can be observed in the original starting position and the cooling is most effective in the perovskite film compared to the Me-4PACz film (c.f., **Figures 3.2 & 3.3** for t > 20 ms). For spatial temperature profiling, four regions A, B, C, and D (**Figure 3.1d**) were selected which are the typical locations of solar cells. Laser scanning commenced near region A, progressed to B, and then C and finished near region D. It is clear from the results (**Figure 3.1e**) that the peak temperatures experienced by the regions are slightly different: Tpeak_D > Tpeak_C > Tpeak_B > Tpeak_A although the difference is small. E.g., Tpeak_D - Tpeak_A < 5°C indicating a small amount of heat transfer from laser-scanned-area to non-laser-scanned area. This implies is that for future laser processing optimisation, laser beam power for regions C and D can be further adjusted or reduced to account for heat transfer from regions A and B to reach the target crystallization temperature. Alternatively, scanning speed can also be increased, reducing overall laser processing time to reduce heat flow between regions. In addition, the model can be used to facilitate new material engineering that incorporates additives in the perovskite film to enhance laser power absorption or the addition of a buffer layer in the cell structure specifically for enhancing laser power absorption. Such optimisation and new cell designs, aided by the developed 3D model validated by experiments can be conducted in the future.

Nevertheless, it can be concluded that i) heat was localised to the top surface leaving the glass substrate at lower temperature; ii) cooling occurred upon departure of the laser beam; and iii) heat was reasonably localised to the vicinity of the laser beam are advantageous for temperature sensitive substrates.

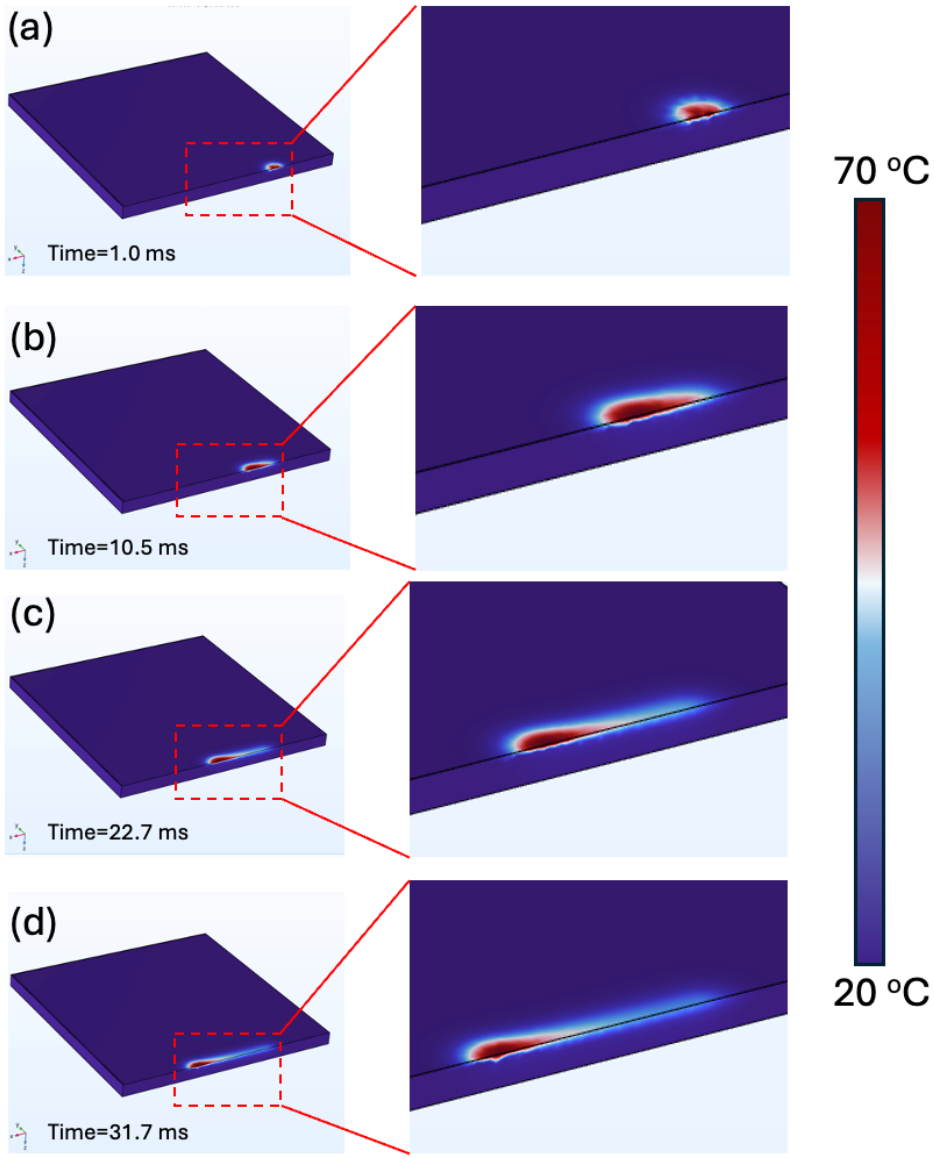

Figure 3.2 Simulated temperature profiles of glass/ITO/Me-4PACz/perovskite at t= (a) 1.0 ms, (b) 10.5 ms, (c) 22.7 ms, and (d) 31.7 ms.

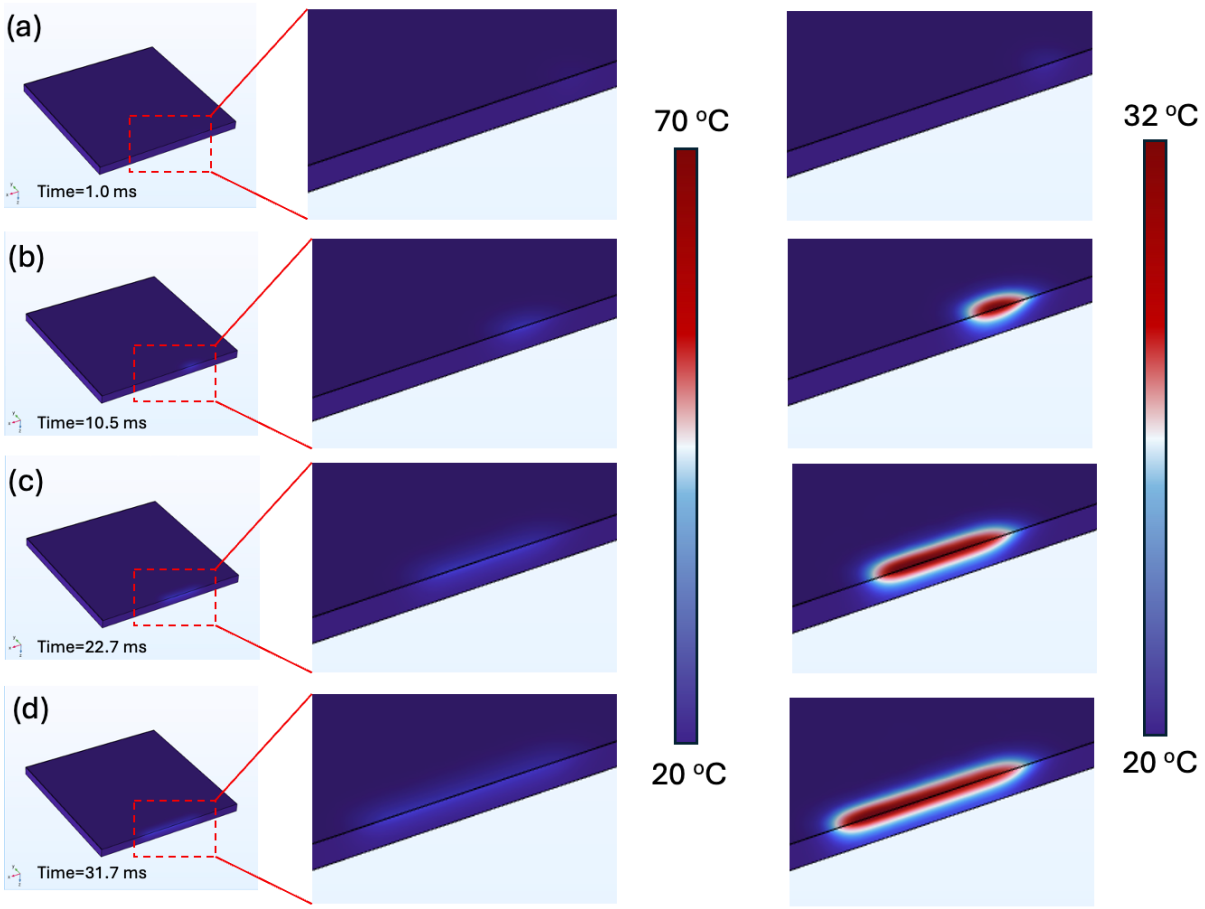

Figure 3.3 Simulated temperature profiles of glass/ITO/Me-4PACz at t= (a) 1.0 ms, (b) 10.5 ms, (c) 22.7 ms, and (d) 31.7 ms.

3.4 Conclusions

Macroscopic and localised time-dependent temperature profiles were modelled using a 3D finite element analysis based on COMSOL Multiphysics. The model verifies that localised annealing is achieved with most of heat confined to the top surface of the substrate. It is shown that the perovskite film is more effective in absorbing laser power absorption and in cooling compared to Me-4PACz. The modelled substrate temperature agreed with that measured, confirming lower glass substrate temperature (~65 °C) during laser annealing compared to 100 °C in the case of conventional hot-plate annealing. Results are promising for low substrate temperature manufacturing process in mass production.

3.5 References

(1) Wlodarczyk, K. L.; Brunton, A.; Rumsby, P.; Hand, D. P. Picosecond laser cutting and drilling of thin flex glass. *Optics and Lasers in Engineering* **2016**, *78*, 64-74. DOI: https://doi.org/10.1016/j.optlaseng.2015.10.001.

(2) Mottay, E.; Liu, X.; Zhang, H.; Mazur, E.; Sanatinia, R.; Pfleging, W. Industrial applications of ultrafast laser processing. *MRS Bulletin* 2016, *41* (12), 984-992. DOI: 10.1557/mrs.2016.275.

(3) Bruening, S.; Du, K.; Gillner, A. High-throughput ultrafast laser micromachining with multiple parallel spots. In Conference on Lasers and Electro-Optics, San Jose, California, *Optica Publishing Group* **2022**, p AM3I.3. DOI: 10.1364/CLEO_AT.2022.AM3I.3.

(4) Abdullayeva, N.; Tuc Altaf, C.; Kumtepe, A.; Yilmaz, N.; Coskun, O.; Sankir, M.; Kurt, H.; Celebi, C.; Yanilmaz, A.; Demirci Sankir, N. Zinc Oxide and Metal Halide Perovskite Nanostructures Having Tunable Morphologies Grown by Nanosecond Laser Ablation for Light-Emitting Devices. *ACS Applied Nano Materials* **2020**, *3* (6), 5881-5897. DOI: 10.1021/acsanm.0c01034.

(5) Trinh, X.-L.; Nguyen, V.-M.; Nguyen, H.-C.; Phan, T.-L.; Kim, H.-C. Temperature-assisted crystallization and morphology for $CH_3NH_3PbI_3$ perovskite solar cells using laser-induced heat treatment. *Organic Electronics* **2024**, *132*, 107099. DOI: https://doi.org/10.1016/j.orgel.2024.107099.

(6) Vora, H.; Dahotre, N. Laser Machining of Structural Alumina: Influence of Moving Laser Beam on the Evolution of Surface Topography. *International Journal of Applied Ceramic Technology* **2015**, *12* (3), 665-678. DOI: https://doi.org/10.1111/ijac.12223.

(7) Vora, H. D.; Dahotre, N. B. Multiphysics Theoretical Evaluation of Thermal Stresses in Laser Machined Structural Alumina. *Lasers in Manufacturing and Materials Processing* **2015**, *2* (1), 1-23. DOI: 10.1007/s40516-014-0004-x.

(8) Son, Y.-I.; Shin, J. Numerical Study on the Laser Annealing of Silicon Used in Advanced V-NAND Device. *Materials* **2022**, *15* (12). DOI: 10.3390/ma15124201.

(9) Vora, H. D.; Santhanakrishnan, S.; Harimkar, S. P.; Boetcher, S. K. S.; Dahotre, N. B. One-dimensional multipulse laser machining of structural alumina: evolution of surface topography. *The International Journal of Advanced Manufacturing Technology* **2013**, *68* (1), 69-83. DOI: 10.1007/s00170-012-4709-8.

(10) Yuan, Z.; Lou, Q.; Zhou, J.; Dong, J.; Wei, Y.; Wang, Z.; Zhao, H.; Wu, G. Numerical and experimental analysis on green laser crystallization of amorphous silicon thin films. *Optics & Laser Technology* **2009**, *41* (4), 380-383. DOI: https://doi.org/10.1016/j.optlastec.2008.09.003.

Chapter 4 All-Laser-Annealed Wide Bandgap Perovskite Solar Cells

4.1 Introduction

As discussed in Chapter 1 Section 1.3.3, efficient wide bandgap perovskites (bandgap > 1.70 eV) are essential for tandem, but many suffer from open-circuit voltage losses (W_{OC}) limiting efficiencies achievable by tandem devices. As discussed, W_{OC} can be reduced by a well-designed and appropriately fabricated hole transport layer (HTL) enables energy level alignment and perovskite/HTL interface with reduced surface passivation. While self-assembly mono-layer (SAM) type HTLs have become popular in the state-of-the-art high efficiency perovskite single junction and tandem solar cells, prior to this thesis, there has been no report on laser processing of SAM HTL for perovskite solar cells.

Therefore, this chapter develops effective laser annealing processes in ambient for fabricating (4-(3,6-Dimethyl-9H-carbazol-9-yl)butyl)phosphonic acid (Me-4PACz) SAM HTL and WBG 1.80 eV $FA_{0.8}Cs_{0.2}PbI_{1.8}Br_{1.2}$ perovskite layers.

4.2 Experimental methods

Materials

Materials and solvents used in this chapter were identical to those in Chatper 2 (see Section 2.2). In addition, methylammonium chloride (MACl) was purchased from GreatCell Solar Materials. (4-(3,6-Dimethyl-9H-carbazol-9-yl)butyl)phosphonic acid (Me-4PACz) and lead bromide ($PbBr_2$) were purchased from TCI.

Laser annealing

Laser annealing conditions from chapter 2 and laser processing parameters from Table 3.1 were also used in this chapter except for the laser power ratio. In this chapter, the ratio was optimized to be 32%, giving a power density of ~1.4 kW/cm^2 for the wider bandgap perovskite layer in this chapter.

For the search of optimum laser power for Me-4PACz annealing, 5%; 15%; 25%; 35%; 45%;

55%; 65%; 75%; 85%; 95%; 100% of the maximum power setting were used initially and complete device performances were compared to determine the optimized laser power ratio, which was 35% and the optimal power was 17.5 W.

Device fabrication

ITO glass substrate cleaning process in this chapter is identical to that in Chapter 2 except the last step whereby rinsed and dry substrates were treated by oxygen plasma for 2 minutes.

Hole transport layer solution was prepared by dissolving Me-4PACz into a mixture solvent of methanol:dimethylformamide (DMF) (95:5 vol%), with a concentration of 0.5 mg/mL. The Me-4PACz solution was deposited onto the ITO substrates by spin coating, at a spin rate of 4000 rpm for 16s. The film was then either annealed on a hot plate at 85 °C for 10 minutes within a N_2 filled glove box (GTA) or transferred out of glovebox for ambient laser annealing (ALA) – see details above.

Wide bandgap perovskite (WBG) $FA_{0.8}Cs_{0.2}PbI_{1.8}Br_{1.2}$, (with potassium hexafluorophosphate (KPF_6) and MACl additives) solution was prepared by mixing FAI (206.4 mg), cesium iodide (CsI, 77.9 mg), $PbBr_2$ (276.6 mg), PbI_2 (692 mg), KPF_6 (4.0 mg), and MACl (1.0 mg) in a DMF (900 μL):NMP (100 μL) binary solvent. The corresponding concentration was 1.5 M. WBG perovskite precursor solution was stirred with a vortex mixer at room temperature for 30 min before use. 80 μL of WBG perovskite precursor solution was spin-coated onto the Me-4PACz layer with an acceleration of rate of 400 rpm/s, and a spin rate of 4000 rpm for 50s. 15s into the spin coating, N_2 gas quenching (at a pressure of ~100 psi) was applied. The deposited WBG perovskite precursor film was then either annealed on a hot plate within a N_2 filled glove box (GTA) at 100 °C, for at least 10 minutes or transferred out of glovebox for ambient laser annealing (ALA) – see details above.

Finally, LiF (1.0 nm), C_{60} (20 nm), BCP (6 nm) and Cu (100 nm) were deposited sequentially using a thermal evaporator.

Device and film characterizations

Methods for current density-voltage (*J-V*) measurements; external quantum efficiency (EQE) measurements; light intensity-dependent V_{OC} measurements; scanning electron microscopy (SEM); X-ray diffraction (XRD) measurements; steady-state and time-resolved photoluminescence measurements; determination of carrier lifetimes; and X-ray photoelectron spectra (XPS) and depth-resolved XPS measurements used in this chapter are identical to those in Chapter 2.

Fully fabricated solar devices were used for current *J-V*, EQE, light-intensity-dependent V_{OC}

measurements.

Test structures of perovskite/Me-4PACz/ITO/glass were used for SEM, XRD, optical absorption and photoluminescence measurements.

4.3 Results and discussions

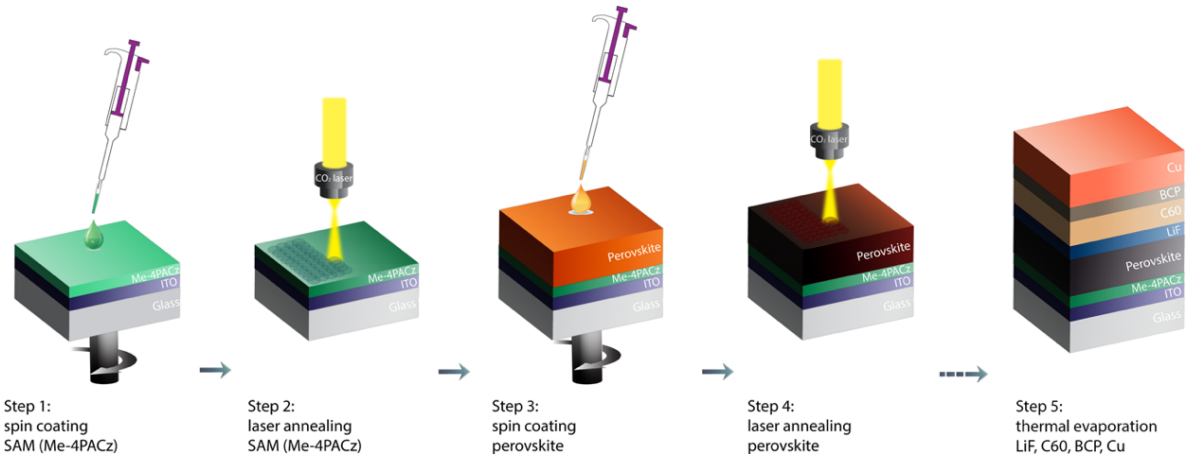

Figure 4.1. Schematic of process flow for fabricating wide bandgap perovskite solar cells utilising laser annealing for both the hole transport layer and the perovskite layer.

To demonstrate ambient laser annealing (ALA) for fabricating both the Me-4PACz and the perovskite layers for WBG perovskite cells, the process sequence and cell structure illustrated in **Figure 4.1** was developed. After ALA, depositions of lithium fluoride (LiF), fullerene (C_{60}), bathocuproine (BCP) to facilitate electron transport to the copper (Cu) electrode were carried out to complete cell fabrications. For comparisons, control cells were also fabricated using hot-plate thermal annealing in a N_2 filled glove-box (GTA) for both the Me-4PACz and the perovskite layers or for the Me-4PACz layer only.

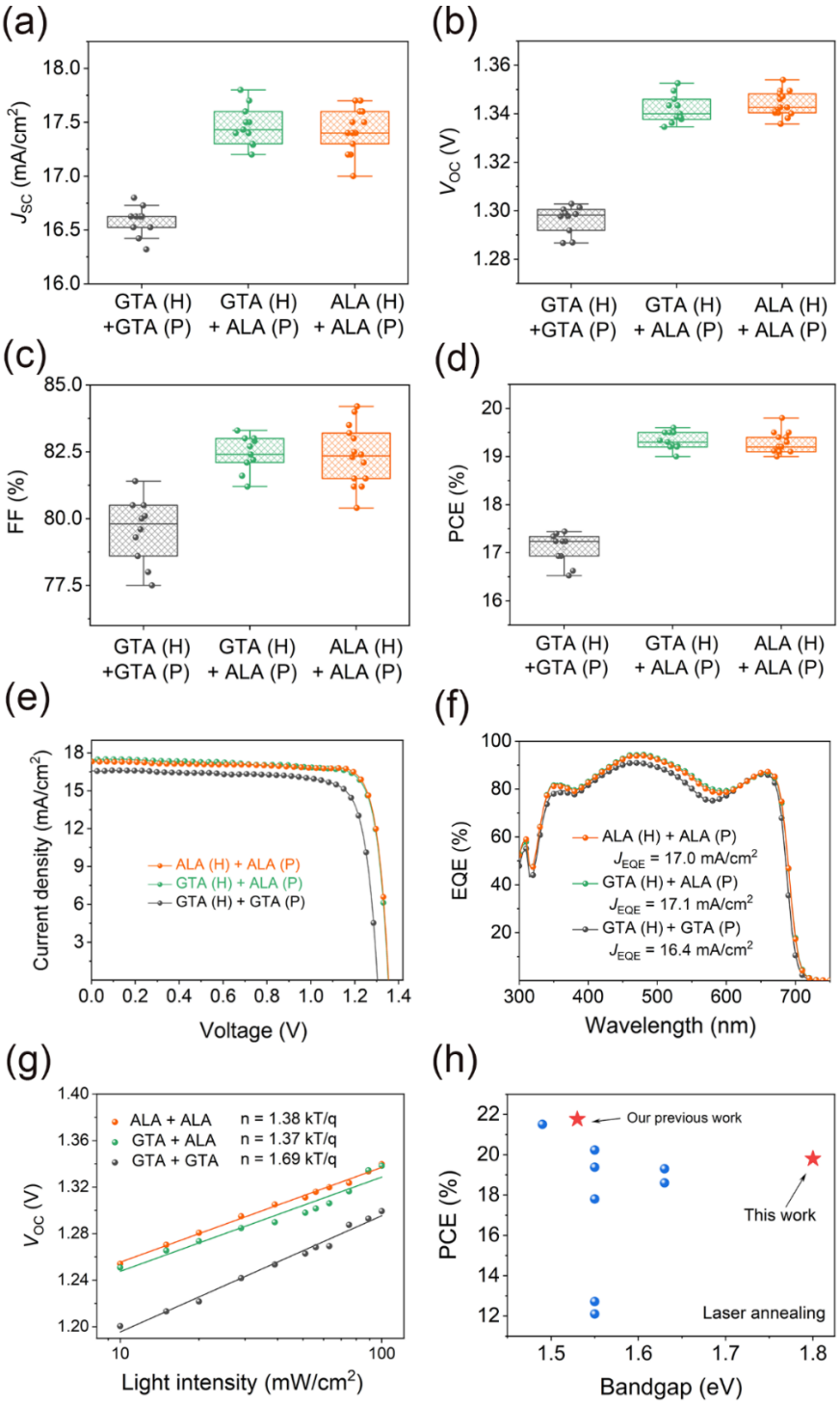

Figure 4.2 Performance of devices annealed by glovebox thermal annealing (GTA) for both hole transport (H) and perovskite (P) layers (grey); ambient (relativity humidity of 30 to 40%) laser annealing (ALA) for both layers (orange); and a combination of GTA and ALA for H and P layers, respectively (green). Distributions: (a) short-circuit current density (J_{SC}), (b) open-circuit voltage (V_{OC}), (c) fill factor (FF), and (d) power conversion efficiency (PCE) for GTA (H) + GTA (P) cells; GTA (H) + ALA (P) cells; and ALA (H) + ALA (P) cells. (e) Light current density-voltage (J-V) and(f) external quantum efficiency (EQE) plots of the champion devices in each category. (g) Light-dependent V_{OC} for representative cells in each category. (h) Plot of PCEs of laser-annealed perovskite solar cells reported[1-8] compared to our work.

Table 4.1 Summary of average and champion device performances. ALA devices were processed under relativity humidity of 30 to 40%.

Annealing	Avg. / Best	J_{SC} (mA cm^{-2})	V_{OC} (V)	FF (%)	PCE (%)
GTA(H)+GTA(P)	Average	16.5±0.1	1.30±0.01	79.6±1.2	17.1±0.3
	Champion	16.6	1.30	80.5	17.4
GTA(H)+ALA(P)	Average	17.5±0.2	1.34±0.01	82.4±0.6	19.3±0.2
	Champion	17.5	1.35	82.4	19.5
ALA(H)+ALA(P)	Average	17.4±0.2	1.34±0.01	82.3±1.1	19.3±0.2
	Champion	17.4	1.35	84.2	19.8

Results are shown in **Figure 4.2** and **Table 4.1**. The ALA process when applied to the perovskite layer increased average device PCE by 2.1% absolute for the champion device due to the improvements in all electrical parameters. While ALA when applied to both layers did not improve the average device PCE further, it is clear that ALA does not result in any detrimental effect to the HTL either. The ALA process even though conducted in ambient (relativity humidity of 30 to 40%) did not increase the spread of electrical parameters either. Notably, at the time of reporting, this was the first for 1.80 eV perovskite cell fabricated by laser annealing (**Figure 4.2h**). In addition, the V_{OC}, FF and PCE achieved by the all-ALA champion cell were also the highest for WBG (1.80 eV) perovskite cells (**Figure 4.3**).

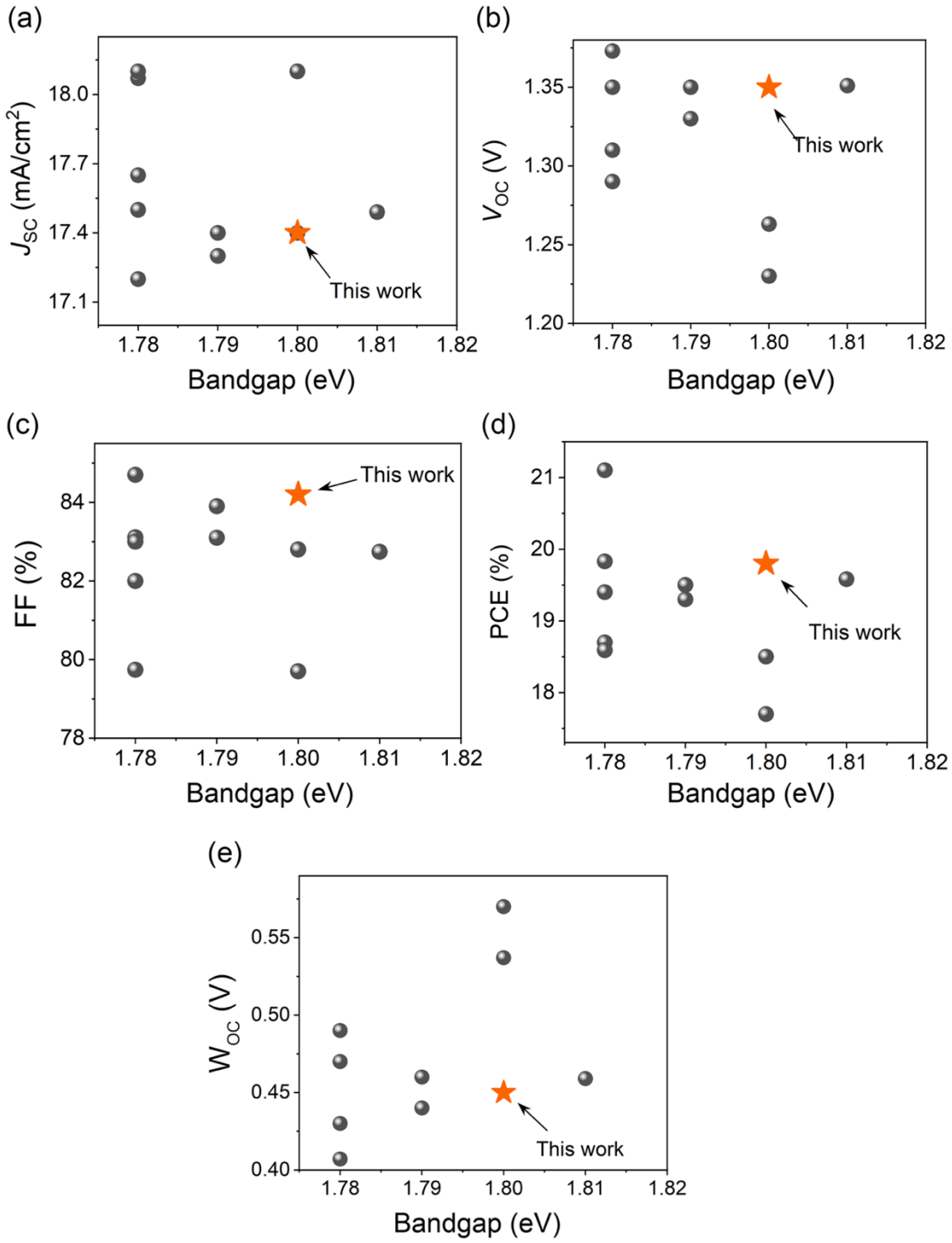

Figure 4.3. Cell parameters of reported WBG perovskite cells in the last 3 years. Values are also listed in **Table 4.2**.

Table 4.2 Cell parameters of reported WBG perovskite cells in the last 3 years.

Year	E_g (eV)	J_{SC} (mA/cm^2)	V_{OC} (V)	FF (%)	PCE (%)	W_{OC} (V)	Ref.
2024	1.81	17.5	1.351	82.7	19.6	0.459	[9]
2023	1.78	17.7	1.350	83.1	19.8	0.430	[10]
2022	1.80	17.4	1.263	79.7	17.7	0.537	[11]
2024	1.78	17.5	1.350	82.0	19.4	0.430	[12]
2024	1.78	17.2	1.310	83.0	18.7	0.470	[13]
2023	1.80	18.1	1.230	82.8	18.5	0.570	[14]
2024	1.78	18.1	1.290	79.7	18.6	0.490	[15]
2023	1.79	17.3	1.330	83.9	19.3	0.460	[16]
2024	1.79	17.4	1.350	83.1	19.5	0.440	[17]
2025	1.78	18.1	1.373	84.7	21.1	0.407	[18]

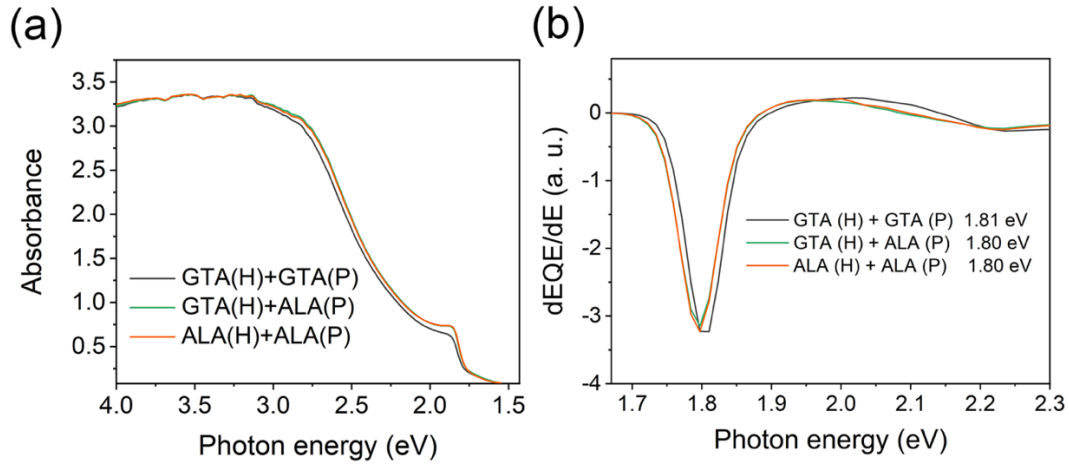

Figure 4.4. (a) Absorbance (b) dEQE/dE spectra for GTA and ALA perovskite/ Me-4PACz stacks and complete solar cells, respectively.

The J_{SC} increase in laser annealed perovskite cells (**Figure 4.2a**) correlated with the relatively broadband improvement in the corresponding external quantum efficiencies (EQE) (**Figure 4.2f**) and absorption coefficients (**Figure 4.4a**). This is due to the improved film quality in the laser annealed perovskite films with enlarged grain size (cf. **Figures 4.5e** & **4.5f with Figure 4.5d**). Large grain size has been previously observed in laser annealed films compared to hot-plate annealed perovskite film.[5, 19] As discussed in Chapter 2, laser annealing facilitated rapid solvent evaporation, nucleation, crystallization and grain growth that is not restricted the growth can extend to regions that are not yet irradiated as opposed to grain growth induced by hot-plate that self-limits as neighbouring grains impinge on each other. This can be seen in the cross-sectional scanning electron microscopy images of ALA perovskite films (Figures 4.5b&c) when compared to the GTA perovskite film (Figures 4.5a). It is clear that larger columnar grains can be observed in ALA perovskites and when on ALA HTL, the grains were vertically continuous. ALA perovskites on the other hand exhibit smaller equiaxed like vertically dis-

continuous grains.

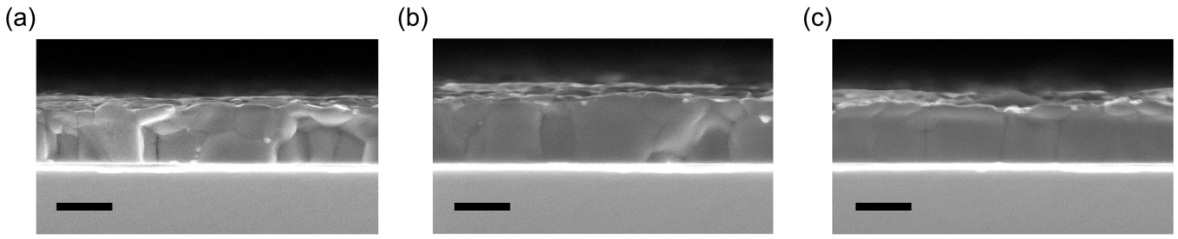

Figure 4.5 Cross-sectional SEM images of perovskite films on Me-4PACz processed by (a) GTA (H)+GTA(P), (b) GTA(H)+ALA(P) and (c) ALA (H)+ALA(P). Scale bar = 500 nm..

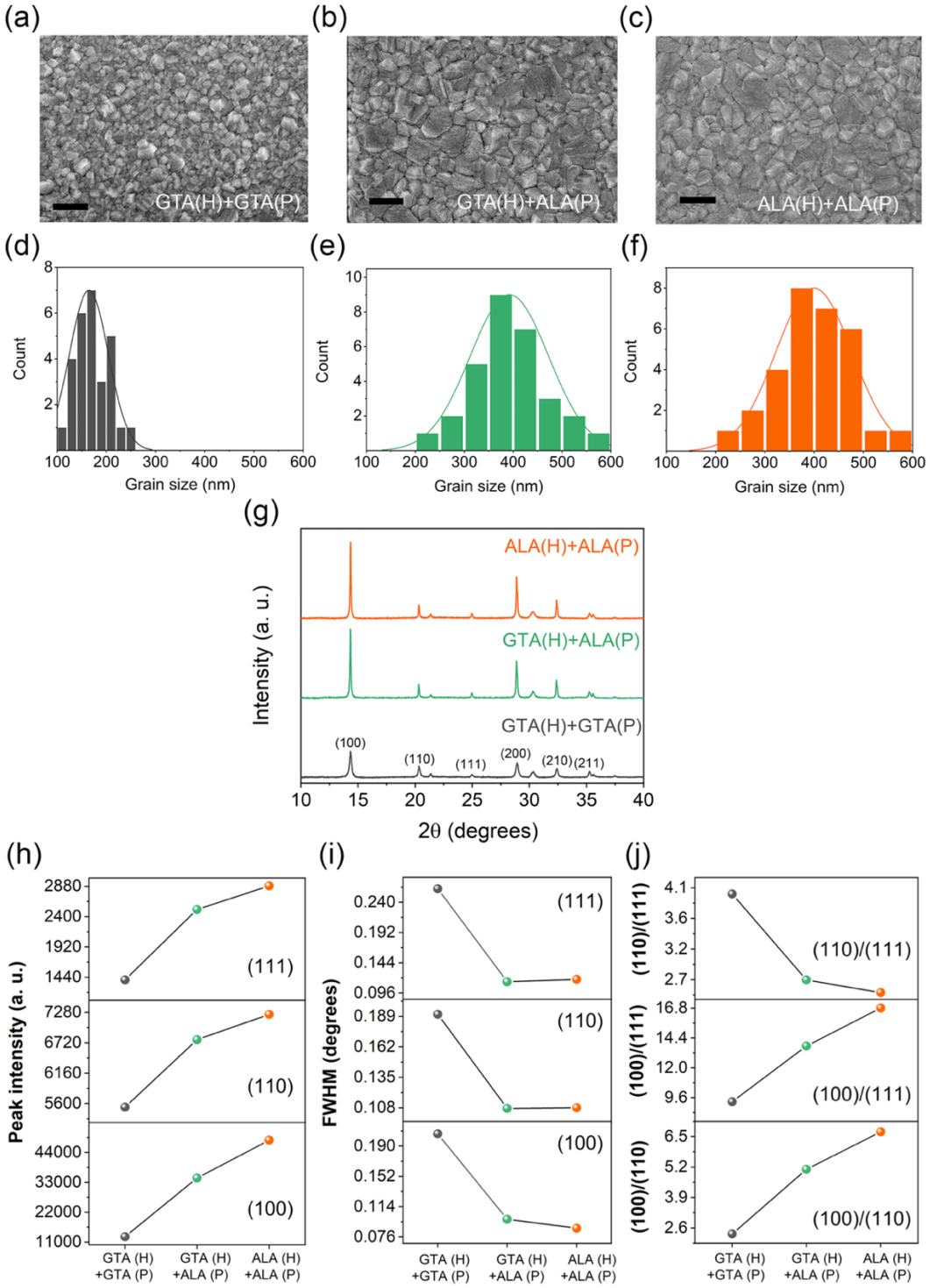

Figure 4.6 Scanning electron microscopy (SEM) images of perovskite films on Me-4PACz processed by (a) GTA (H)+GTA (P), (b) GTA (H)+ALA (P) and (c) ALA (H) + ALA (P). Scale bar = 500 nm. (d-f) Distribution of grain sizes for perovskite films in (a)-(c). (g) X-ray diffraction (XRD) patterns of the same films. Corresponding (h) intensities of the perovskite (111) (top), (110) (middle), (100) (bottom) diffraction peaks; (i) full-width at half-maxima (FWHM); and (j) Intensity ratios of (110)/(111), (100)/(111), and (100)/(110).

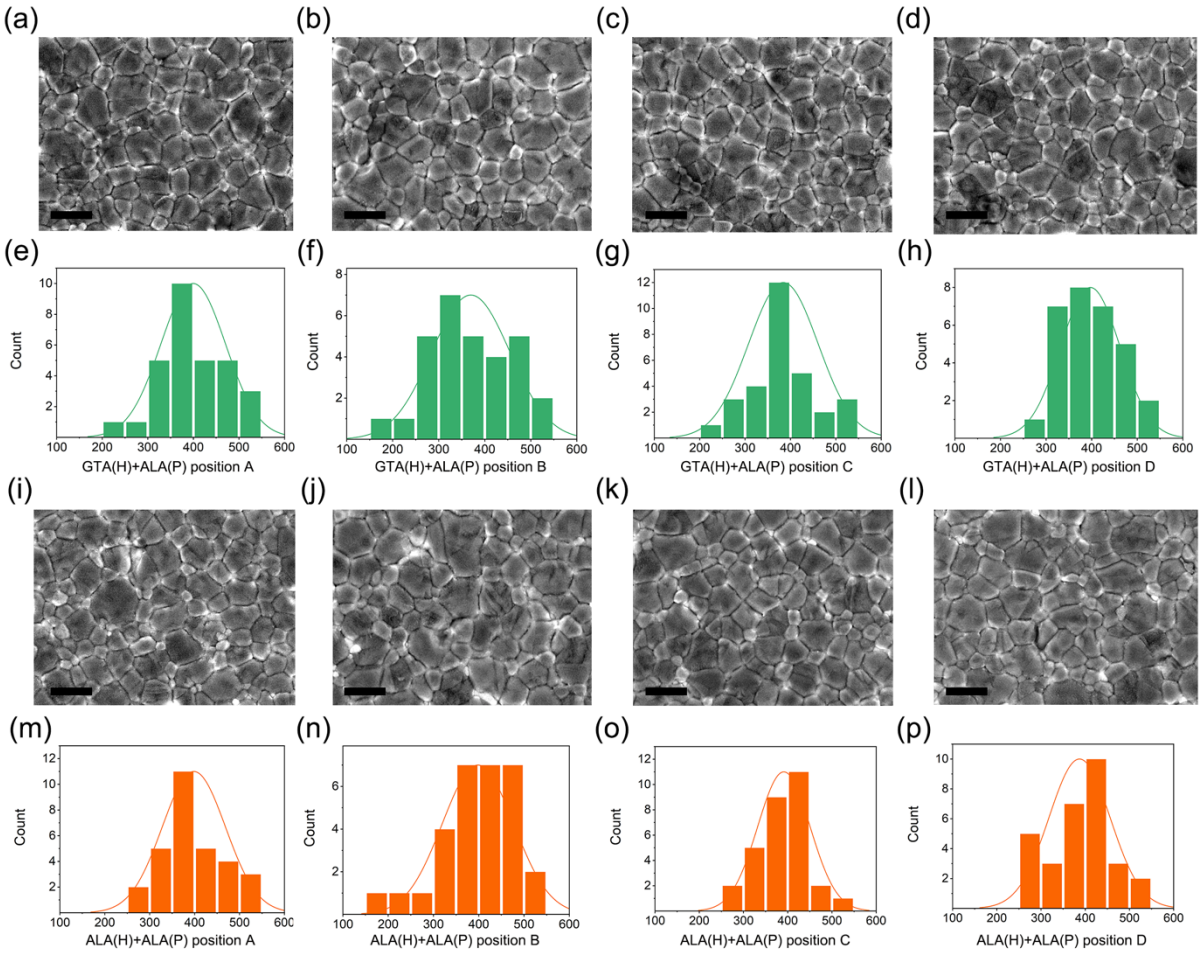

Figure 4.7 Scanning electron microscopy (SEM) images of perovskite films on Me-4PACz processed by (a) GTA (H)+GTA (P), (b) GTA (H)+ALA (P) at positions A, B, C, & D as illustrated in **Figure 3.1d**. Scale bar = 500 nm. (e-h, m-p) Distribution of grain sizes for the same films.

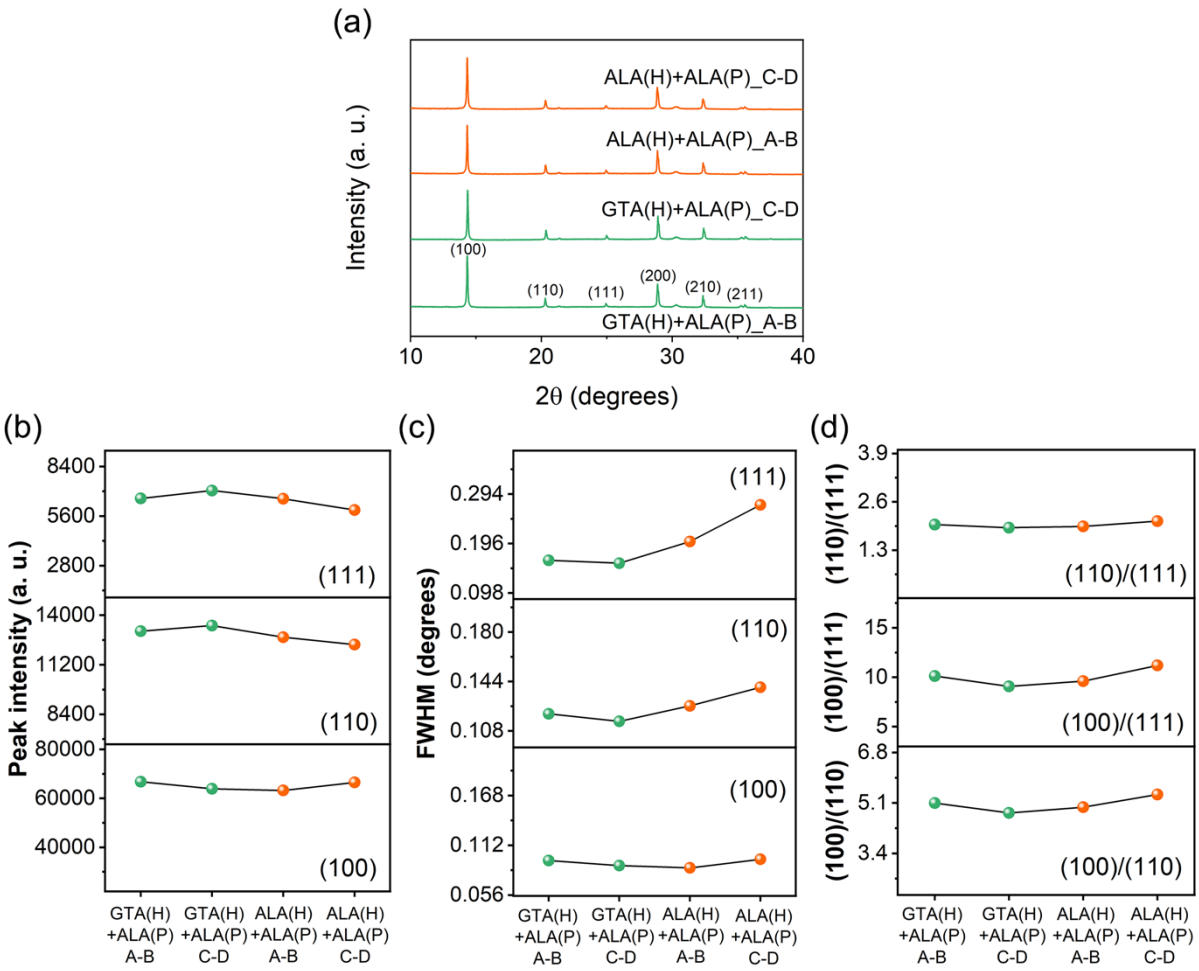

Figure 4.8 (a) X-ray diffraction (XRD) patterns of perovskite films on Me-4PACz processed by GTA (H)+GTA (P) (green) and ALA (H)+ALA (P) (orange) over regions A&B, of C& D as illustrated in Figure 3.1d. Corresponding (b) intensities and (c) full-width at half-maxima (FWHM) of the perovskite (111) (top), (110) (middle), (100) (bottom) diffraction peaks. (d) Intensity ratios of (110)/(111), (100)/(111), and (100)/(110).

The observed larger columnar grains in laser annealed perovskites help explain the better crystallinity as characterised by X-ray diffraction (XRD) measurements (**Figure 4.6g**). The peaks for the key crystalline phases ((100), (110) and (111)) showed enhanced intensity (**Figure 4.6h**) and reduced full width at half maximum (FWHM) (**Figure 4.6i**) in laser annealed perovskites that also have increased preference to the (100) crystal orientation (**Figure 4.6j**). The laser annealed films are also relatively uniform showing similar grain sizes (**Figure 4.7**) in and crystallinities (**Figure 4.8**) at different locations of the film.

The better perovskite film quality therefore led to reduced defect-related non-radiative carrier recombination in the associated solar cells which can be seen in the results of their light-dependent V_{OC} measurements (**Figure 4.2g**) showing the reduction in ideality factor from ~1.7 to ~1.4 in ALA cells.

The reduced defect-related non-radiative carrier recombination is also supported by significant increase in steady-state photoluminescence (PL) (**Figure 4.9a**) and significant increase in carrier lifetimes (**Table 4.3** obtained from **Figure 4.9b**) in ALA perovskites that explain the increase in V_{OC} in the corresponding cells.

The very small red shift observed in the PL peak in ALA perovskites and in the bandgap of the corresponding cells can be explained by the increase in iodine-to-lead and iodine-to-bromine ratios (I/Pb, I/Br) in the ALA perovskites compared to the GTA one (**Table 4.3**) extracted from results of x-ray photoelectron spectroscopy (XPS) (**Figure 4.10**).

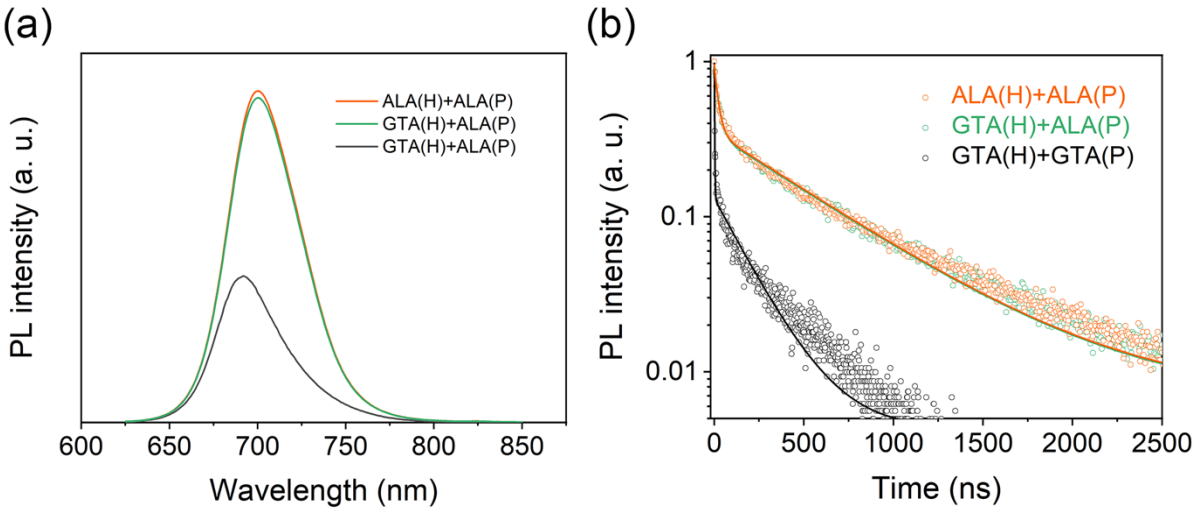

Figure 4.9. (a) Steady-stage and (b) time resolved photoluminescence curves for GTA and ALA films.

Table 4.3 Fitted lifetimes from measured time-resolved photoluminescence (TrPL) (**Figure 4.9b**) of GTA and ALA perovskite/ Me-4PACz stacks.

Annealing	τ_1/ns	A_1/%	τ_2/ns	A_2/%	Effective lifetime/ns
GTA(H)+GTA(P)	1.3	84.4	135.0	12.7	127.0
GTA(H)+ALA(P)	16.3	60.3	396.9	33.8	370.8
ALA(H)+ALA(P)	15.5	60.3	395.6	34.3	371.1

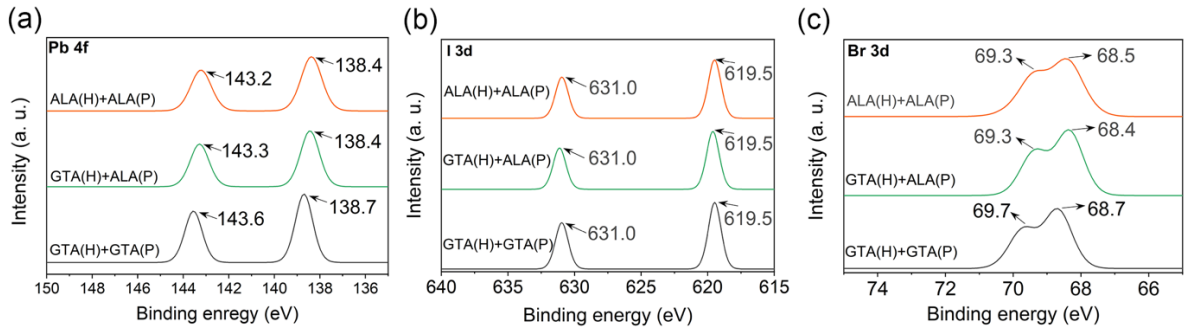

Figure 4.10 The deconvoluted high-resolution X-ray photoelectron spectroscopy (XPS) spectra of (a) Pb 4f, (b) I 3d, (c) Br 3d for GTA and ALA films. The both Pb 4f and Br 3d peaks

are at lower binding energies in ALA perovskites compared to those in GTA perovskites, suggesting less uncoordinated Pb and Br ions[20-22] while there are negligible differences between the I 3d peaks in the ALA or GTA perovskites.

Table 4.4 Calculated averaged relative atomic ratio of I/Pb, Br/Pb, I/Br based on XPS results in **Figure 4.10**.

Annealing	I/Pb ratio	Br/Pb	I/Br
GTA(H)+GTA(P)	2.49	1.65	1.51
GTA(H)+ALA(P)	2.60	1.68	1.55
ALA(H)+ALA(P)	2.67	1.69	1.58

4.4 Conclusion

In this work, an all-laser-annealing for wide bandgap (1.80 eV) perovskite solar cell fabrication using a low photon energy CO_2 laser was successfully demonstrated, for the first time. The laser process dramatically reduced annealing time by a factor of 10 and reduced temperature experienced by the substrate. The laser annealed devices produced low voltage loss (W_{OC}) of 0.45 V. The high open circuit voltage (V_{OC}) of 1.35 V and high-power conversion efficiency (PCE) of 19.8% were the highest for 1.80 eV perovskite cells at the time of reporting. This was due to significant enhancement in perovskite crystal size, crystallinity resulting in reduced defect related non-radiative recombination in laser perovskite films and devices.

The demonstrated laser annealing technique not only enables faster and more energy-efficient fabrication but also holds promise for scalable, high-throughput manufacturing of perovskite solar cells. Future studies could further optimize laser parameters to enhance film quality and investigate the long-term stability of laser-annealed devices, paving the way for broader adoption of laser processing in perovskite photovoltaics.

4.5 References

(1) Jeon, T.; Jin, H. M.; Lee, S. H.; Lee, J. M.; Park, H. I.; Kim, M. K.; Lee, K. J.; Shin, B.; Kim, S. O. Laser Crystallization of Organic–Inorganic Hybrid Perovskite Solar Cells. *ACS Nano* **2016**, *10* (8), 7907-7914. DOI: 10.1021/acsnano.6b03815.

(2) Li, F.; Zhu, W.; Bao, C.; Yu, T.; Wang, Y.; Zhou, X.; Zou, Z. Laser-assisted crystallization of $CH_3NH_3PbI_3$ films for efficient perovskite solar cells with a high open-circuit voltage.

Chemical Communications **2016**, *52* (31), 5394-5397, 10.1039/C6CC00753H. DOI: 10.1039/C6CC00753H.

(3) Shan, X.; Wang, S.; Dong, W.; Pan, N.; Shao, J.; Wang, X.; Tao, R.; Deng, Z.; Hu, L.; Kong, F.; et al. Flash Surface Treatment of $CH_3NH_3PbI_3$ Films Using 248 nm KrF Excimer Laser Enhances the Performance of Perovskite Solar Cells. *Solar RRL* **2019**, *3* (7), 1900020. DOI: https://doi.org/10.1002/solr.201900020.

(4) Kong, W.; Zhao, C.; Xing, J.; Zou, Y.; Huang, T.; Li, F.; Yang, J.; Yu, W.; Guo, C. Enhancing Perovskite Solar Cell Performance through Femtosecond Laser Polishing. *Solar RRL* **2020**, *4* (7), 2000189. DOI: https://doi.org/10.1002/solr.202000189.

(5) You, P.; Li, G.; Tang, G.; Cao, J.; Yan, F. Ultrafast laser-annealing of perovskite films for efficient perovskite solar cells. *Energy & Environmental Science* **2020**, *13* (4), 1187-1196. DOI: 10.1039/C9EE02324K.

(6) Trinh, X.-L.; Tran, N.-H.; Seo, H.; Kim, H.-C. Enhanced performance of perovskite solar cells via laser-induced heat treatment on perovskite film. *Solar Energy* **2020**, *206*, 301-307. DOI: https://doi.org/10.1016/j.solener.2020.05.063.

(7) Kedia, M.; Rai, M.; Phirke, H.; Aranda, C. A.; Das, C.; Chirvony, V.; Boehringer, S.; Kot, M.; Byranvand, M. M.; Flege, J. I.; et al. Light Makes Right: Laser Polishing for Surface Modification of Perovskite Solar Cells. *ACS Energy Letters* **2023**, *8* (6), 2603-2610. DOI: 10.1021/acsenergylett.3c00469.

(8) Yi, J.; Leung, T.-L.; Digweed, J.; Bing, J.; Bailey, C.; Liao, C.; Tao, R.; Wang, G.; Li, Z.; Nguyen, H. T.; et al. CO_2 Laser Crystallization in Ambient for Highly Efficient $FAPbI_3$ Perovskite Solar Cells. *Small* **2024**, *20* (45), 2402215. DOI: https://doi.org/10.1002/smll.202402215.

(9) Wu, S.; Yan, Y.; Yin, J.; Jiang, K.; Li, F.; Zeng, Z.; Tsang, S.-W.; Jen, A. K. Y. Redox mediator-stabilized wide-bandgap perovskites for monolithic perovskite-organic tandem solar cells. *Nature Energy* **2024**, *9* (4), 411-421. DOI: 10.1038/s41560-024-01451-8.

(10) Cui, H.; Huang, L.; Zhou, S.; Wang, C.; Hu, X.; Guan, H.; Wang, S.; Shao, W.; Pu, D.; Dong, K.; et al. Lead halide coordination competition at buried interfaces for low V_{OC}-deficits

in wide-bandgap perovskite solar cells. *Energy & Environmental Science* **2023**, *16* (12), 5992-6002. DOI: 10.1039/D3EE02818F.

(11) Wen, J.; Zhao, Y.; Liu, Z.; Gao, H.; Lin, R.; Wan, S.; Ji, C.; Xiao, K.; Gao, Y.; Tian, Y.; et al. Steric Engineering Enables Efficient and Photostable Wide-Bandgap Perovskites for All-Perovskite Tandem Solar Cells. *Advanced Materials* **2022**, *34* (26), 2110356. DOI: https://doi.org/10.1002/adma.202110356.

(12) Jiang, Q.; Tong, J.; Scheidt, R. A.; Wang, X.; Louks, A. E.; Xian, Y.; Tirawat, R.; Palmstrom, A. F.; Hautzinger, M. P.; Harvey, S. P.; et al. Compositional texture engineering for highly stable wide-bandgap perovskite solar cells. *Science* **2022**, *378* (6626), 1295-1300. DOI: 10.1126/science.adf0194.

(13) Li, S.; Zheng, Z.; Ju, J.; Cheng, S.; Chen, F.; Xue, Z.; Ma, L.; Wang, Z. A Generic Strategy to Stabilize Wide Bandgap Perovskites for Efficient Tandem Solar Cells. *Advanced Materials* **2024**, *36* (9), 2307701. DOI: https://doi.org/10.1002/adma.202307701.

(14) Li, T.; Xu, J.; Lin, R.; Teale, S.; Li, H.; Liu, Z.; Duan, C.; Zhao, Q.; Xiao, K.; Wu, P.; et al. Inorganic wide-bandgap perovskite subcells with dipole bridge for all-perovskite tandems. *Nature Energy* **2023**, *8* (6), 610-620. DOI: 10.1038/s41560-023-01250-7.

(15) Li, Y.; Yan, Y.; Fu, Y.; Jiang, W.; Liu, M.; Chen, M.; Huang, X.; Lu, G.; Lu, X.; Yin, J.; et al. Highly Durable Inverted Inorganic Perovskite/Organic Tandem Solar Cells Enabled by Multifunctional Additives. *Angewandte Chemie International Edition* **2024**, *63* (52), e202412515. DOI: https://doi.org/10.1002/anie.202412515.

(16) Chen, H.; Maxwell, A.; Li, C.; Teale, S.; Chen, B.; Zhu, T.; Ugur, E.; Harrison, G.; Grater, L.; Wang, J.; et al. Regulating surface potential maximizes voltage in all-perovskite tandems. *Nature* **2023**, *613* (7945), 676-681. DOI: 10.1038/s41586-022-05541-z.

(17) Chen, M.; Li, Y.; Zeng, Z.; Liu, M.; Du, T.; Huang, X.; Bi, L.; Wang, J.; Jiang, W.; An, Y.; et al. Regulating the crystallization of mixed-halide perovskites by cation alloying for perovskite–organic tandem solar cells. *Energy & Environmental Science* **2024**, *17* (24), 9580-9589. DOI: 10.1039/D4EE03045A.

(18) Liu, Z.; Lin, R.; Wei, M.; Yin, M.; Wu, P.; Li, M.; Li, L.; Wang, Y.; Chen, G.; Carnevali, V.; et al. All-perovskite tandem solar cells achieving >29% efficiency with improved (100) orientation in wide-bandgap perovskites. *Nature Materials* **2025**. DOI: 10.1038/s41563-024-02073-x.

(19) Yang, H.; Peng, M.; Yi, W.; Jiang, H.; Cheng, G. J. Oriented Perovskite Film from Laser Recrystallization in Magnetic Field. *Advanced Materials* **2023**, *35* (45), 2303635. DOI: https://doi.org/10.1002/adma.202303635.

(20) Azam, M.; Ma, Y.; Zhang, B.; Shao, X.; Wan, Z.; Zeng, H.; Yin, H.; Luo, J.; Jia, C. Tailoring pyridine bridged chalcogen-concave molecules for defects passivation enables efficient and stable perovskite solar cells. *Nature Communications* **2025**, *16* (1), 602. DOI: 10.1038/s41467-025-55815-z.

(21) Fu, Q.; Tang, X.; Liu, H.; Wang, R.; Liu, T.; Wu, Z.; Woo, H. Y.; Zhou, T.; Wan, X.; Chen, Y.; et al. Ionic Dopant-Free Polymer Alloy Hole Transport Materials for High-Performance Perovskite Solar Cells. *Journal of the American Chemical Society* **2022**, *144* (21), 9500-9509. DOI: 10.1021/jacs.2c04029.

(22) Wang, H.; Zou, W.; Luo, H.; Quan, Y.; Yang, L.; Liu, X.; Li, H. Ion migration inhibition and defect passivation via sulfonate salt coordination for high-performance perovskite solar cells with enhanced phase stability. *Journal of Materials Chemistry C* **2023**, *11* (39), 13518-13525. DOI: 10.1039/D3TC02032K.

Chapter 5 Laser-Annealed Organic Photovoltaic (OPV) and Perovskite-OPV Tandem Solar Cells

5.1 Introduction

As discussed in Chapter 1 Section 1.3.4, while there has been a growing interest in developing laser processes for perovskite[1-8] or organic solar cell fabrication[9-11]. In addition, the ability of conducting annealing in ambient lowers the barrier to industrial translation. Out of the 50 perovskite-OPV tandem solar cells reported at the time of the writing of this thesis, there are only two that were annealed in the ambient (**Table 5.1**) and there is none that uses laser annealing for all the layers in the tandem (**Table 5.1**).

Therefore, this chapter demonstrates the use of ambient laser annealing (ALA) for the fabrication of PM6:Y6 OPV and perovskite-OPV tandem solar cells for the first time.

Table 5.1. Annealing methods used and J_{EQE} of each sub-cell for reported perovskite-OPV tandem solar cells. "NR" = not reported.

Perovskite-OPV Tandem				Perovskite					OPV					Annealing		Ref
V_{OC} (V)	J_{SC} (mA /cm^2)	FF (%)	PCE (%)	V_{OC} (V)	J_{SC} (mA /cm^2)	FF (%)	PCE (%)	J_{EQE} (mA /cm^2)	V_{OC} (V)	J_{SC} (mA /cm^2)	FF (%)	PCE (%)	J_{EQE} (mA /cm^2)	Method	Atmosphere	
2.10	14.7	80.0	25.1	1.37	16.1	84.2	18.5	14.5	0.85	26.2	74.5	16.7	14.5	Thermal	Glove box	12
2.10	14.4	76.6	23.2	1.29	18.1	79.7	18.6	14.3	0.86	27.2	76.3	17.9	14.1	Thermal	Air	13
2.10	14.7	80.5	25.1	1.30	16.6	84.6	18.2	14.5	0.86	28.1	78.4	18.9	14.5	Thermal	Glove box	14
1.90	13.9	70.5	18.2	NR	NR	NR	NR	12.9	NR	NR	NR	NR	12.9	Thermal	Glove box	15
1.52	10.1	67.0	10.2	0.92	14.1	70.0	9.1	10.1	0.66	14.7	68.0	6.6	10.2	Thermal	Glove box	16
1.63	13.1	75.1	16.0	1.03	15.6	70.6	11.4	NR	NR	NR	NR	NR	NR	Thermal	Glove box	17
1.90	13.1	83.1	20.6	1.10	16.1	83.1	14.7	13.1	0.84	25.1	77.0	16.3	13.1	Thermal	Glove box	18
1.95	12.5	75.6	18.4	1.27	13.5	84.8	14.5	12.3	0.78	25.7	71.8	14.4	12.5	Thermal	Glove box	19
1.85	11.5	71.0	15.1	1.22	16.0	76.0	14.9	10.7	0.77	23.4	69.6	12.5	10.8	Thermal	Glove box	20
1.96	13.3	80.8	21.1	1.21	15.8	81.6	15.5	12.8	0.83	26.1	74.0	16.0	12.7	Thermal	NR	21
2.06	14.8	77.2	23.6	1.26	17.9	78.9	17.8	14.3	0.85	26.8	74.8	16.8	14.4	Thermal	Glove box	22
1.92	12.6	79.0	19.2	1.08	16.2	80.0	14.0	14.4	0.86	25.2	72.0	15.6	14.5	Thermal	Glove box	23
2.22	12.7	76.0	21.4	1.40	15.2	83.2	17.8	11.9	0.84	26.6	75.6	16.9	11.9	Thermal	Glove box	24
2.01	12.0	76.9	18.6	1.30	14.7	73.5	14.0	12.5	0.83	26.5	75.2	16.6	12.0	NR	NR	25
2.15	13.4	80.3	23.2	1.36	15.3	80.4	16.7	13.1	0.84	26.6	76.9	17.3	13.0	Thermal	Glove box	26
2.10	14.9	78.4	24.3	1.21	19.6	80.7	19.2	14.5	0.84	28.3	78.4	18.7	14.5	Thermal	Glove box	27
2.22	13.1	79.5	23.1	1.42	15.1	82.5	17.7	12.4	NR	NR	NR	NR	12.8	Thermal	Glove box	28
2.10	13.6	77.6	22.3	1.26	18.1	83.4	18.9	13.7	0.83	26.5	75.7	16.7	13.5	Thermal	Glove box	29
2.10	14.2	77.7	23.2	1.35	15.1	83.7	17.0	14.3	0.80	26.4	71.8	15.2	14.1	Thermal	Glove box	30
2.10	14.4	83.0	25.1	1.36	17.4	83.5	19.6	14.6	0.84	28.3	78.4	18.7	14.5	Thermal	Glove box	31
2.10	13.9	76.9	22.4	1.31	15.8	82.9	17.2	14.0	0.81	26.9	71.9	15.5	13.5	Thermal	NR	32
1.85	13.8	70.5	18.0	1.18	18.1	67.1	14.3	14.6	0.71	24.9	62.8	11.1	13.3	Thermal	Glove box	33
2.07	13.9	77.3	22.3	1.26	16.6	80.4	16.9	13.8	0.83	26.3	73.3	16.1	13.8	Thermal	Glove box	34
1.88	15.7	74.6	22.0	1.25	16.9	83.0	17.6	15.8	0.65	28.6	69.2	12.6	15.5	Thermal	Glove box	35

2.15	14.0	80.0	24.0	1.34	15.6	81.0	16.8	14.1	0.87	26.7	75.0	17.5	14.1	Thermal	Glove box	36
2.14	14.4	78.7	24.4	1.33	14.7	84.0	16.4	14.2	0.86	27.6	76.9	18.3	14.2	Thermal	Ambient	37
2.12	14.1	75.0	22.3	1.33	16.4	80.9	17.7	13.1	0.83	26.4	75.0	16.4	12.2	Thermal	Glove box	38
2.14	14.2	80.7	24.5	1.35	16.8	83.3	18.9	14.2	0.85	26.2	75.7	16.9	14.2	Thermal	Glove box	39
2.15	12.8	84.0	23.0	1.35	17.1	85.4	19.7	14.3	0.85	27.4	72.3	16.8	12.1	Thermal	Glove box	40
2.15	14.4	81.7	25.2	1.35	17.5	82.7	19.6	14.4	0.84	26.6	74.4	16.6	14.2	Thermal	Glove box	41
1.85	13.9	70.5	18.2	NR	NR	NR	NR	12.9	NR	NR	NR	NR	12.9	Thermal	Glove box	42
2.21	14.4	81.8	26.1	1.36	16.3	83.3	18.5	14.1	0.86	27.5	75.4	17.7	14.1	Thermal	Glove box	43
2.21	14.7	79.5	25.9	1.45	15.7	76.3	19.2	14.2	0.86	28.3	77.6	18.9	14.0	Thermal	Glove box	44
2.23	15.0	75.8	25.3	1.40	15.8	78.5	17.4	14.4	0.87	25.6	75.5	16.8	14.7	Thermal	Glove box	45
2.24	14.9	80.0	26.4	1.37	16.2	80.3	17.8	14.5	0.92	26.7	78.9	19.4	14.2	Thermal	NR	46
2.10	14.7	81.1	25.1	1.33	17.7	81.2	19.1	14.1	0.84	27.3	75.4	17.3	14.0	Thermal	Glove box	47
2.11	13.9	79.0	23.2	1.30	18.5	83.0	20.1	13.6	0.85	26.8	71.0	16.2	13.5	Thermal	Glove box	48
2.09	14.4	80.9	24.3	1.27	16.5	81.6	17.1	14.2	0.84	28.4	75.0	18.0	14.3	Thermal	Glove box	49
2.22	13.3	84.1	24.7	1.37	16.9	81.9	18.9	13.5	0.86	25.7	78.4	17.3	13.4	Thermal	Glove box	50
2.14	14.3	82.2	25.2	1.34	16.9	82.4	18.6	14.1	NR	NR	NR	NR	14.1	Thermal	Glove box	51
2.12	15.2	82.1	26.5	1.32	17.5	82.3	16.1	15.0	0.84	27.7	74.3	17.3	14.9	Thermal	Glove box	52
2.09	14.6	76.0	23.2	1.33	17.2	80.4	18.3	14.0	0.80	28.1	69.2	15.6	14.6	Thermal	Glove box	53
2.14	13.9	81.0	24.1	1.32	15.5	83.2	17.0	13.3	0.84	25.8	75.9	16.4	13.0	Thermal	NR	54
2.11	14.1	81.0	24.0	1.36	16.5	84.9	19.0	13.6	0.80	27.7	72.7	16.2	13.3	Thermal	Glove box	55
2.05	13.4	76.8	21.0	1.25	14.3	79.4	14.2	13.3	0.83	26.3	73.8	16.1	13.3	Thermal	Glove box	56
2.13	14.3	81.7	24.8	1.32	16.2	83.4	17.6	14.4	0.84	27.7	77.7	18.0	14.3	Thermal	Glove box	57
2.05	14.9	82.3	25.3	1.29	17.7	85.0	19.4	14.8	0.82	28.2	78.4	18.1	14.9	Thermal	Glove box	58
2.16	15.4	79.4	26.4	1.36	16.1	83.8	18.4	15.2	0.83	29.1	76.7	18.5	15.2	Thermal	Glove box	59
2.13	14.4	83.6	25.6	1.33	16.6	82.5	18.2	14.5	0.85	27.4	78.6	18.3	14.5	Thermal	Glove box	60
2.16	13.4	79.3	23.2	1.36	15.6	78.8	16.7	13.3	NR	NR	NR	15.9	13.3	Thermal	NR	61
2.10	**14.3**	**79.6**	**24.0**	**1.34**	**18.0**	**83.4**	**20.2**	**14.1**	**0.85**	**27.4**	**72.3**	**16.8**	**13.9**	**Laser**	**Ambient**	**This work**

5.2 Experimental methods

Materials

Materials and solvents used in this chapter are identical to those in Chapters 2 and 4 (see Sections 2.2 and 4.2). Cellulose acetate butyrate (CAB), potassium hexafluorophosphate (KPF_6) and cesium iodide (CsI) were purchased from Sigma-Aldrich. Pre-patterned ITO glasses with a sheet resistance of 8 Ω/sq were bought from Wuhan Jinge Solar Energy Technology Co. Ltd.

Laser annealing

Laser annealing conditions from Chapter 2 and laser processing parameters from Table 3.1 were also used in this chapter except the laser head motion in x- and y-direction for the PM6:Y6 OPV layer was at a speed of 304 mm/s. Different optimized laser power ratios (40%) and different optimal power (20.0 W) were used for the perovskite layer. Same optimized laser power ratio (35%) and optimal power (17.5 W) was used for MeO-2PACz:Me-4PACz. For the PM6:Y6 OPV layer, the optimized laser power ratio was and 20% and the optimal power was 10.0 W.

During laser processing optimisation for the PM6:Y6 OPV layer, low (L) laser pulse energy density at 0.08 J/cm^2 and high (H) laser pulse energy density at 0.30 J/cm^2 were also trialled. They corresponded to laser power ratio at 10% and laser power at 5 W for “L” or laser power ratio at 30% and laser power at 15 W for “H”.

Table 5.2 summarises the laser processing parameters including laser pulse energy density (J/cm^2) used.

Table 5.2. Optimized laser processing parameters used for perovskite, MeO-2PACz:Me-4PACz and PM6:Y6 OPV layers

	Perovskite	MeO-2PACz: Me-4PACz	PM6:Y6
Laser power (W)	20	17.5	10
Laser pulse energy density (J/cm^2)	0.36	0.31	0.15
Pulse repetition rate (Hz)		5000	6000
Scanning speed (mm/s)		254	304
Dwell time (ms)		9.4	7.9
Pulse-to-pulse distance (μm)		50.8	50.8
Time gap between two pulses (ms)		0.20	0.17

Device fabrication

Wide bandgap perovskite device:

Same ITO glass substrate cleaning process was carried out as Chapter 4.

Hole transport layer solution was prepared by mixing MeO-2PACz and Me-4PACz solutions in a volume ratio of 40%:60%. The two respective solutions were prepared by dissolving into a mixture solvent of methanol:dimethylformamide (DMF) (95:5 vol%), with a concentration of 0.5 mg/mL. The MeO-2PACz:Me-4PACz solution was deposited onto the ITO substrates by spin coating, at a spin rate of 4000 rpm for 16s. The film was then either annealed on a hot plate within a N_2 filled glove box (GTA) at 85 °C for 10 minutes or transferred out of glovebox for ambient laser annealing (ALA) – see details above.

Cellulose acetate butyrate (CAB) solution was prepared by dissolving in DMF with a concentration of 0.01 mg/mL and stirred with vortex mixer for at least 5 days before use. Wide bandgap perovskite (WBG) $FA_{0.8}Cs_{0.2}PbI_{1.8}Br_{1.2}$, with potassium hexafluorophosphate (KPF_6) and CAB additives, solution was prepared by mixing FAI (206.4 mg), CsI (77.9 mg), $PbBr_2$ (276.6 mg), PbI_2 (692 mg), KPF_6 (4.0 mg) in CAB-DMF (900 μL) : NMP (100 μL) binary solvent. The corresponding concentration was 1.5 M. WBG perovskite precursor solution was stirred with a vortex mixer at room temperature for 30 min before use. 80 μL of WBG perovskite precursor solution was spin-coated onto the Me-4PACz layer with an acceleration of rate of 400 rpm/s, and a spin rate of 4000 rpm for 50s. 15s into the spin coating, N_2 gas quenching (at a pressure of ~100 psi) was applied. The deposited WBG perovskite precursor film was then either annealed on a hot plate within a N_2 filled glove box (GTA) at 100 °C for 10 minutes or transferred out of glovebox for ambient laser annealing (ALA) – see details above.

LiF (1.0 nm), C_{60} (20 nm), BCP (6 nm) were then deposited sequentially on the annealed (GTA/ALA) perovskite film using a thermal evaporator. To complete cell fabrication as a single

junction, Cu (100 nm) is deposited via thermal evaporation using an evaporation mask. The active area of the cell was 0.0706 cm^2. For tandems, following steps were carried out.

OPV on perovskite for tandem:

After the fabrication of wide bandgap perovskite device, tin (IV) oxide (SnO_2) was deposited by thermal atomic layer deposition (ALD) in an Arradiance GEMStar reactor. Tetrakis(dimethylamino)tin(IV) (TDMASn) was used as the Sn precursor and was held at 60 °C in a stainless-steel container. Water was used as an oxidant and was delivered from a stainless-steel container at room temperature, the precursor delivery manifold's temperature was set to 115 °C. The TDMASn/purge1/H_2O/purge2 times were 1s/10s/0.2s/15s with corresponding nitrogen flows of 30sccm/90sccm/90sccm/90sccm to the deposition chamber at 80 °C. A 34 nm SnO_2 thin film was formed after 200 cycles.

0.5 nm (nominal, as read out by thickness monitor) Au was then deposited using thermal evaporation. A 10 nm molybdenum oxide (MoO_X) thin film was deposited on the pre-cleaned substrates via thermal evaporation.

To prepare the binary OPV precursor, PM6 and Y6 were mixed in a 1:1.5 mass ratio and added to 730 µL of chloroform (15 mg/mL) with the addition of 3.7 µL of 1-chloronaphthalene (CN) as an additive, and mechanically stirred overnight at room temperature inside the glovebox. The precursor solution was spin-coated on MoO_X coated substrate at a spin rate of 5000 rpm for 15 s. This was followed by an annealing step of 10 minutes at 100 °C temperature or laser annealing in ambient – see details above.

Afterwards, 20 nm C_{60} and 6 nm BCP were sequentially deposited via thermal evaporation. Finally, 100 nm Cu was thermally evaporated on the substrate using an evaporation mask. The active area of the cell was 0.0706 cm^2. The single junction OPVs were fabricated using the same processes but deposited on ITO-glass substrates.

For encapsulating solar cells for thermal stability tests (60 °C in N_2 filled glove box), the poly-isobutylene (PIB) based polymer "blanket" approach[62,63] was used. After tandem cell fabrication completion, the edge of the cell was cleaned mechanically. The PIB based polymer was then applied to the entire device with a cover glass, except for ITO area acting as feedthrough for positive and negative contacts. After PIB application, the sample was pressed for 30 minutes.

Device and film characterizations

Same equipment from Chapters 2 and 4 was used for current density-voltage (*J-V*)

measurements. Conditions were similar except the scanned voltage ranges were -0.1 – 1.4 V, -0.1 – 1.0 V and -0.1 – 2.2 V for single junction perovskite, organic and tandem solar cells, respectively.

Same methods from Chapters 2 and/or 4 were used for steady-state power output, and light intensity-dependent V_{OC} measurements; determination of the activation energy of recombination current E_a; scanning electron microscopy (SEM); Atomic force microscopy (AFM), X-ray diffraction (XRD) measurements; steady-state and time-resolved photoluminescence measurements; determination of carrier lifetimes; and X-ray photoelectron spectra (XPS) and depth-resolved XPS measurements.

While same methods from Chapters 2 and/or 4 were used for external quantum efficiency (EQE) measurements, bias illumination from very bright LEDs with emission peaks of 850 and 460 nm were used for the wide bandgap perovskite and narrow bandgap OPV subcells, respectively, for the EQE measurement of perovskite-OPV tandem solar cells.

Test structures of perovskite/MeO-2PACz:Me-4PACz/ITO/glass were used for SEM, XRD, optical absorption and photoluminescence measurements and AFM. Same type of annealing (GTA or ALA) was used for both the perovskite and MeO-2PACz:Me-4PACz layers.

Attenuated total reflectance Fourier transform infrared (ATR-FTIR) spectroscopy was carried out by a Bruker Alpha portable spectrometer using a Platinum ATR single reflection module.

The temperature-dependent open-circuit voltage measurements were performed in a helium atmosphere, using a cryogen-free cryostat (Cryogenics Ltd) and a model 350 temperature controller (Lakeshore). The white light source was provided by an OSL2 fibre-coupled illuminator (Thorlabs). The open-circuit voltage was measured using a B2901A precision source/measure unit (Keysight). The voltage values were recorded at each temperature after the value stabilized (~10-15 mins).

Depth resolved grazing incident X-ray diffraction (GIXRD) measurements were carried out using the Panalytical Empyrean system equipped with iCore, dCore, and a 1Der detectors. Settings used were 45 kV/40 mA for a scan range of 8 - 40° (2θ), and a step size of 0.033° for sample size ~15 mm square. There were 3 scans per sample. The first was a normal θ–2θ scan (Bragg-Brentano geometry), for an X-ray penetrate depth of ~500 nm. The second scan had a grazing incidence geometry of ω = 0.5°, where X-ray penetration was about 290 nm (calculated). For the third scan, the ω angle was 0.3°, for a penetration depth of about 170 nm (calculated). The data was processed with HighScore Plus software. Peak profile fitting was

performed, and FWHM was measured. The phase identification was carried out on the first scans.

Transient photocurrent (TPC) was measured using a Keysight MSO9254A oscilloscope. The 520 nm wavelength excitation light was provided by a Thorlabs NPL52B pulsed laser with a 5 ns pulse width, repetition rate of 1 MHz, and pulse energy of 1.2 nJ. The diameter of the beam was approximately 2 mm.

Temperature profiling simulation

Same method as that in Chapter 3.

5.3 Results and discussions

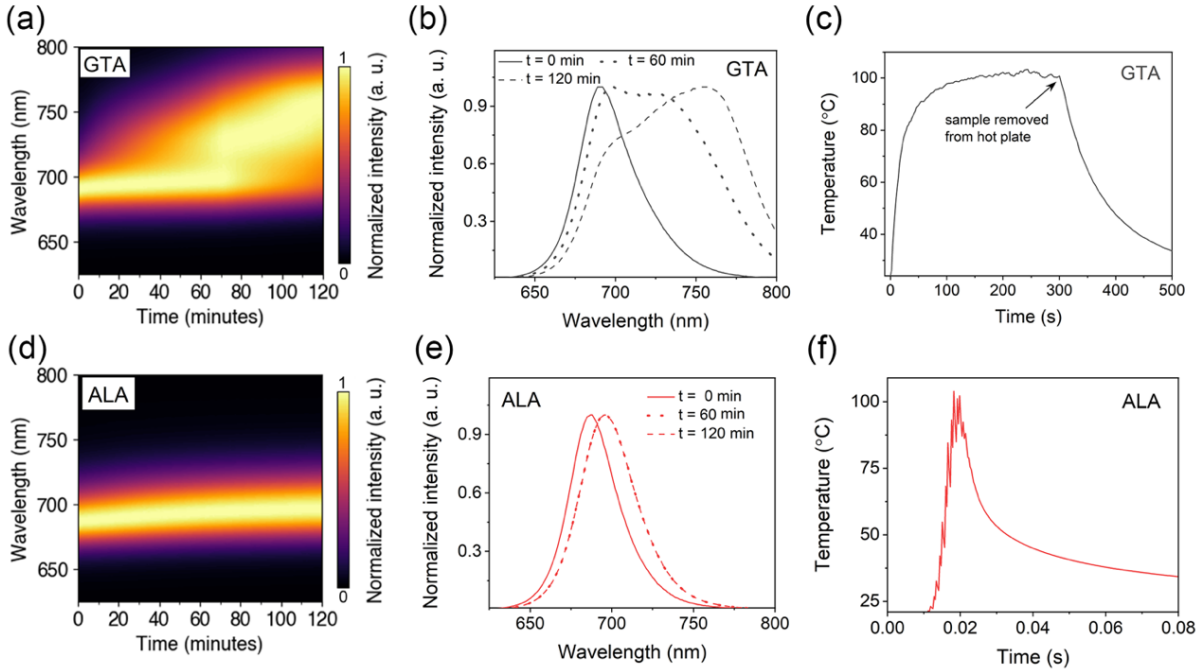

Figure 5.1 Evolution of normalised photoluminescence (PL) spectra during 120 minutes of continuous measurement for (a) glovebox thermal annealed (GTA), (d) ambient laser annealing (ALA) perovskite/MeO-2PACz:Me-4PACz/ITO/glass test structures. (b, e) Snapshots of the same PL spectra at t = 0 (solid), 60 (dotted), and 120 (dash) minutes. (c) Temperature profile measured at the perovskite surface during thermal annealing. (f) Temperature profile simulated for perovskite surface during laser annealing.

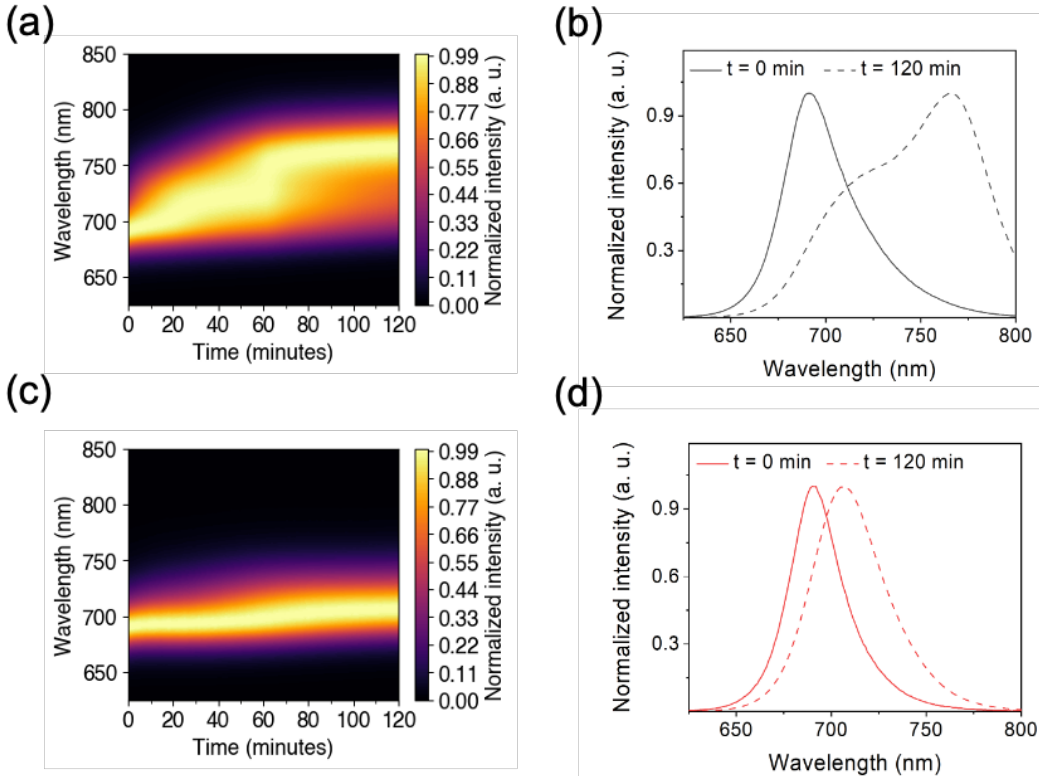

Figure 5.2 Evolution of normalized photoluminescence (PL) spectra during 120 minutes of continuous measurement for (a) glovebox thermal annealed (GTA), (c) ambient laser annealing (ALA) perovskite/MeO-2PACz:Me-4PACz/ITO/glass test structures without the use additives. (b, d) Snapshots of the same PL spectra at t = 0 (solid), and 120 (dash) minutes.

To study the phase stability of the ambient laser annealed (ALA) wide bandgap 1.78 eV perovskite films, test structure of perovskite/MeO-2PACz:Me-4PACz/ITO/glass was fabricated whereby both the MeO-2PACz:Me-4PACz hole transport layer (HTL) and the perovskite layer (with or without the use of additives (see wide bandgap perovskite device fabrication details in the Supporting Information) were annealed by laser.

Steady-state photoluminescence (PL) measurement was then carried out over time. Measurement on perovskite/MeO-2PACz:Me-4PACz/ITO/glass test structure annealed by conventional hot-plate (thermal) annealing inside a glovebox (GTA) was also carried out for comparison. For comparison between ambient laser annealed (ALA) and ambient hot-plate (thermal) annealing (ATA) films and devices, see Chapter 2.

Results in **Figures 5.1a & b** and **5.2** show significant emission broadening and the emergence of longer-wavelength peak during PL measurement in the GTA perovskite film suggesting light-induced phase segregation. This is not the case for ALA perovskite film whereby only red-shift was observed after 60 minutes of measurement and without further shifting afterwards indicating suppressed phase segregation (**Figures 5.1d & e**). Suppressed segregation is also

observed in perovskite film without additives (**Figure 5.2**).

According to measured and simulated temperature profiles for the GTA and ALA perovskite films, shown in **Figures 5.1c** & **f**, respectively, both GTA and ALA films experienced similar peak temperatures at ~100 °C. However, the ALA film experienced much more rapid heating and cooling rates, averaged at 30220 °C/s and -29473 °C/s, respectively, compared to 4 °C/s and -1 °C/s for the GTA film.

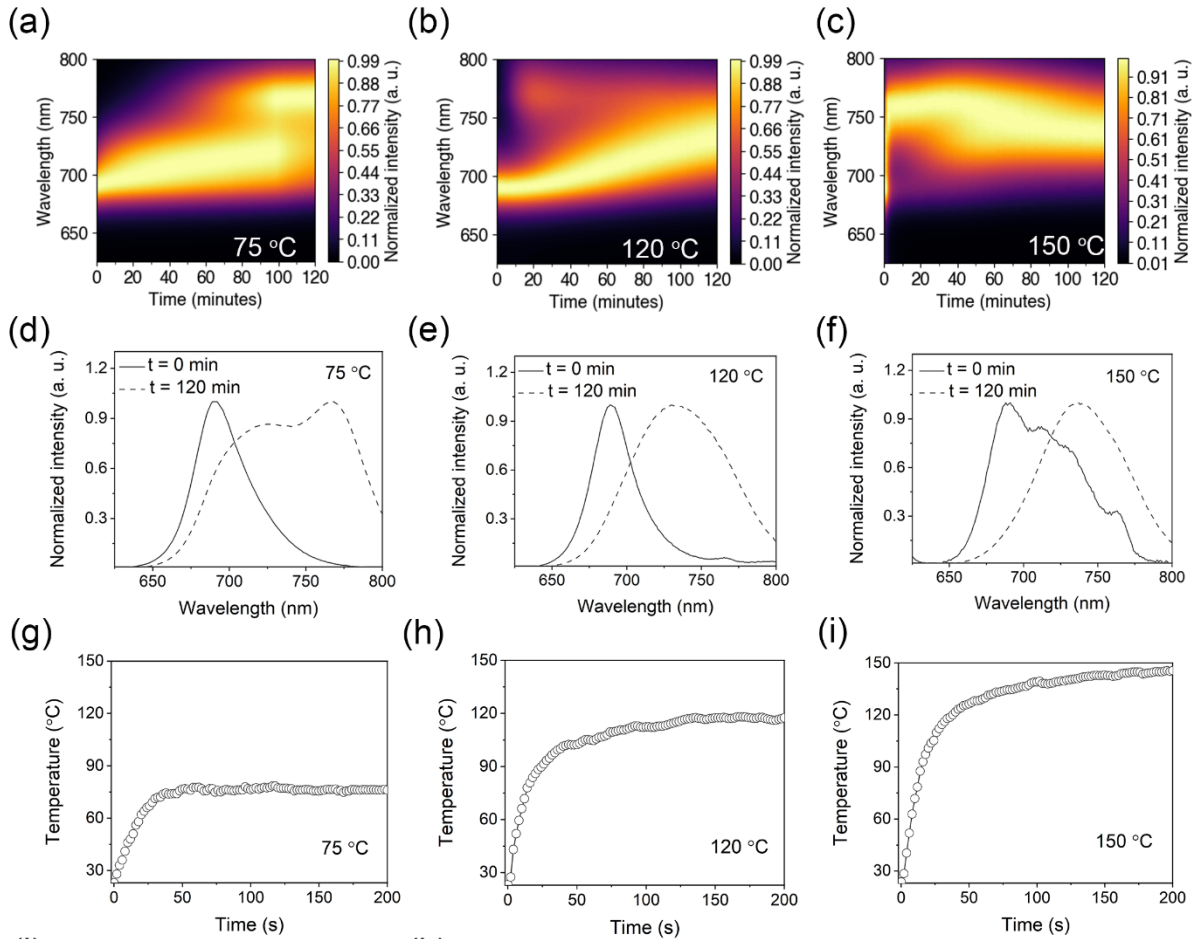

Figure 5.3 Evolution of normalised photoluminescence (PL) spectra during 120 minutes of continuous measurement for perovskite/MeO-2PACz:Me-4PACz/ITO/glass test structures by GTA at (a) 75 °C; (b) 120 °C; (c) 150 °C for the perovskite film. (d-f) Snapshots of the same PL spectra measured at t = 0 (solid) and 120 min (dashed). (g-i) Temperature profiles measured at the perovskite surface during thermal annealing of the same films.

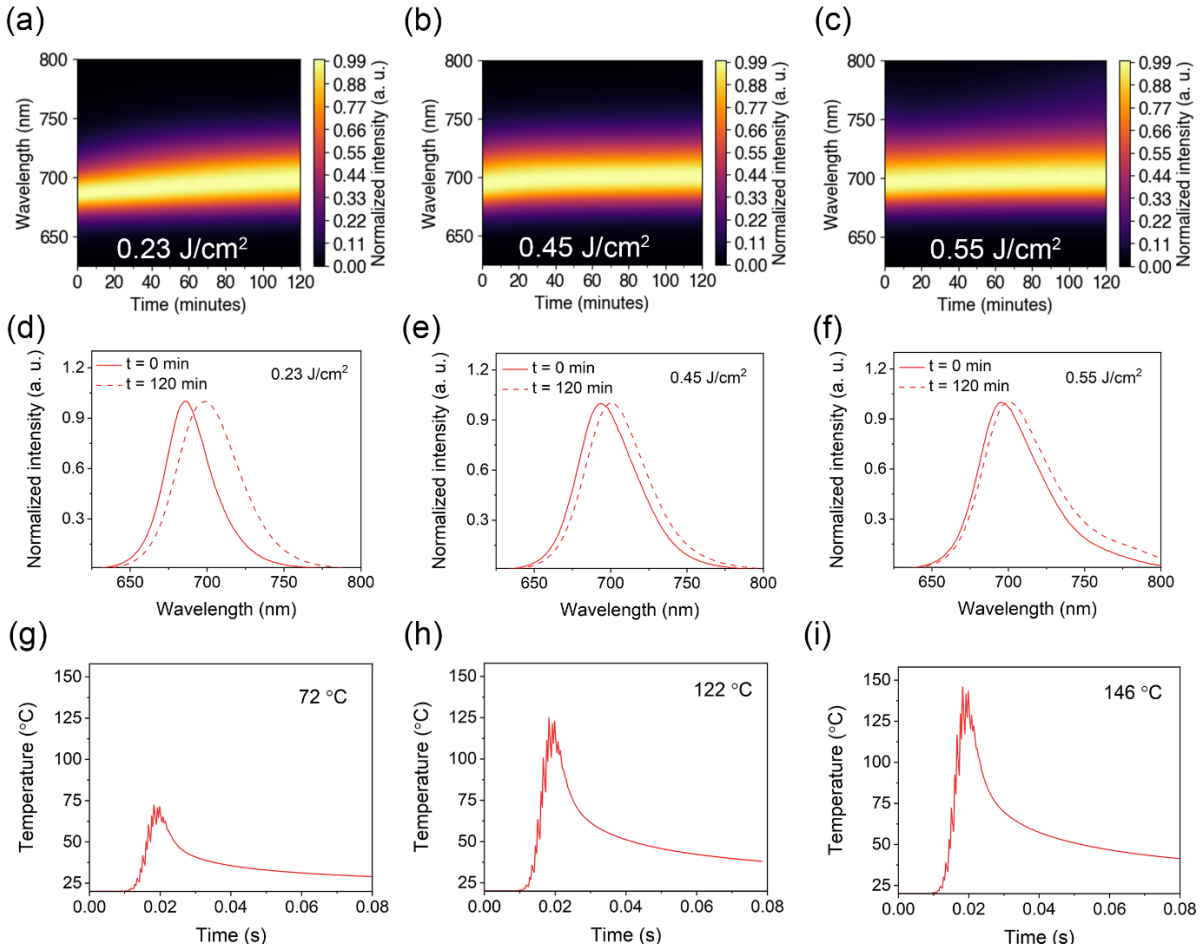

Figure 5.4 Evolution of normalised PL spectra for during 120 minutes of continuous measurement for perovskite/MeO-2PACz:Me-4PACz/ITO/glass test structures by ALA at laser pulse energy densities of (a) 0.23 J/cm^2 (laser power ratio = 25% and laser power = 12.5 W); (b) 0.45 J/cm^2 (laser power ratio = 50% and laser power = 25W); (c) 0.55 J/cm^2 (laser power ratio = 60% and laser power = 30W) for the perovskite film. (d-f) Snapshots of the same PL spectra measured at t=0 (solid) and 120 min (dashed). (g-i) Temperature profiles simulated for perovskite surface during laser annealing.

Results from further experiments showed that rapid heating and cooling contributes to perovskite phase stability as shown in **Figures 5.3 & 5.4**. All GTA perovskite films whether annealed at temperatures 75, 120 or 150 °C showed PL broadening (**Figure 5.3a-f**) during measurement due to light-induced phase segregation. All these films experienced slow heating rate of less than 6 °C/s and even slow rate of cooling (**Figure 5.3g-i**). ALA perovskite films were also fabricated at three different laser pulse energy densities reaching similar peak temperatures (72, 122 and 146 °C). No significant broadening nor secondary PL peak was observed during two hours of measurement (**Figure 5.4a-f**) except for peak-red-shifts observed especially in the ALA film processed at low laser pulse energy (**Figure 5.4d**). All the ALA films experienced heating and cooling over a much shorter period of time – tens of milliseconds

(**Figure 5.4g-i**) as opposed to hundreds of seconds (**Figure 5.3g-i**) for the GTA films. Therefore, the 5 orders of magnitude higher heating and cooling rates experienced by the ALA films compared to the GTA films is the major contributor to phase stability rather than the annealing temperature being the contributor. Similarly, ion migration reduction in mixed halide perovskite by laser annealing has been recently reported by Song et al.[64] who attributed the ion migration reduction to enhanced interaction among the inter-ionic forces in the inorganic framework and the optimization of crystallization kinetics resulting from the ultrafast shock pressure and rapid heating/cooling thermal effect from laser annealing.

Apart from better phase stability, ALA perovskite films, compared to GTA films, also produced larger grains (**Figure 5.5**), stronger preference to the (100) crystalline phase (**Figure 5.6b-d**) and fewer PbI_2 residues at the surface or within the bulk (**Figure 5.6a & 5.7**), enhanced light absorption (**Figure 5.8a**), and significantly higher steady-state photoluminescence (**Figure 5.8b**) and carrier lifetimes (**Table 5.3** & **Figure 5.8c**).

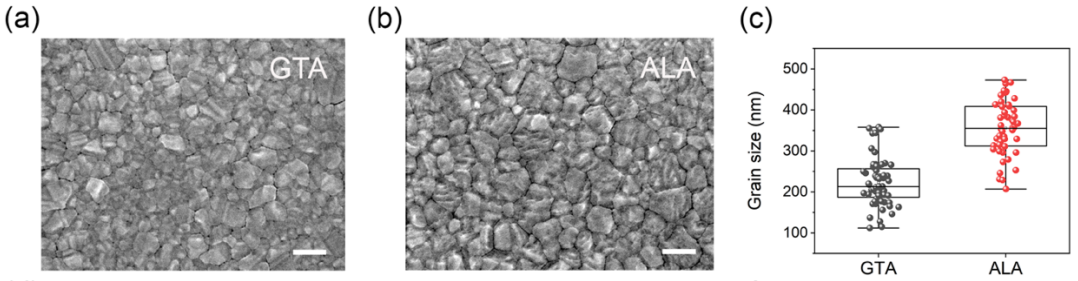

Figure 5.5 Scanning electron microscopy (SEM) images of (a) GTA- and (b) ALA-films. (c) Grain size distributions for films in (a) and (b). Scale bar = 400 nm.

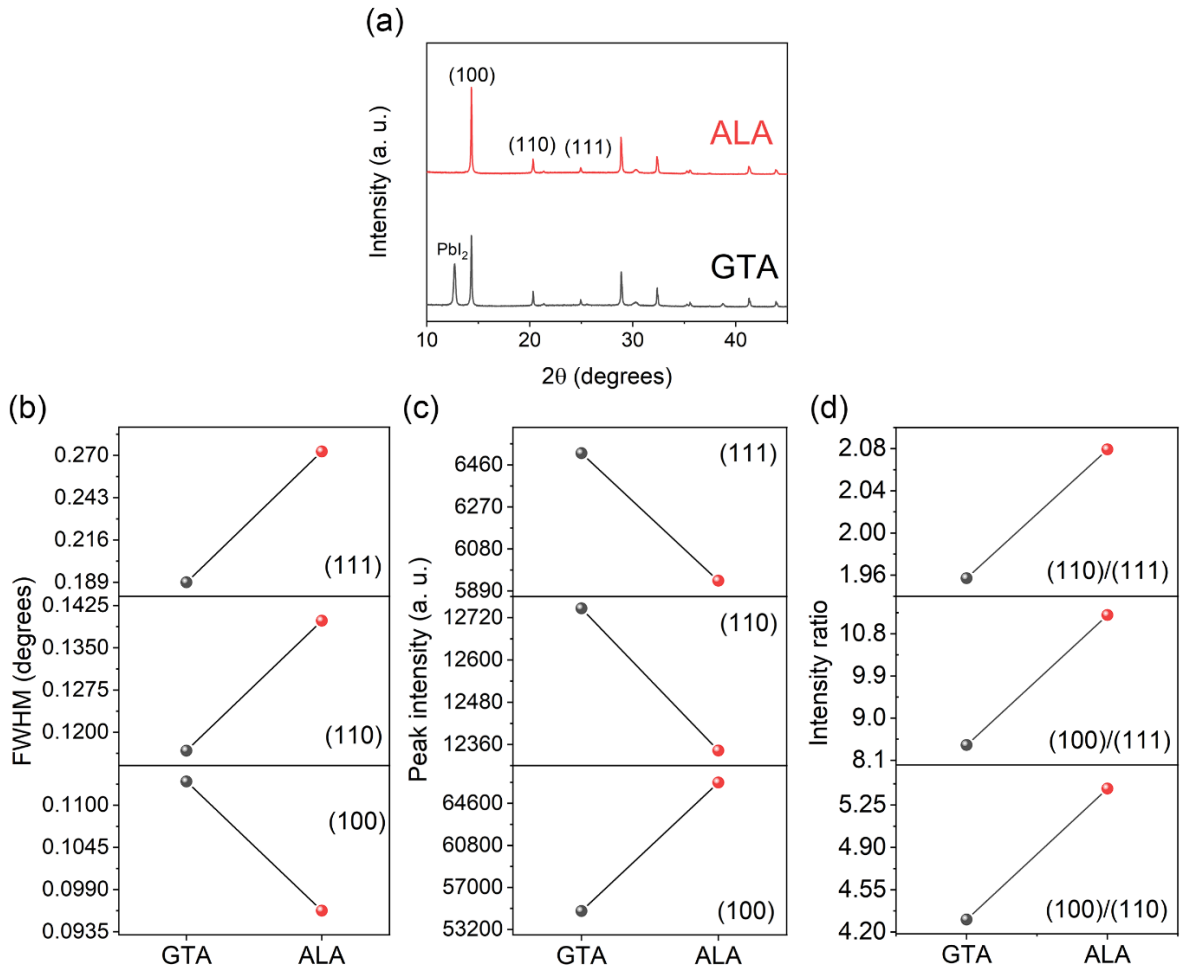

Figure 5.6 (a) X-ray diffraction (XRD) patterns of GTA- and ALA-films. (b) Full width at half-maxima (FWHM) and (c) peak intensities of the perovskite (111) (top), (110) (middle), (100) (bottom) diffraction peaks from (a). (d) Intensity ratios of (110)/(111), (100)/(111), and (100)/(110).

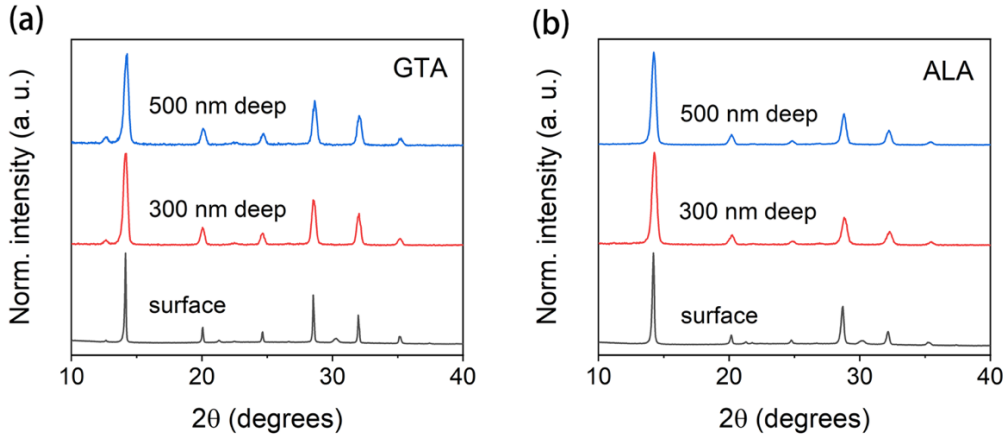

Figure 5.7 Depth resolved grazing incident X-ray diffraction (GIXRD) patterns of (a) GTA and (b) ALA perovskite films.

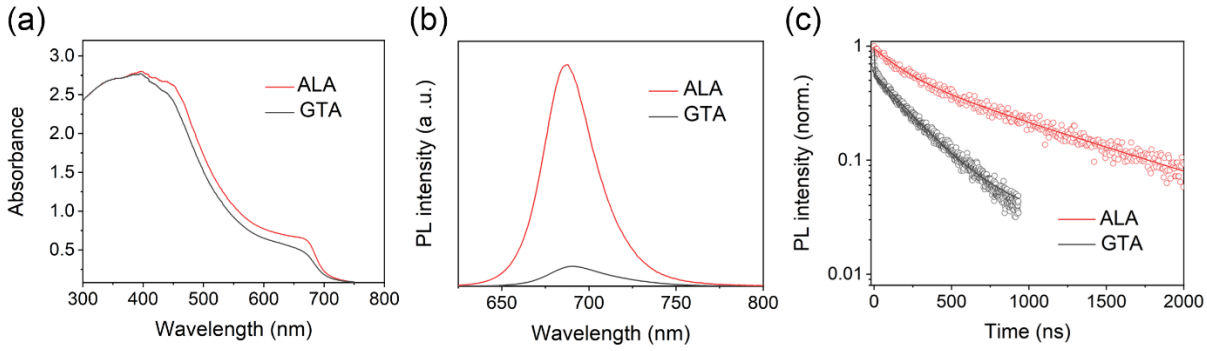

Figure 5.8 (a) UV-Vis absorbance spectra, (b) steady photoluminescence (PL) and (c) time resolved PL of GTA- and ALA-films.

Table 5.3 Fitted lifetimes from measured time-resolved photoluminescence (TrPL) of GTA and ALA perovskite films from **Figure 5.8c**.

Annealing	τ_1 (ns)	A_1 (%)	τ_2 (ns)	A_2 (%)	Effective lifetime (ns)
GTA	3.4	39	272.0	55	269.7
ALA	130.5	38	688.8	57	625.8

These enhanced material properties in ALA perovskites explain the more superior performance in the associated wide bandgap 1.78 eV photovoltaic devices (**Figure 5.9, Table 5.4 and Figure 5.10**) compared to the GTA devices. Enhanced light absorption in ALA perovskites contributed to higher J_{SC} (**Figure 5.9d**). Enhancing photoluminescence and carrier lifetimes observed in ALA films correlate with higher V_{OC} (**Figure 5.9e**) and FF (**Figure 5.9f**) in ALA devices. This is due to improved carrier transport (**Figure 5.11**) and the reduction of trap-related carrier recombination in the ALA devices as shown by reduction in the ideality factor (n_{id}) to 1.16 in a representative ALA device compared to n_{id}=1.36 for a representative GTA device, determined from their light intensity-dependent V_{OC} plots (**Figure 5.9h**).

It is important to note that device performance improvement does not only come from the improvement in the bulk, but also from improvement at perovskite/HTL interface as laser annealing was used for both perovskite layer and the HTL. This is evident from the results of temperature-dependent V_{OC} measurements (**Figure 5.9i**), the recombination current activation energy (E_a) increased from 1.75 eV for the GTA device to 1.89 eV for ALA device indicating that recombination mechanism in the GTA cell is more surface-dominated while for the ALA cell, it is more bulk-dominated due to the improvement of the ALA perovskite surfaces. The first surface improvement comes from improved perovskite/HTL interface as laser annealing was used for both the perovskite layer and HTL in ALA devices. **Figure 5.12** shows improved contact angle of perovskite precursor solution on an ALA HTL film compared to a GTA HTL.

The second surface improvement in ALA devices comes from smoother top perovskite surface compared to a GTA perovskite surface (**Figure 5.13**).

The advantage of ALA over GTA diminishes when ambient relativity humidity ⩾ 70% resulting in reduction and large spread for all electrical parameters (**Figure 5.14**).

Table 5.4 Summary of average and champion GTA and ALA wide bandgap 1.78 eV perovskite device performances. ALA devices were processed under relativity humidity of 30 to 40%.

Annealing	Avg. / Best	J_{SC} (mA cm^{-2})	V_{OC} (V)	FF (%)	PCE (%)
GTA	Average	17.5±0.1	1.29±0.01	81.0±0.4	18.4±0.4
	Champion	17.7	1.30	81.7	18.8
ALA	Average	17.9±0.2	1.34±0.01	81.9±1.2	19.6±0.4
	Champion	18.0	1.34	83.4	20.2

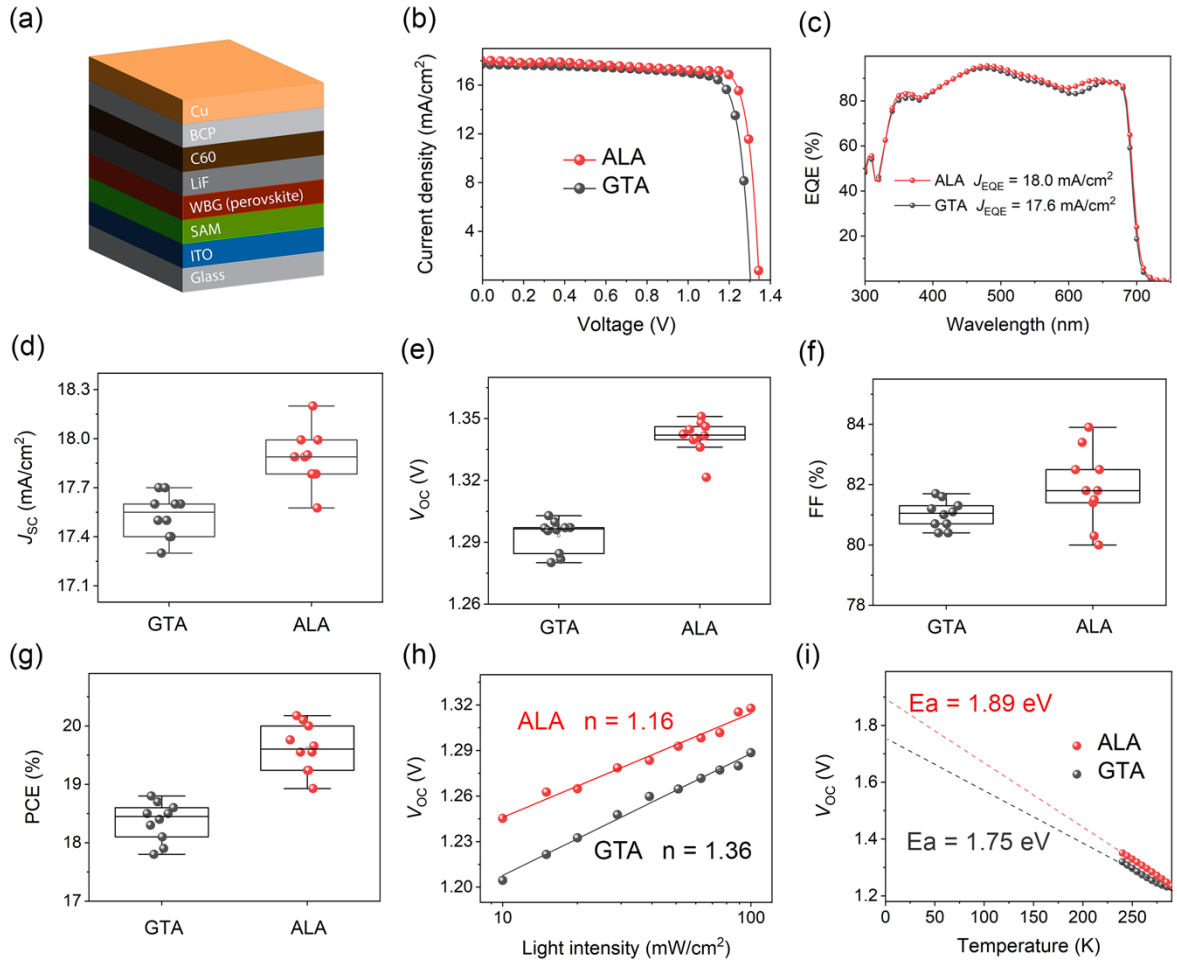

Figure 5.9 (a) Schematic of wide bandgap 1.78 eV perovskite devices demonstrated. (b) Light current density-voltage (*J-V*) and (c) external quantum efficiency (EQE) plots of the champion GTA and ALA devices. ALA devices were processed under relativity humidity of 30 to 40%. Distributions of (d) short-circuit current density (J_{SC}), (e) open-circuit voltage (V_{OC}), (f) fill factor (FF), and (g) power conversion efficiency (PCE) for GTA and ALA devices. (h) Light-

dependent and (i) temperature-dependent V_{OC} of representative GTA and ALA devices.

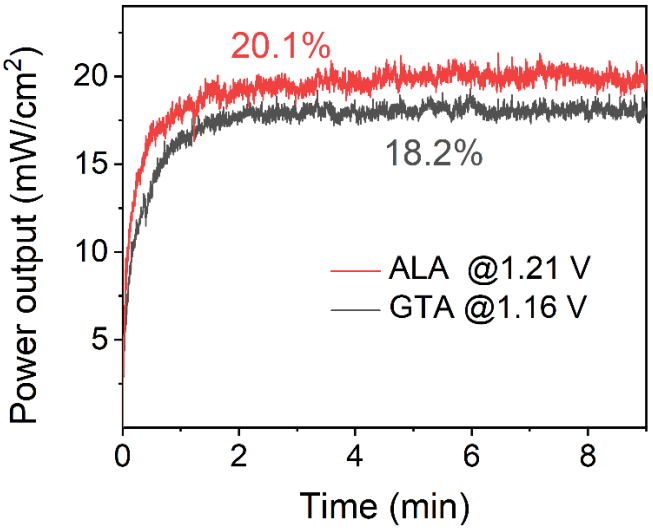

Figure 5.10 Steady-state output power of representative GTA (black) and ALA (red) wide bandgap 1.78 eV perovskite devices.

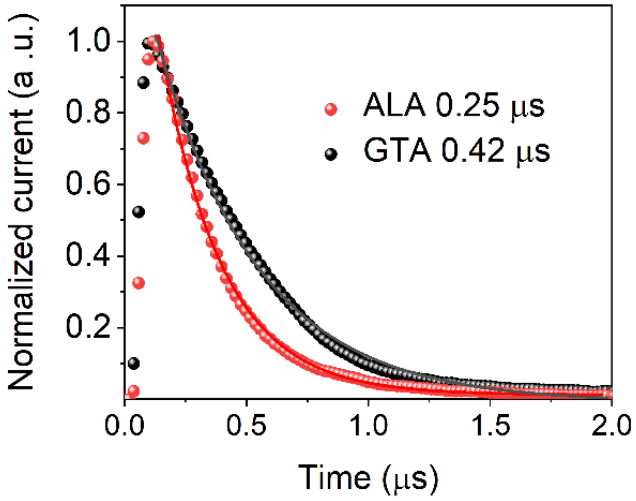

Figure 5.11 Transient photocurrents (TPC) of representative GTA (black) and ALA (red) wide bandgap 1.78 eV perovskite devices. Also shown are calculated carrier extraction times.

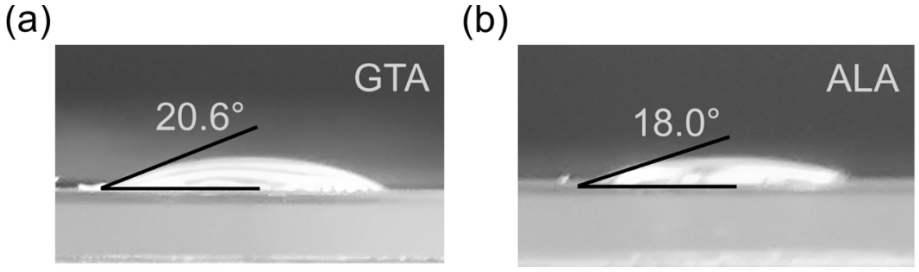

Figure 5.12 Contact angles of perovskite precursor solution on (a) GTA and (b) ALA HTL.

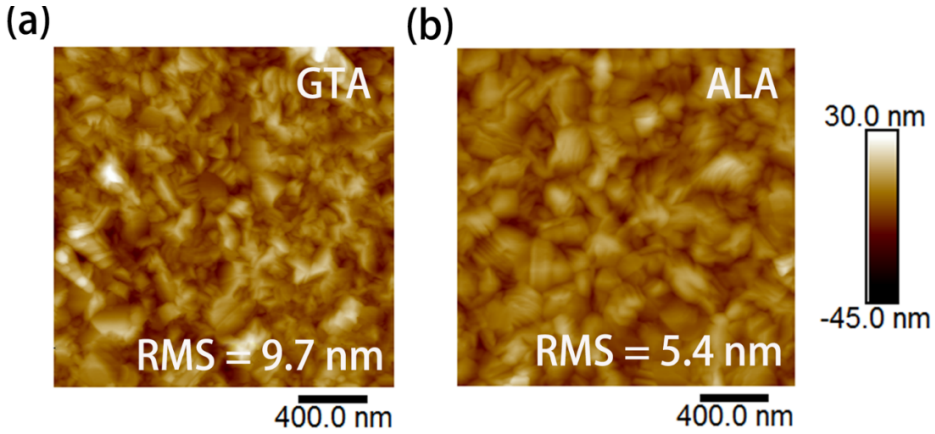

Figure 5.13 Atomic force microscopy (AFM) images of (a) GTA and (b) ALA perovskite films.

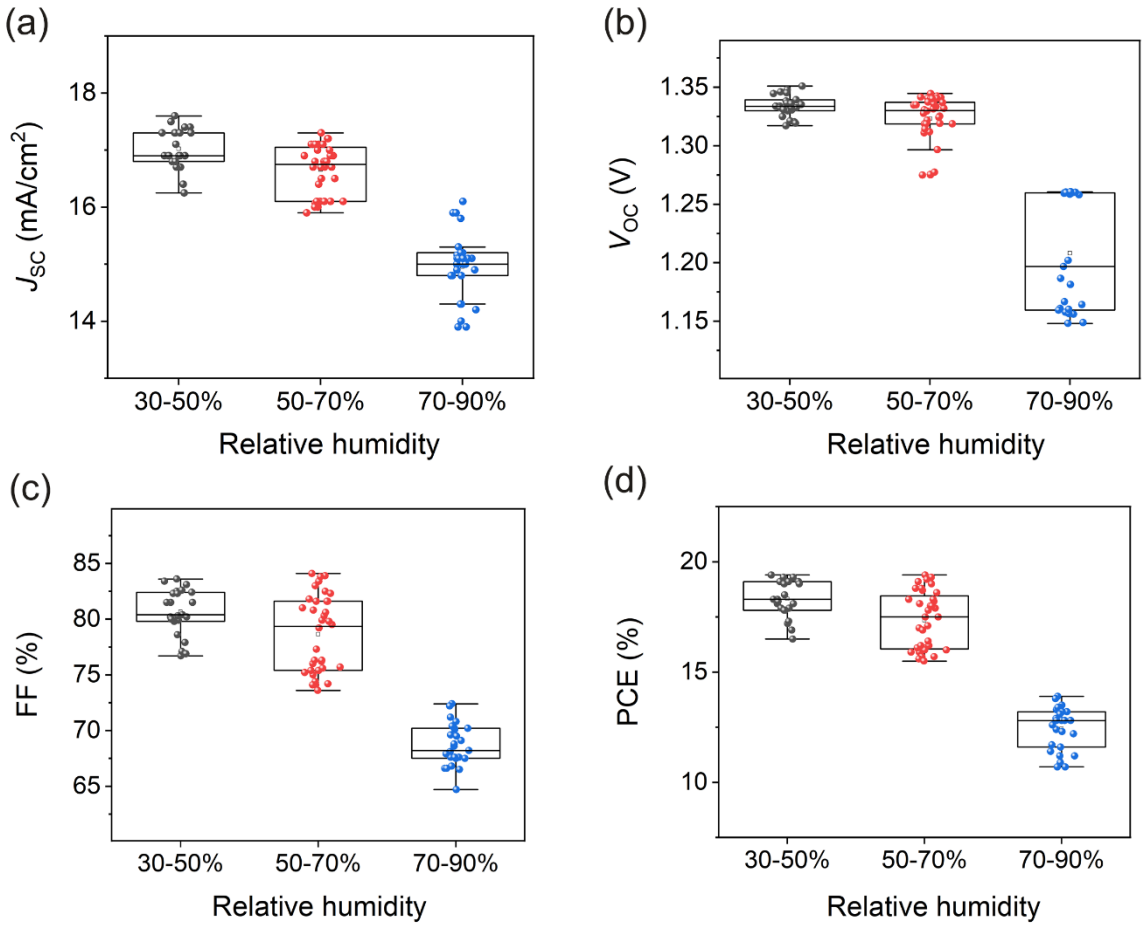

Figure 5.14 Distributions of (a) short-circuit current density (J_{SC}), (b) open-circuit voltage (V_{OC}), (c) fill factor (FF), and (d) power conversion efficiency (PCE) for ALA wide bandgap 1.78 eV perovskite devices as a function of ambient relative humidity.

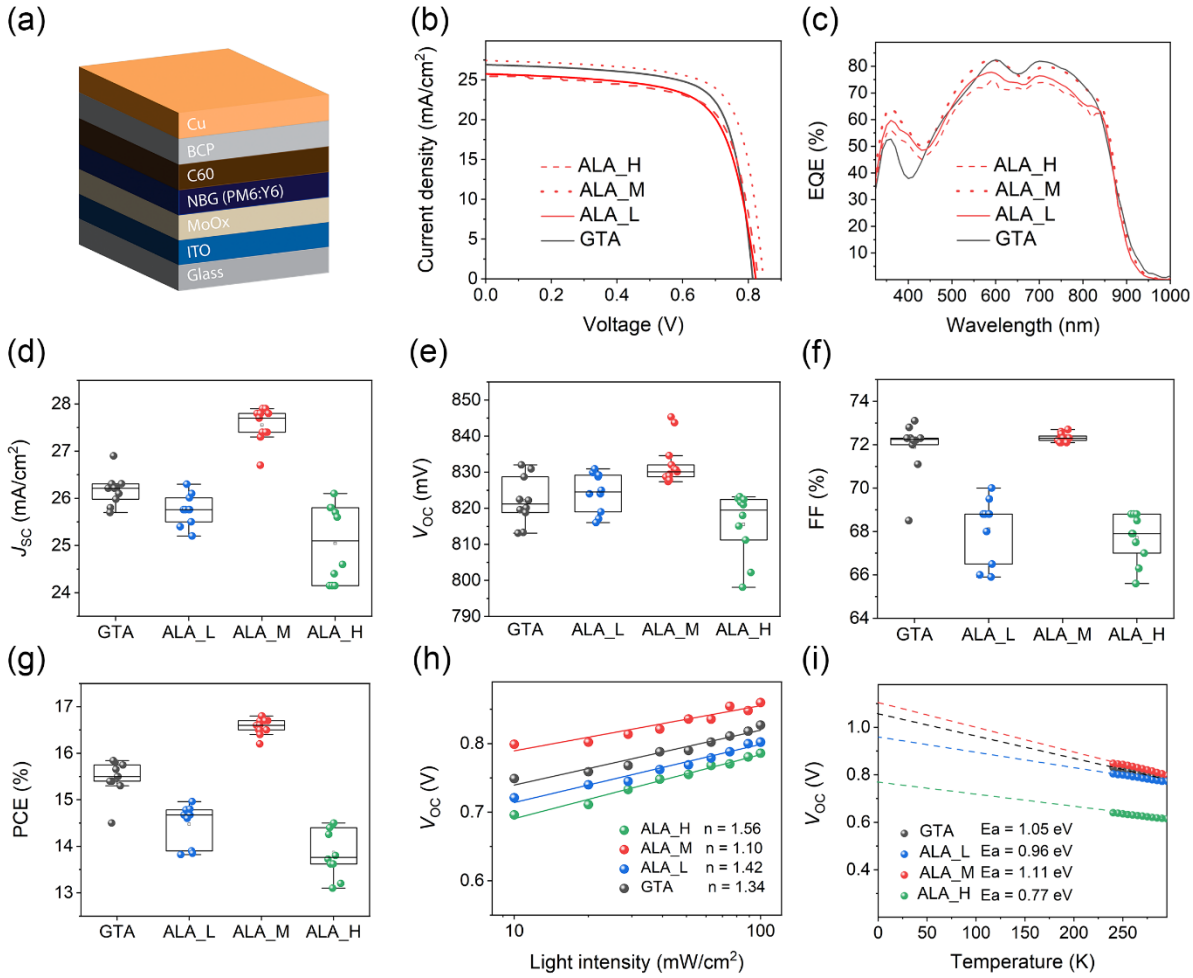

Figure 5.15 (a) Schematic of PM6:Y6 organic photovoltaic (OPV) perovskite devices demonstrated. (b) Light current density-voltage (*J-V*) and (c) external quantum efficiency (EQE) plots of the champion or representative GTA OPV devices and same device by ALA at lower, medium and high laser pulse densities. Distribution of (a) J_{SC}, (b) V_{OC}, (c) FF, and (d) PCE of GTA and ALA OPV devices annealed at 3 different laser pulse densities. (h) Light- and (i) temperature-dependent V_{OC} of representative GTA and ALA devices.

Capitalizing on the advantages of laser annealing, especially the low photon energy of CO_2 laser beam that enables annealing without substantial damage to chemical bonds, laser annealing was developed for OPV solar cells based on PM6:Y6 (**Figure 5.15**) trialling three laser energy densities at 0.08 J/cm^2 (denoted as ALA_L), 0.15 J/cm^2, (denoted as ALA_M) and 0.30 J/cm^2 (denoted as ALA_H). Details of laser power ratios and laser power settings for these three conditions can be found in Section 5.2.

Figure 5.16 shows the Fourier transform infrared (FTIR) spectroscopy for GTA and ALA PM6:Y6 films on top of wide bandgap perovskite cells. It can be seen that no chemical bonding changes can be observed even at high laser energy density demonstrating the advantage of low photon energy of CO_2 laser for annealing.

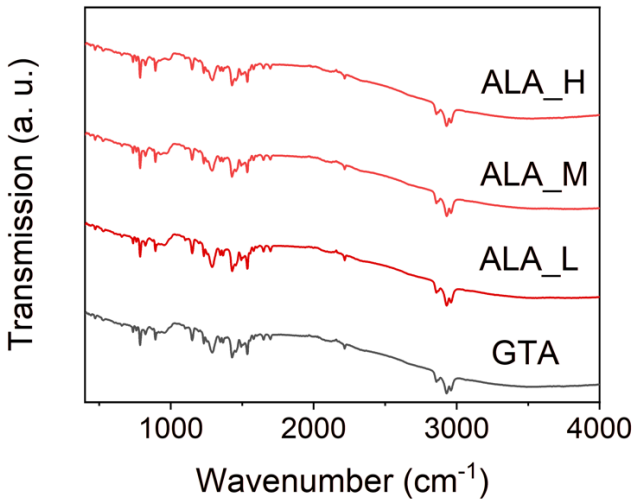

Figure 5.16 ATR-FTIR spectroscopy for GTA (black) and ALA (red) PM6:Y6 films on top of wide bandgap perovskite cells. 3 different laser energy densities at 0.08 J/cm^2 (ALA_L, solid), 0.15 J/cm^2, (ALA_M, dotted) and 0.30 J/cm^2 (ALA_H, dash) were used.

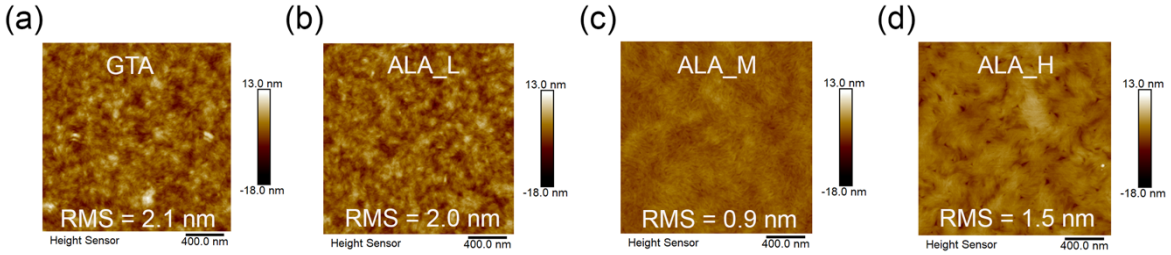

Figure 5.17 AFM images of PM6:Y6 films on top of ITO glass by (a) GTA and ALA at laser energy density at (b) 0.08 J/cm^2 (ALA_L), (c) 0.15 J/cm^2, (ALA_M) and (d) 0.30 J/cm^2 (ALA_H).

The morphologies of the same GTA and ALA PM6:Y6 films observed under atomic force microscope (AFM) are shown in **Figure 5.17**. ALA PM6:Y6 film processed at the optimal laser energy density (with a root-mean-square (RMS) roughness of 0.9 nm, **Figure 5.17c**) is smoother than the GTA film with an RMS roughness = 2.1 nm, **Figure 5.17a**). In addition, the optimum film exhibits more uniform and homogeneous surface that could be attributed to the CO_2 laser polishing or smoothing effect on material surfaces.[65-67] Lower or higher laser energy densities resulted in rougher films (**Figure 5.17b&d**). The former is due to insufficient energy for film smoothening. The latter is due to the formation of pinholes under high irradiation density.

With regards to opto-electronic properties, **Figure 5.18** shows that ALA films annealed with the optimum laser energy density exhibits the lowest steady-state photoluminescence suggesting better exciton dissociation, important for OPV device performance.[68, 69]

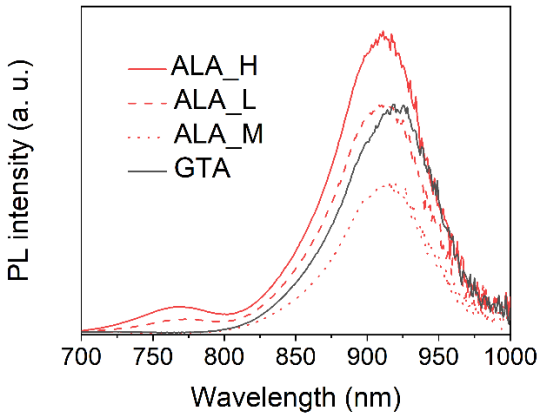

Figure 5.18 Steady-state PL spectra of PM6:Y6 films on top of MoOx/ITO/glass: GTA (black) and ALA (red) at laser energy density at 0.08 J/cm^2 (ALA_L, solid line), 0.15 J/cm^2, (ALA_M, dotted line) and 0.30 J/cm^2 (ALA_H, dash line).

Table 5.5 Summary of GTA PM6:Y6 OPV device and same devices by ALA performances at lower, medium and high laser pulse densities.

Annealing	Avg. / Best	J_{SC} (mA cm^{-2})	V_{OC} (V)	FF (%)	PCE (%)
GTA	Average	26.1±0.3	0.82 ±0.01	71.9±1.3	15.5±0.4
	Champion	26.3	0.83	72.3	15.8
ALA_L	Average	25.8±0.3	0.82±0.01	68.1±1.5	14.5±0.4
	Champion	25.8	0.83	68.8	14.8
ALA-M	Average	27.6±0.3	0.83±0.01	72.3±0.2	16.6±0.2
	Champion	27.4	0.85	72.3	16.8
ALA_H	Average	25.1±0.9	0.82±9.1	68.3±0.5	14.1±0.4
	Champion	25.7	0.82	68.5	14.5

For device demonstrations, control devices annealed by a hot-plate in a N_2-filled glove box (GTA) were also fabricated for comparison. Device results are shown in **Figure 5.15** and **Table 5.5** which agree with trends observed from PM6:Y6 film properties observed above as a function of laser energy density. The highest J_{SC} (**Figure 5.15**) was obtained when medium laser energy density was used when the ALA PM6:Y6 is smoothest, that contributed to improved FF, more so than V_{OC}.

The improved FF is likely to be due to the PM6:Y6/C_{60} interface formed on smoother PM6:Y6 film. Clues can be found from the light-dependent V_{OC} measurements (**Figure 5.15i**). The ALA PM6:Y6 device with optimum laser energy density produced the highest E_a (1.11 eV) compared to those of the GTA PM6:Y6 devices and ALA PM6:Y6 devices indicating their carrier recombination are more surface dominated.

When higher or lower laser energy densities were used, devices produced sub-optimal values across all electrical characteristics (**Figures 5.15 d-g**) due to reduced film homogeneity (e.g., rougher surfaces).

Results from light-intensity dependent V_{OC} (**Figure 5.15h**) followed the same trend as J_{SC}, FF and therefore PCE indicating reduced of trap-related carrier recombination (from laser annealing especially at optimum laser energy intensity) played a major role in these improvements.

A champion PCE of 16.8% was obtained for the first ambient-laser annealed PM6:Y6 OPV cell reported and the PCE is highest for all laser annealed PM6:Y6 OPV cell reported (**Figure 5.19** & **Table 5.6**).

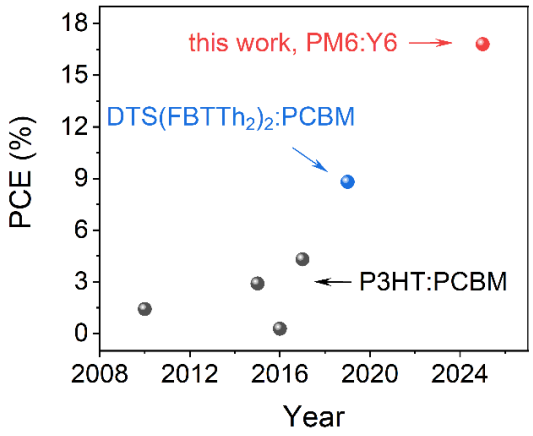

Figure 5.19 Plot of power conversion efficiencies (PCEs) of laser-annealed organic photovoltaic cells reported[10,11,70-72] compared to our work.

Table 5.6 Cell parameters of reported laser-annealed organic photovoltaic (OPV) cells from **Figure 5.19** compared to our work.

Year	OPV	Laser	J_{SC} (mA/cm^2)	V_{OC} (V)	FF (%)	PCE (%)	Ref.
2010	P3HT:PCBM	Fibre	7.2	0.63	35.5	1.4	10
2015	P3HT:PCBM	Ti:Sapphire	8.7	0.61	54.8	2.9	11
2016	P3HT:PCBM	Nd:YAG	2.2	0.56	22.0	0.3	19
2017	P3HT:PCBM	Ti:Sapphire	10.6	0.62	65.5	4.3	20
2019	DTS(FBTTh$_2$)$_2$:PCBM	Ti:Sapphire	15.9	0.82	67.3	8.8	21
2024	**PM6:Y6**	**CO_2**	**27.4**	**0.85**	**72.3**	**16.8**	**This work**

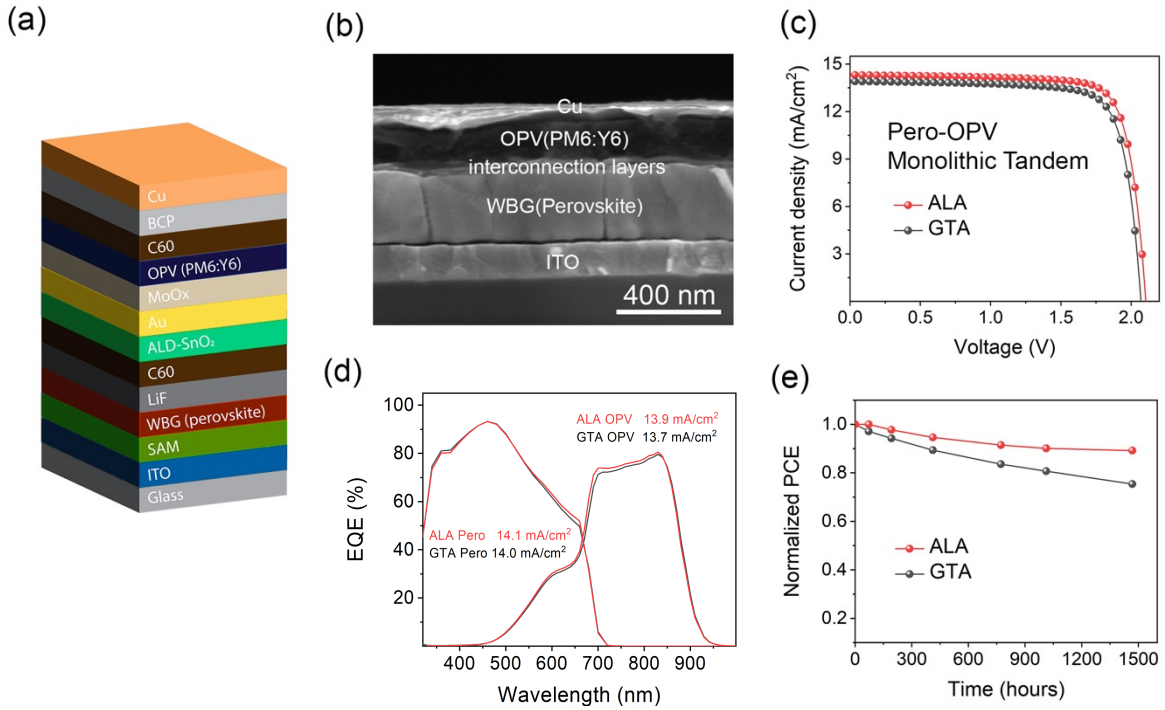

Figure 5.20 Perovskite-OPV tandem (a) structure schematic, (b) cross-sectional SEM image, (c) champion *J-V* and (d) representative EQE and (e) thermal stability (60 °C in N_2 filled glove box) of representative ALA and GTA devices.

Table 5.7 Summary of champion GTA and ALA perovskite-OPV tandem performances.

Annealing	J_{SC} (mA cm^{-2})	V_{OC} (V)	FF (%)	PCE (%)
GTA	13.9	2.07	78.6	22.6
ALA	14.3	2.10	79.6	24.0

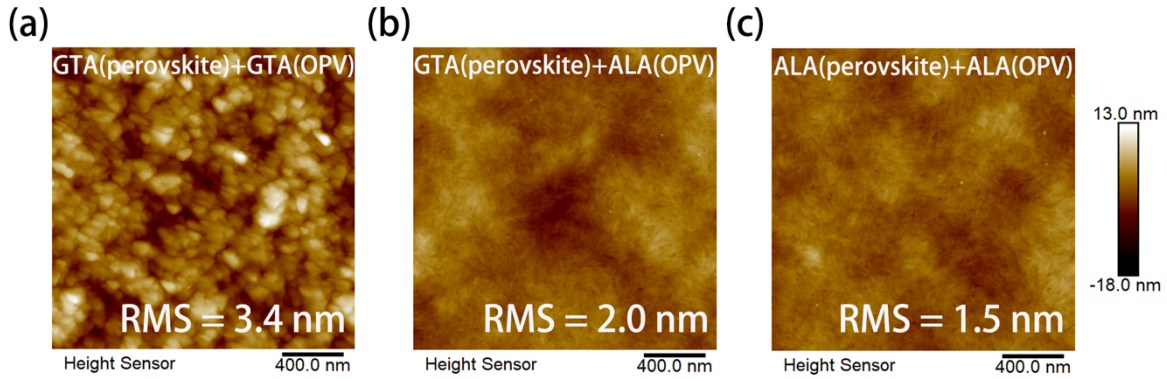

Figure 5.21 AFM images for PM6:Y6 OPV/MoO_x/Au/ALD-SnO_2/C60/LiF/perovskite/HTL/ITO/glass processed by (a) GTA(perovskite)+GTA(OPV); (b) GTA(perovskite)+ALA(OPV); (c) ALA(perovskite)+ALA(OPV).

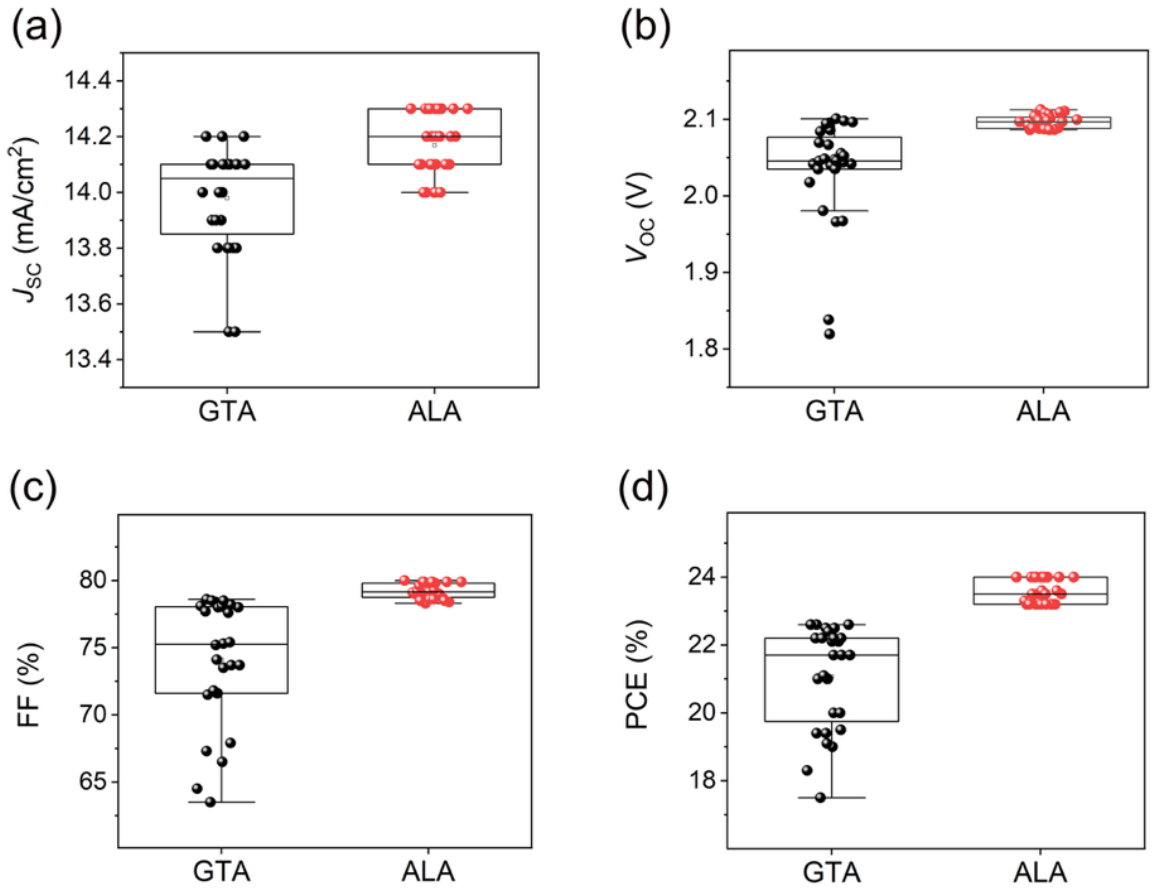

Figure 5.22 Distributions of (a) J_{SC}, (b) V_{OC}, (c) FF, and (d) PCE of GTA- and ALA-perovskite-OPV tandems:

Finally, perovskite-organic tandem solar cells (**Figures 5.20a&b**) was demonstrated whereby all annealing was performed by laser for the fabrication of mixed MeO-2PACz:Me-4PACz self-assembled-monolayer type hole layer, the perovskite layer, as well as the PM6:Y6 OPV layer. The all-laser-annealed tandems are smoother (**Figure 5.21**), and performed better across all electrical characteristics (**Table 5.7**), with narrower distributions (**Figure 5.22**), demonstrating better reproductivity, compared to the hot-plate annealed tandem even though the former was annealed in the ambient while the latter was inside a N_2 filled glovebox.

The laser annealed tandem was also more thermal stable (**Figure 5.20e**). Future work will involve further optimisation of the laser annealed OPV cell to reduce current mismatch in the tandem (**Figure 5.20d**) although similar or even higher current mismatch have been observed in 19 reported perovskite-OPV tandems, out of the 50 listed in (**Table 5.1**).

5.4 Conclusion

In this chapter, the first laser annealed perovskite-OPV tandem solar cell and the first laser annealed OPV cell based on PM6:Y6 were reported, capitalising on the advantage of laser annealing in suppressing phase segregation in wide-bandgap perovskites and in producing smoother PM6:Y6 OPV film for improved PM6:Y6/C_{60} interface. For phase segregation suppression in wide bandgap perovskites, it was found that rapid heating and cooling rates, rather than annealing temperature were the decisive factor. For laser annealing PM6:Y6 OPV, using optimal laser power density was critical for PM6:Y6 film morphology. As a result, a champion power conversion efficiency that was the highest for laser annealed OPV cell was achieved at the time of reporting. The first laser annealed perovskite-OPV tandem produced a champion efficiency of 24% which is impressive given the annealing for all layers (mixed MeO-2PACz:Me-4PACz self-assembled-monolayer type hole layer, the wide bandgap 1.78 eV perovskite layer, and the PM6:Y6 OPV layer) were conducted in ambient. This work demonstrates the tremendous potentials of laser annealing for perovskite tandem solar cells especially in mass production given the time savings gained by the laser process.

5.5 References

(1) You, P.; Li, G.; Tang, G.; Cao, J.; Yan, F. Ultrafast laser-annealing of perovskite films for efficient perovskite solar cells. *Energy & Environmental Science* **2020**, *13* (4), 1187-1196. DOI: https://doi.org/10.1039/C9EE02324K.

(2) Jeon, T.; Jin, H. M.; Lee, S. H.; Lee, J. M.; Park, H. I.; Kim, M. K.; Lee, K. J.; Shin, B.; Kim, S. O. Laser crystallization of organic–inorganic hybrid perovskite solar cells. *ACS nano* **2016**, *10* (8), 7907-7914. DOI: https://doi.org/10.1021/acsnano.6b03815.

(3) Li, F.; Zhu, W.; Bao, C.; Yu, T.; Wang, Y.; Zhou, X.; Zou, Z. Laser-assisted crystallization of $CH_3NH_3PbI_3$ films for efficient perovskite solar cells with a high open-circuit voltage. *Chemical Communications* **2016**, 52 (31), 5394-5397. DOI: https://doi.org/10.1039/c6cc00753H.

(4) Shan, X.; Wang, S.; Dong, W.; Pan, N.; Shao, J.; Wang, X.; Tao, R.; Deng, Z.; Hu, L.; Kong, F. Flash surface treatment of $CH_3NH_3PbI_3$ films using 248 nm KrF excimer laser enhances the

performance of perovskite solar cells. *Solar RRL* **2019**, *3* (7), 1900020. DOI: https://doi.org/10.1002/solr.201900020.

(5) Kong, W.; Zhao, C.; Xing, J.; Zou, Y.; Huang, T.; Li, F.; Yang, J.; Yu, W.; Guo, C. Enhancing perovskite solar cell performance through femtosecond laser polishing. *Solar RRL* **2020**, *4* (7), 2000189. DOI: https://doi.org/10.1002/solr.202000189.

(6) Trinh, X.-L.; Tran, N.-H.; Seo, H.; Kim, H.-C. Enhanced performance of perovskite solar cells via laser-induced heat treatment on perovskite film. *Solar Energy* **2020**, *206*, 301-307. DOI: https://doi.org/10.1016/j.solener.2020.05.063.

(7) Kedia, M.; Rai, M.; Phirke, H.; Aranda, C. A.; Das, C.; Chirvony, V.; Boehringer, S.; Kot, M.; Byranvand, M. M.; Flege, J. I. Light makes right: laser polishing for surface modification of perovskite solar cells. *ACS Energy Letters* **2023**, *8* (6), 2603-2610. DOI : https://doi.org/10.1021/acsenergylett.3c00469.

(8) Yi, J.; Leung, T.-L.; Digweed, J.; Bing, J.; Bailey, C.; Liao, C.; Tao, R.; Wang, G.; Li, Z.; Nguyen, H. T.; et al. CO_2 Laser Crystallization in Ambient for Highly Efficient $FAPbI_3$ Perovskite Solar Cells. *Small* **2024**, *20* (45), 2402215. DOI: https://doi.org/10.1002/smll.202402215.

(9) Chae, S.; Jo, K. H.; Lee, S. W.; Keum, H. S.; Kim, H. J.; Choi, J.; Lee, H. H. Selective chain alignment of conducting polymer blend films by an ultrafast laser. *Macromolecular Chemistry and Physics* **2016**, *217* (4), 537-542. DOI: https://doi.org/10.1002/macp.201500354.

(10) Gill, H. S.; Thota, S.; Li, L.; Kokil, A.; Mosurkal, R.; Kumar, J. Performance enhancement of fullerene based solar cells upon NIR laser irradiation. *RSC Advances* **2015**, *5* (60), 48526-48532. DOI: 10.1039/C5RA05640C.

(11) Lan, S.; Wu, X.; Zhang, G.; Chen, G.; Chen, H.; Guo, T. Improvement of Device Performance of Organic Photovoltaics via Laser Irradiation. *The Journal of Physical Chemistry C* **2019**, *123* (36), 22058-22065. DOI: 10.1021/acs.jpcc.9b06707.

(12) Guo, X.; Jia, Z.; Liu, S.; Guo, R.; Jiang, F.; Shi, Y.; Dong, Z.; Luo, R.; Wang, Y.D.; Shi, Z. and Li, J.; Stabilizing efficient wide-bandgap perovskite in perovskite-organic tandem solar cells. *Joule* **2024**, *8* (9), 2554-2569. DOI: 10.1016/j.joule.2024.06.009.

(13) Li, Y.; Yan, Y.; Fu, Y.; Jiang, W.; Liu, M.; Chen, M.; Huang, X.; Lu, G.; Lu, X.; Yin, J.; Wu, S.; Highly durable inverted inorganic perovskite/organic tandem solar cells enabled by multifunctional additives. *Angewandte Chemie International Edition* ***2024***, *63* (52), e202412515. DOI: https://doi.org/10.1002/anie.202412515.

(14) Zhang, Z.; Chen, W.; Jiang, X.; Cao, J.; Yang, H.; Chen, H.; Yang, F.; Shen, Y.; Yang, H.; Cheng, Q. and Chen, X.; Suppression of phase segregation in wide-bandgap perovskites with thiocyanate ions for perovskite/organic tandems with 25.06% efficiency. *Nature Energy* **2024**, *9* (5), 592-601. DOI: https://doi.org/10.1038/s41560-024-01491-0.

(15) Bai, Y.; Tian, S.; Guan, Y.; Wang, X.; Wang, F.; Li, M.; Tan, Z.A. and Liu, G.; Bidirectional Voltage Regulation for Integrated Photovoltachromic Device Based on P3HT-Electrochromic Unit and Perovskite/Organic Tandem Solar Cells. *Small* **2024**, *20* (42), 2402903. DOI: https://doi.org/10.1002/smll.202402903.

(16) Chen, C, C.; Bae, S., H.; Chang, W. H.; Hong, Z.; Li, G.; Chen, Q.; Zhou, H.; Yang, Y.; Perovskite/polymer monolithic hybrid tandem solar cells utilizing a low-temperature, full solution process. *Materials Horizons* **2015**, *2* (2), 203-11. DOI: 10.1039/C4MH00237G.

(17) Liu, Y.; Renna, L. A.; Bag, M.; Page, Z. A.; Kim, P.; Choi, J.; Emrick, T.; Venkataraman, D.; Russell, T. P.; High efficiency tandem thin-perovskite/polymer solar cells with a graded recombination layer. *ACS applied materials & interfaces* **2016**, *8* (11), 7070-6. DOI: https://doi.org/10.1021/acsami.5b12740.

(18) Chen, X.; Jia, Z.; Chen, Z.; Jiang, T.; Bai, L.; Tao, F.; Chen, J.; Chen, X.; Liu, T.; Xu, X.; Yang, C.; Efficient and reproducible monolithic perovskite/organic tandem solar cells with low-loss interconnecting layers. *Joule* **2020**, *4* (7), 1594-606. DOI: 10.1016/j.joule.2020.06.006.

(19) Xie, S.; Xia, R.; Chen, Z.; Tian, J.; Yan, L.; Ren, M.; Li, Z.; Zhang, G.; Xue, Q.; Yip, H. L.; Cao, Y.; Efficient monolithic perovskite/organic tandem solar cells and their efficiency potential. *Nano Energy* **2020**, *78*, 105238. DOI: https://doi.org/10.1016/j.nanoen.2020.105238.

(20) Li, Z.; Wu, S.; Zhang, J.; Lee, K. C.; Lei, H.; Lin, F.; Wang, Z.; Zhu, Z.; Jen, A. K.; Hybrid perovskite-organic flexible tandem solar cell enabling highly efficient electrocatalysis overall

water splitting. *Advanced Energy Materials* **2020**, *10* (18), 2000361. DOI: https://doi.org/10.1002/aenm.202000361.

(21) Wang, P.; Li, W.; Sandberg, O. J.; Guo, C.; Sun, R.; Wang, H.; Li, D.; Zhang, H.; Cheng, S.; Liu, D.; Min, J.; Tuning of the interconnecting layer for monolithic perovskite/organic tandem solar cells with record efficiency exceeding 21%. *Nano Letters* **2021**, *21* (18), 7845-54. DOI: https://doi.org/10.1021/acs.nanolett.1c02897.

(22) Chen, W.; Zhu, Y.; Xiu, J.; Chen, G.; Liang, H.; Liu, S.; Xue, H.; Birgersson, E.; Ho, J. W.; Qin, X.; Lin, J.; Monolithic perovskite/organic tandem solar cells with 23.6% efficiency enabled by reduced voltage losses and optimized interconnecting layer. *Nature Energy* **2022**, *7* (3), 229-37. DOI: https://doi.org/10.1038/s41560-021-00966-8.

(23) Zhang, Z.; Cueto, C.; Ding, Y.; Yu, L.; Russell, T. P.; Emrick, T.; Liu, Y.; High-Performance 1 cm^2 Perovskite-Organic Tandem Solar Cells with a Solvent-Resistant and Thickness-Insensitive Interconnecting Layer. *ACS applied materials & interfaces* **2022**, *14* (26), 29896-904. DOI: https://doi.org/10.1021/acsami.2c06760.

(24) Ding, Y.; Guo, Q.; Geng, Y.; Dai, Z.; Wang, Z.; Chen, Z.; Guo, Q.; Zheng, Z.; Li, Y.; Zhou, E.; A low-cost hole transport layer enables $CsPbI_2Br$ single-junction and tandem perovskite solar cells with record efficiencies of 17.8% and 21.4%. *Nano Today* **2022**, *46*, 101586. DOI: https://doi.org/10.1016/j.nantod.2022.101586.

(25) Tian, S.; Huang, T.; Han, F.; Wang, F.; Tan, Z. A.; Bai, Y.; Optimization of tail state Urbach energy enables efficient organic solar cells and perovskite/organic tandem solar cells. *Organic Electronics* **2023**, *113*, 106714. DOI: https://doi.org/10.1016/j.orgel.2022.106714.

(26) Yang, H.; Chen, W.; Yu, Y.; Shen, Y.; Yang, H.; Li, X.; Zhang, B.; Chen, H.; Cheng, Q.; Zhang, Z.; Qin, W.; Regulating charge carrier recombination in the interconnecting layer to boost the efficiency and stability of monolithic perovskite/organic tandem solar cells. *Advanced Materials* **2023**, *35* (6), 2208604. DOI: https://doi.org/10.1002/adma.202208604.

(27) Wu, H.; Chen, T.; Li, Y.; Guan, S.; Zhang, L.; Chen, T.; Liu, Y.; Jin, Y.; Zuo, L.; Fu, W.; Wu, G.; Phase-segregation free quasi-2D perovskite/organic tandem solar cells with low *V*oc loss and efficiency beyond 21%. *Journal of Materials Chemistry A* **2023**, *11* (13), 6877-85. DOI: https://doi.org/10.1039/D3TA00052D.

(28) Ding, Y.; Duan, C.; Guo, Q.; Meng, Y.; Wang, Z.; Dai, Z.; Zhou, E.; Side-chain engineering of benzotriazole-based polymers as hole transport material enables high-efficiency $CsPbI_2Br$ single-junction and tandem perovskite solar cells. *Nano Today* **2023**, *53*, 102046. DOI: https://doi.org/10.1016/j.nantod.2023.102046.

(29) Tang, Y.; Zhang, Y.; Zhou, X.; Huang, T.; Shen, K.; Zhang, K.; Du, X.; Shi, T.; Xiao, X.; Li, N. and Brabec, C.J.; Solvent engineering of scalable deposited wide-bandgap perovskites for efficient monolithic perovskite-organic tandem solar cells. *Nano Energy* **2023**, *114*, 108653. DOI: https://doi.org/10.1016/j.nanoen.2023.108653.

(30) Sun, S. Q.; Xu, X.; Sun, Q.; Yao, Q.; Cai, Y.; Li, X. Y.; Xu, Y. L.; He, W.; Zhu, M.; Lv, X.; Lin, F. R.; All-inorganic perovskite-based monolithic perovskite/organic tandem solar cells with 23.21% efficiency by dual-interface engineering. *Advanced Energy Materials* **2023**, *13* (16), 2204347. DOI: https://doi.org/10.1002/aenm.202204347.

(31) Ye, Q.; Fan, B.; Zhou, Y.; Liu, S.; Yao, S.; Lv, J.; Wang, C.; Dai, R.; Chen, D.; Meng, X. and Huang, Z.; Competitive Crystallization Modulated Phase-Homogeneous Wide-Bandgap Perovskites for Monolithic Perovskite-Organic Tandem Solar Cells. Advanced Materials **2025**, 11781. DOI: https://doi.org/10.1002/adma.202511781.

(32) Yao, Q.; Xie, Y. M.; Zhou, Y.; Xue, Q.; Xu, X.; Gao, Y.; Niu, T.; Chu, L.; Zhou, Z.; Lin, F. R. and Jen, A.K.Y.; Dual sub-cells modification enables high-efficiency n–i–p type monolithic perovskite/organic tandem solar cells. *Advanced Functional Materials* **2023**, *33* (8), 2212599. DOI: https://doi.org/10.1002/adfm.202212599.

(33) Xu, H.; Torres M. L.; Koc, M.; Aydin, E.; Zhumagali, S.; Haque, M. A.; Yazmaciyan, A.; Sharma, A.; Rosas, V. D.; Huerta, H.; De, B. M.; Metal-free interconnecting layer for monolithic perovskite/organic tandem solar cells with enhanced outdoor stability. *ACS Applied Energy Materials* **2022**, *5* (11), 14035-44. DOI: https://doi.org/10.1021/acsaem.2c01749.

(34) Wang, C.; Shao, W.; Liang, J.; Chen, C.; Hu, X.; Cui, H.; Liu, C.; Fang, G.; Tao, C.; Suppressing phase segregation in wide bandgap perovskites for monolithic perovskite/organic tandem solar cells with reduced voltage loss. *Small* **2022**, *18* (49), 2204081. DOI: https://doi.org/10.1002/smll.202204081.

(35) Qin, S.; Lu, C.; Jia, Z.; Wang, Y.; Li, S.; Lai, W.; Shi, P.; Wang, R.; Zhu, C.; Du, J.; Zhang, J.; Constructing monolithic perovskite/organic tandem solar cell with efficiency of 22.0% via reduced open-circuit voltage loss and broadened absorption spectra. *Advanced Materials* **2022**, *34* (11), 2108829. DOI: https://doi.org/10.1002/adma.202108829.

(36) Brinkmann, K. O.; Becker, T.; Zimmermann, F.; Kreusel, C.; Gahlmann, T.; Theisen, M.; Haeger, T.; Olthof, S.; Tückmantel, C.; Günster, M.; Maschwitz, T.; Perovskite–organic tandem solar cells with indium oxide interconnect. *Nature* **2022**, *604* (7905), 280-6. DOI: https://doi.org/10.1038/s41586-022-04455-0.

(37) Hu, X.; Zhao, C.; Liu, Y.; Li, J. A.; Wang, L.; Tang, X.; Dou, Y.; Shi, X.; Liu, T.; Luo, S. and Chen, S.; Blade-Coated Perovskite-Organic Tandem Solar Cells in Ambient Conditions. *Advanced Functional Materials* **2025**, 12093. DOI: https://doi.org/10.1002/adfm.202512093.

(38) Xie, G.; Li, H.; Wang, X.; Fang, J.; Lin, D.; Wang, D.; Li, S.; He, S.; Qiu, L.; Phase segregation and voltage loss mitigated highly efficient perovskite–organic tandem solar cells with a simple ambipolar SnOx interconnecting layer. *Advanced Functional Materials* **2023**, *33* (52), 2308794. DOI: https://doi.org/10.1002/adfm.202308794.

(39) Wang, X.; Zhang, D.; Liu, B.; Wu, X.; Jiang, X.; Zhang, S.; Wang, Y.; Gao, D.; Wang, L.; Wang, H. and Huang, Z.; Highly efficient perovskite/organic tandem solar cells enabled by mixed‐cation surface modulation. *Advanced Materials* **2023**, *35* (49), 2305946. DOI: https://doi.org/10.1002/adma.202305946.

(40) Mahmud, M. A.; Zheng, J.; Chang, J. F.; Wang, G.; Liao, C.; Rahman, M. H.; Tarique, W. B.; Tang, S.; Bing, J.; Bailey, C. G.; Li, Z.; Halogenated Polycyclic Aromatic Hydrocarbon for Hole Selective Layer/Perovskite Interface Modification and Passivation for Efficient Perovskite‐Organic Tandem Solar Cells with Record Fill Factor. *Advanced Energy Materials* **2024**,*14* (45), 2400691. DOI: https://doi.org/10.1002/aenm.202400691.

(41) Wu, S.; Yan, Y.; Yin, J.; Jiang, K.; Li, F.; Zeng, Z.; Tsang, S. W.; Jen A. K.; Redox mediator-stabilized wide-bandgap perovskites for monolithic perovskite-organic tandem solar cells. *Nature Energy* **2024**, *9* (4), 411-21. DOI: https://doi.org/10.1038/s41560-024-01451-8.

(42) Bai, Y.; Tian, S.; Guan, Y.; Wang, X.; Wang, F.; Li, M.; Tan, Z.A. and Liu, G.; Bidirectional Voltage Regulation for Integrated Photovoltachromic Device Based on P3HT‐

Electrochromic Unit and Perovskite/Organic Tandem Solar Cells. *Small* **2024**, *20* (42), 2402903. DOI: https://doi.org/10.1002/smll.202402903.

(43) An, Y.; Zhang, N.; Liu, Q.; Jiang, W.; Du, G.; Chen, D.; Liu, M.; Huang, X.; Lei, T.; Qiu, Q. and Lin, F.R.; Balancing carrier transport in interconnection layer for efficient perovskite/organic tandem solar cells. *Nature communications* **2025**, *16* (1), 1-11. DOI: https://doi.org/10.1038/s41467-025-58047-3.

(44) Han, Y.; Fu, J.; Ren, Z.; Yu, J.; Liang, Q.; Xu, Z.; Xie, X.; Li, D.; Ma, R.; Cao, M. and Sun, Y.; Inorganic perovskite/organic tandem solar cells with 25.1% certified efficiency via bottom contact modulation. *Nature Energy* **2025**, 1-13. DOI: https://doi.org/10.1038/s41560-025-01742-8.

(45) Tian, J.; Liu, C.; Forberich, K.; Barabash, A.; Xie, Z.; Qiu, S.; Byun, J.; Peng, Z.; Zhang, K.; Du, T. and Sathasivam, S.; Overcoming optical losses in thin metal-based recombination layers for efficient nip perovskite-organic tandem solar cells. *Nature Communications* **2025**, *16* (1), 154. DOI: https://doi.org/10.1038/s41467-024-55376-7.

(46) Cui, X.; Xie, G.; Ran, G.; Liu, Y.; Ma, X.; Zhang, G.; Kong, Q.; Zhang, W.; Li, H.; Cheng, P. and Ouyang, D.; Organic film evolution and recombination losses in highly efficient perovskite/organic tandem solar cells. *Nature Communications* **2025**, *16* (1), 8986. DOI: https://doi.org/10.1038/s41467-025-64032-7.

(47) He, Z.; Yu, R.; Dong, Y.; Wang, R.; Zhang, Y. and Tan, Z.A.; Minimized optical/electrical energy loss for 25.1% Monolithic perovskite/organic tandem solar cells. *Nature Communications* **2025**, *16* (1), 1773. DOI: https://doi.org/10.1038/s41467-025-57093-1.

(48) Xiao, Y.; Huang, T.; Chen, N.; Chen, P.; Luo, D.; Jiang, X.; Jia, X.; Hu, J.; Wang, D.; Kaienburg, P. and Mahesh, S.; Improved Interconnecting Layer for Perovskite–Organic Tandem Solar Cells. *ACS Energy Letters* **2025**, *10*, 5184-5191. DOI: https://doi.org/10.1021/acsenergylett.5c01923.

(49) Chen, X.; Jia, Z.; Chen, Z.; Zhou, C.; Huang, S.; Xia, X.; Liang, S.; Wang, P.; Jiang, T.; Liu, T. and Xu, X.; Efficient Perovskite/Organic Tandem Photovoltaic Devices and Large‐area

Modules Featuring Thick-Film Organic Solar Cells. *Advanced Materials* **2025**, 2500190. DOI: https://doi.org/10.1002/adma.202500190.

(50) Son, J.G.; Ameen, S.; Roe, J.; Park, S.; Seo, J.; Kim, J.; Faheem, A.B.; Koo, H.E.; Oh, S.O.; Jo, Y. and Kim, J.W.; Exceeding 2.2 V Open-Circuit Voltage in Perovskite/Organic Tandem Solar Cells via Multi-Functional Hole-Selective Layer. *Advanced Energy Materials* **2025**, *15* (28), 2404092. DOI: https://doi.org/10.1002/aenm.202404092

(51) Zheng, J.; Chen, W.; Wang, Z.; Kang, S.; Dong, P.; Yin, Y.; Chen, H.; Cao, J.; Yuan, J.; Xu, G. and Xu, J.; Selective Crystallization Delay in Wide-Bandgap Perovskites Enables Initial Homogeneous Phase for Square Centimeter Perovskite/Organic Tandem Solar Cells. *Advanced Materials* **2025**, e10437. DOI: https://doi.org/10.1002/adma.202510437.

(52) Wang, Y.D.; Jia, Z.; Liu, S.; Luo, R.; Zhang, Y.; Steele, J.A.; Degnan, Z.; Bilal Faheem, M.; Solano, E.; Qiao, Q. and Li, J.; Regulating wide-bandgap perovskite face-on stacking in hybrid-deposited perovskite/organic tandem solar cells. *Nature Communications* **2025**, *16* (1), 6142. DOI: https://doi.org/10.1038/s41467-025-61404-x.

(53) Li, X.Y.; Wu, Z.; Yao, Q.; Chen, L.Y.; Zeng, W.; Sun, Q.; Lin, F.R.; Jen, A.K.Y.; Shi, T.; Yip, H.L. and Xie, Y.M.; Buried Interface Modification Toward Efficient $CsPbI_{2.2}Br_{0.8}$ Based Monolithic Perovskite/Organic Tandem Solar Cells. *Small* **2025**, *21* (3), 2406824. DOI: https://doi.org/10.1002/smll.202406824.

(54) Jiang, S.; Wang, Z.; Xu, C.; Yang, J.; Wang, Y.; Gong, K.; Li, K.; Liu, T. and Tan, Z.A.; Synergistic Optimization of n‐i‐p Structured Monolithic All‐Inorganic Perovskite/Organic Tandem Solar Cells Achieving Efficiency over 24%. *Small* **2025**, 2500134. DOI: https://doi.org/10.1002/smll.202500134.

(55) Xie, G.; Li, H.; Fang, J.; Wang, X.; Peng, H.; Lin, D.; Huang, N.; Gan, L.; Li, W.; Jiang, R. and Bu, T.; Crystallization Thermodynamics Regulation of 1.85 eV Wide‐Bandgap Perovskite for Efficient and Stable Perovskite‐Organic Tandem Photovoltaics. *Angewandte Chemie International Edition* **2025**, *64* (17), e202501764. DOI: https://doi.org/10.1002/anie.202501764.

(56) Aslam, F.; Li, H.; Chang, J.; Tahir, M.; Zahid, M.; Sadiq, M.I.; Liao, X.; Zeng, Q.; Liu, F. and Yang, J.; Dual-Interface Passivation of Wide-Bandgap Perovskite Films for Efficient Four-Terminal Perovskite–Organic Tandem Solar Cells. *The Journal of Physical Chemistry Letters* **2025**, *16* (21), 5195-5201. DOI: https://doi.org/10.1021/acs.jpclett.5c00756.

(57) Wang, Y.; Liu, B.; Zhang, D.; Yu, H.; Wu, X.; Gao, D.; Li, B.; Zhang, C.; Liu, W.; Yu, Z. and Wang, N.; All‐Polymer Bulk‐Heterojunction Enables Stable Monolithic Perovskite/Organic Tandem Solar Cells with High Efficiency. *Small* **2025**, *21* (13), 2411031. DOI: https://doi.org/10.1038/s41560-021-00966-8.

(58) Liu, S.; Hao, L.; Yu, J.; Xu, Y.; Dou, Y.; Xie, J.; Wang, Y.; Zhang, K.; Huang, F. and Cao, Y.; High-Performance and Stable Perovskite/Organic Tandem Solar Cells Enabled by Interconnecting Layer Engineering. *ACS nano* **2024**, *19* (1), pp.748-759. DOI: https://doi.org/10.1021/acsnano.4c11888.

(59) Jiang, X.; Qin, S.; Meng, L.; He, G.; Zhang, J.; Wang, Y.; Zhu, Y.; Zou, T.; Gong, Y.; Chen, Z. and Sun, G.; Isomeric diammonium passivation for perovskite–organic tandem solar cells. *Nature* **2024**, *635* (8040), 860-866. DOI: https://doi.org/10.1038/s41586-024-08160-y.

(60) Wu, X.; Zhang, D.; Liu, B.; Wang, Y.; Wang, X.; Liu, Q.; Gao, D.; Wang, N.; Li, B.; Wang, L. and Yu, Z.; Optimization of charge extraction and interconnecting layers for highly efficient perovskite/organic tandem solar cells with high fill factor. *Advanced Materials* **2024**, *36* (49), 2410692. DOI: https://doi.org/10.1002/adma.202410692.

(61) Lang, K.; Xu, J.; Han, H.; Liu, H.; Fu, Y.; Zhang, X.; Sun, Z.; Shi, Q.; Tan, Z.A. and Yao, J.; Optimized Crystallization of $CsPbI_2Br$ Films through the Incorporation of H_2O for High‐Efficiency All‐Inorganic Perovskite/Organic Tandem Solar Cell. *Advanced Functional Materials* **2025**, 2502966. DOI: https://doi.org/10.1002/adfm.202502966.

(62) Shi, L.; Bucknall, M. P; Young, T.; Zhang, M.; Hu, R.; Bing, J.; Lee, D. S.; Kim, J.; Wu, T.; Takamure, N.; Mckenzie, D. R.; Huang, S. J.; Green, M.A.; Ho-Baillie, A. W. Y.; Gas chromatography-mass spectrometry analyses of encapsulated stable perovskite solar cells. *Science* **2020**, *368* (6497), eaba2414. DOI: 10.1126/science.aba2412.

(63) Shi, L.; Young, T. L.; Kim, J.; Sheng, Y.; Wang, L.; Chen, Y.; Feng, Z.; Keevers, M.J.; Hao, X.; Verlinden, P.J.; Green, M.A.; Ho-Baillie, A. W. Y.; Accelerated lifetime testing of

organic–inorganic perovskite solar cells encapsulated by polyisobutylene. *ACS applied materials & interfaces* **2017**, *9* (30), 25073-25081. DOI: 10.1021/acsami.7b07625.

(64) Song, C.; Lou, S.; Deng, S.; Li, M.; Xin, J.; Liang, Q.; Liu, J.; Mitigating Ion Migration in a Mixed-Halide Perovskite via Laser Shock Annealing. *The Journal of Physical Chemistry Letters.* **2025**, *9* (16),10345-54. DOI: https://doi.org/10.1021/acs.jpclett.5c02594.

(65) Cao Z., Wei C., Cheng X., Zhao Y., Peng X., Jiang Z., and Shao J., Ground fused silica processed by combined chemical etching and CO_2 laser polishing with super-smooth surface and high damage resistance. *Optics Letter* **2020**, *45*, 6014-6017. DOI: https://doi.org/10.1364/OL.409857.

(66) Mendez E., Baker H., Nowak K., Villarreal F., Hall D., Mendez E., Baker H., Nowak K., Villarreal F., Hall D., Highly localized CO_2 laser cleaning and damage repair of silica optical surfaces. Proc. SPIE 5647, *Laser-Induced Damage in Optical Materials* **2004**, 5647. DOI: https://doi.org/10.1117/12.585293.

(67) He, T.; Wei, C.; Jiang, Z.; Zhao, Y. and Shao, J.; Super-smooth surface demonstration and the physical mechanism of CO_2 laser polishing of fused silica. *Optics Letter* **2018**, *43*, 5777-5780. DOI: https://doi.org/10.1364/OL.43.005777.

(68) Ning, H.; Jiang, Q.; Han, P.; Lin, M.; Zhang, G.; Chen, J.; Chen, H.; Zeng, S.; Gao, J.; Liu, J.; et al. Manipulating the solubility properties of polymer donors for high-performance layer-by-layer processed organic solar cells. *Energy & Environmental Science* **2021**, *14* (11), 5919-5928. DOI: 10.1039/D1EE01336J.

(69) Qian, D.; Pratik, S. M.; Liu, Q.; Dong, Y.; Zhang, R.; Yu, J.; Gasparini, N.; Wu, J.; Zhang, T.; Coropceanu, V.; et al. Correlating the Hybridization of Local-Exciton and Charge-Transfer States with Charge Generation in Organic Solar Cells. *Advanced Energy Materials* **2023**, *13* (32), 2301026. DOI: 10.1002/aenm.202301026.

(70) Okraku, E. W.; Gupta, M. C.; Wright, K. D. Pulsed laser annealing of P3HT/PCBM organic solar cells. *Solar Energy Materials and Solar Cells* **2010**, *94* (12), 2013-2017. DOI: https://doi.org/10.1016/j.solmat.2010.06.004.

(71) Cui, J.; Rodríguez-Rodríguez, Á.; Hernández, M.; García-Gutiérrez, M.-C.; Nogales, A.; Castillejo, M.; Moseguí González, D.; Müller-Buschbaum, P.; Ezquerra, T. A.; Rebollar, E.

Laser-Induced Periodic Surface Structures on P3HT and on Its Photovoltaic Blend with $PC_{71}BM$. *ACS Applied Materials & Interfaces* **2016**, *8* (46), 31894-31901. DOI: 10.1021/acsami.6b09053.

(72) Feng, L.; Zheng, F.; Bi, P.-Q.; Yang, X.-Y.; Niu, M.-S.; Wang, F.; Hao, X.-T. Laser-induced crystallization and conformation control of poly(3-hexylthiophene) for improving the performance of organic solar cells. *Organic Electronics* **2017**, *49*, 157-164. DOI: https://doi.org/10.1016/j.orgel.2017.06.053.

Chapter 6 Conclusion and future outlook

6.1 Summary including originality, novelty and significance

The originality and novelty of this thesis lie in the first demonstration of the feasibility and effectiveness of CO_2 laser annealing for the fabrication of efficient single- and multi-junction perovskite solar cells.

New knowledge generated in Chapter 2 is the strong dependence of laser power on the formation of α-$FAPbI_3$ phase and its crystallinity. Using laser power higher than the optimum drives out the volatile organic component in the perovskite film increasing the presence of PbI_2 defects.

Chapter 3 presented the first three-dimensional (3D) simulated macroscopic and localized temperature profiles during laser annealing of perovskite and hole transport layers using COMSOL Multiphysics. New insights include the visualisation of the shape and depth of the laser heated region in time and space.

The confinement of laser generated heat within the perovskite layer or the hole transport layer meant that laser annealing can be applied to more than one layer in the fabrication of perovskite solar cells as demonstrate in Chapter 4. A key novelty of this chapter is the development of ambient laser annealing for fabricating self-assembly-monolayer type hole transport layer (HTL). What was not obvious before is the fact that laser-annealing resulted in a higher quality HTL surface for the subsequent perovskite deposition. Laser-annealing of the perovskite layer then further improved its quality. The very first all-laser-annealed wide-bandgap perovskite solar cell produced a champion open-circuit voltage (V_{OC}) of 1.35 V and a champion power conversion efficiency (PCE) that were the highest for a 1.80 eV perovskite single-junction solar cell at the time of reporting.

Chapter 5 uncovered the new knowledge rapid heating and cooling rates, rather than annealing temperature were the decisive factor for suppressing phase segregation in wide bandgap perovskites. Another discovery was that optimal laser power density was critical for PM6:Y6 film morphology and smooth PM6:Y6 film resulting in high quality PM6:Y6 /C_{60} interface was the key to performance improvement in laser annealed PM6:Y6 organic photovoltaic (OPV) cells producing a champion efficiency that was highest for laser-annealed OPVs at the time of reporting.

These findings successfully established laser annealing as a viable alternative to conventional thermal annealing, offering significant time savings compared to hot-plate annealing. Additionally, laser annealing maintains a lower substrate temperature making it a promising technique for temperature-sensitive substrates. The temperature modelled developed will be useful for future process developments for more complicated cell structures.

6.2 Future work

To better understand the underlying mechanism for perovskite crystallization, e.g., α -$FAPbI_3$ formation as a function of laser power, future experiments can be conducted to decouple thermal and photochemical effects from CO_2 laser such as laser "annealing" of perovskite films on cooled substrates.

Future research can also involve the investigation of larger beam profiles for larger device dimensions, while maintaining process uniformity. Such study would be crucial for bridging the gap between laboratory-scale demonstrations and industrial-scale production.

Additionally, simulation model will be extended for the purpose of optimizing laser parameters—such as pulse duration, energy density, and scanning strategies, to engineer material properties. The aim is to further enhance laser-annealed-film quality, device efficiency and reproducibility.

An important future direction is to explore how laser annealing can enhance the operational stability of perovskite devices, with particular focus on the fundamental interactions between the laser and the perovskite layer, as well as the role of laser-induced effects on additives.

Laser annealing can also be further explored for perovskite-perovskite, perovskite-silicon and perovskite-CIGS tandems, noting different material systems may involve different laser-matter interaction.

Moreover, it will be advantageous to investigate the use of laser process for flexible and lightweight photovoltaic applications that typically employ temperature-sensitive-substrates. Such process may increase the viability of niche wearable and portable solar applications.

Another exciting opportunity is the integration of laser annealing (e.g., via multiple laser heads or line beam) with roll-to-roll printing, for scaling of the manufacturing of perovskite solar cells.